Effects of Planetary Parameters on Disequilibrium Chemistry in Irradiated Planetary Atmospheres: From Gas Giants to Sub-Neptunes

Sagnick Mukherjee (iD),[1,2] Jonathan J. Fortney(iD),[1] Nicholas F. Wogan,[3] David K. Sing,[4,2] and Kazumasa Ohno (iD)[5]

[1]*Department of Astronomy and Astrophysics, University of California, Santa Cruz, CA 95064, USA*
[2]*Department of Physics and Astronomy, Johns Hopkins University, Baltimore, MD, USA*
[3]*Space Science Division, NASA Ames Research Center, Moffett Field, CA 94035, USA*
[4]*Department of Earth and Planetary Sciences, Johns Hopkins University, Baltimore, MD, USA*
[5]*Division of Science, National Astronomical Observatory of Japan, 2-21-1 Osawa, Mitaka-shi, Tokyo, Japan*

ABSTRACT

A primary goal of characterizing exoplanet atmospheres is to constrain planetary bulk properties, such as their metallicity, C/O ratio, and intrinsic heat. However, there are significant uncertainties in many aspects of atmospheric physics, such as the strength of vertical mixing. Here we use `PICASO` and the `photochem` model to explore how atmospheric chemistry is influenced by planetary properties like metallicity, C/O ratio, T_{int}, T_{eq}, and K_{zz} in hydrogen-dominated atmospheres. We vary the T_{eq} of the planets between 400 K- 1600 K, across "cold","warm," and 'hot' objects. We also explore an extensive range of T_{int} values between 30-500 K, representing sub-Neptunes to massive gas giants. We find that gases like CO and CO_2 show a drastically different dependence on K_{zz} and C/O for planets with cold interiors (e.g., sub-Neptunes) compared to planets with hotter interiors (e.g., Jupiter mass planets), for the same T_{eq}. We also find that gases like CS and CS_2 can carry a significant portion of the S-inventory in the upper atmosphere near $T_{eq} \leq 600$ K, below which SO_2 ceases to be abundant. For solar C/O, we show that the CO/CH_4 ratio in the upper atmospheres of planets can become ≤ 1 for planets with low T_{eq}, but only if their interiors are cold ($T_{int} \leq 100$ K). We find that photochemical haze precursor molecules in the upper atmosphere show very complex dependence on C/O, K_{zz}, T_{eq}, and T_{int} for planets with cold interiors (e.g., sub-Neptunes). We also briefly explore fully coupling `PICASO` and `photochem` to generate self-consistent radiative-convective-photochemical-equilibrium models.

1. INTRODUCTION

Major goals of characterizing exoplanet atmospheres are to understand the formation and evolutionary history of planets. This process involves observing exoplanetary atmospheres and intrepreting these observations to estimate some key bulk planetary parameters, like metal enrichment of the atmosphere, which can be used to understand their formation scenario and evolutionary history. However, our interpretation of observational data of exoplanetary atmospheres requires a robust understanding of the various physical and chemical processes ongoing in the planet's atmosphere. In this work, we explore how a series of atmospheric processes can affect our interpretation of exoplanet atmospheric observations. We explore how these atmospheric processes specifically impact atmospheric chemistry, which is a crucial link between understanding exoplanetary atmospheres and constraining their formation and evolutionary processes.

There has been a considerable amount of modeling work revolving around the idea that planets retain some amount of information about their formation scenario and subsequent evolution in their current state (e.g., Öberg et al. 2011; Mollière et al. 2022; Mordasini et al. 2016). This information can be retained within important planetary parameters like the planetary radius, bulk metal enrichment, elemental abundance ratios, internal heat flux of the planet, etc. (e.g., Madhusudhan 2012; Fortney et al. 2007; Öberg et al. 2011; Mollière et al. 2022). For transiting planets, parameters like planetary mass and radius are directly measurable. But other critical parameters like bulk metal-enrichment, bulk elemental abundance ratios, and internal heat flux

samukher@ucsc.edu

of planets need to be inferred by observing and understanding their atmospheres. As planetary atmospheres are quite complex, drawing inferences about their bulk properties requires a detailed understanding of the multiple interconnected physical processes at play.

JWST observations have opened a new era of precision chemical analysis of transiting planet atmospheres (e.g., Rustamkulov et al. 2022; Ahrer et al. 2022; Alderson et al. 2022; Feinstein et al. 2022; Tsai et al. 2023b; Kirk et al. 2024; Thao et al. 2024; Welbanks et al. 2024; Sing et al. 2024; Beatty et al. 2024; Bell et al. 2023; Grant et al. 2023; Fu et al. 2024; Radica et al. 2023; August et al. 2023; Schlawin et al. 2024; Xue et al. 2024; Inglis et al. 2024; Bean et al. 2023; Gagnebin et al. 2024). This is especially interesting because the atmospheric chemistry of planets with H/He atmospheres (from giant planets down to sub-Neptunes) is sensitive to three key planetary parameters – 1) bulk metal-enrichment (or metallicity), 2) bulk elemental abundance ratios, and 3) internal heat flux of planets (e.g., Fortney et al. 2020; Mollière et al. 2015).

The metallicity of a planet's atmosphere is defined as $(X/H)_{\mathrm{planet}}/(X/H)_{\mathrm{sun}}$, where X represents the number of atoms of a certain element (like C-, O-, S-, etc) in the object and H is the number of hydrogen atoms. Therefore a planet with higher metallicity will have significantly different atmospheric chemical composition than one with lower metallicity. Two planets with the same metallicity might have the "metals" distributed differently among various elements. For example, one planet can have a higher C/H ratio and lower O/H ratio than the other and yet maintain the same bulk metallicity (e.g., Madhusudhan 2012; Moses et al. 2013a). These abundance ratios are important potential markers of the formation location of planets because of the presence of various ice lines in propoplanetary disks (e.g., Öberg et al. 2011; Mollière et al. 2022; Mordasini et al. 2016). It is clear and well-studied how both of these bulk parameters can affect atmospheric chemistry especially if the atmosphere is in thermochemical equilibrium throughout (e.g., Visscher & Fegley 2005; Visscher et al. 2006; Goyal et al. 2018; Mollière et al. 2015; Lodders 2004; Lodders & Fegley 2002). However, studies of solar system giant planets and brown dwarf atmospheres have shown that disequilibrium chemical processes in addition to thermochemistry can play a significant role across planetary atmospheres (e.g., Zhang 2020; Hubeny & Burrows 2007; Karalidi et al. 2021; Mukherjee et al. 2023; Miles et al. 2020; Phillips et al. 2020; Tsai et al. 2017; Moses et al. 2011; Mukherjee et al. 2024; Venot et al. 2012; Drummond et al. 2016).

The chemical structure of a planet's atmosphere is shaped by a number of other physical processes too, namely – 1) atmospheric mixing, 2) photochemistry, 3) condensation, and 4) molecular diffusion. As a result, the photospheric abundance of a gas like CH_4 is not only controlled by the metallicity, C/O ratio, and heat flux from the deep interior of the planet but also by parameters like the stellar UV flux incident on the planet along with atmospheric properties like strength of vertical and horizontal dynamics in the atmosphere (e.g., Tsai et al. 2021, 2023c; Moses et al. 2011; Fortney et al. 2020; Tsai et al. 2023a). Molecular diffusion is an important process controlling the chemical nature of atmospheres at very low pressures but the importance of this process is often overshadowed by photochemical processes, especially in highly irradiated giant exoplanets (e.g., Tsai et al. 2021). Atmospheric mixing, photochemistry, condensation, and internal heat flux of exoplanets remain the least understood/constrained processes/parameters in exoplanet atmospheres. We briefly explain these processes here.

Atmospheric Mixing – Atmospheres of planets are dynamic, not static, in nature. This dynamics can play out in three dimensions causing both vertical and horizontal bulk transport of gases and aerosols in atmospheres (e.g., Showman et al. 2009; Menou & Rauscher 2009; Steinrueck et al. 2019; Roth et al. 2024). As a result, photospheric abundances of gases such as CH_4, CO, NH_3 can be significantly altered depending on the strength of dynamics in the atmosphere (Cooper & Showman 2006; Drummond et al. 2016; Steinrueck et al. 2019; Mendonça et al. 2018; Drummond et al. 2018, 2020; Zamyatina et al. 2023; Lee et al. 2023). 3D models of tidally locked close-in giant exoplanets have revealed three major types of transport operational in their atmospheres – 1) vertical transport, 2) day-to-night transport, and 3) pole-to-equator transport. Vertical transport can lift gases and aerosols from the deeper parts of the atmosphere across several pressure scale-heights, while the day-to-night winds can transport gases from the hotter day-side of the planet to their colder night-side. Clearly, a full understanding of the role of atmospheric dynamics on planet-wide chemistry requires the use of 3D models to explore vast swathes of the multidimensional parameter space involved. This vast parameter space includes dimensions like the stellar flux incident on the planet, the planet's gravity, atmospheric composition, rotational period, interior properties such as interior heat flux, cloud composition, etc. The computational run times involved in 3D atmospheric models often prohibit a full scale parameter space exploration.

However, 1D models can somewhat capture the vertical transport operating in these atmospheres by simplifying the transport as a diffusive process, parametrized with the 1D eddy diffusion coefficient– K_{zz}. K_{zz} is defined as $v_{\mathrm{mix}}L_{\mathrm{mix}}$, where v_{mix} is the typical velocity of transport and L_{mix} is the typical length-scale at which this bulk transport is operational (Allen et al. 1981). But, observational constraints on K_{zz} are very weak. Recently, several studies have constrained K_{zz} to a certain extent in brown dwarf atmospheres with ground-based and space-based data (e.g., Miles et al. 2020; Mukherjee et al. 2022; Madurowicz et al. 2023; Beiler et al. 2023; Mukherjee et al. 2024; Kothari et al. 2024) but we have only started to constrain it for irradiated planets (e.g., Sing et al. 2024; Welbanks et al. 2024; Kawashima & Min 2021). Various 3D and 2D modeling efforts have found a large range of K_{zz} values in model atmospheres (e.g., Tan 2022; Parmentier et al. 2013; Komacek et al. 2019; Tsai et al. 2023c; Freytag et al. 2010; Menou 2019), keeping the parameter uncertain by several orders of magnitude in irradiated planets. It is important to especially mitigate this uncertainty due to the influence of K_{zz} on key gas abundances that are used to infer bulk properties of planets such as C/O or metallicity.

Internal Heat Flux – As planets evolve, they slowly lose their gravitational heat of formation to space. This energy is carried from the deep interior through convection to the deep atmosphere up to the point where the atmosphere is opaque at all wavelengths (e.g., Fortney et al. 2007). Beyond that, the heat is lost to space via radiation in the partially or fully optically thin radiative atmosphere. Therefore, detailed properties of the atmosphere, such as its composition and thermal structure, control the rate of cooling of the whole planet over its entire lifetime. This rate of cooling, in turn, also controls the contraction of the planet over time. Additionally, external energy sources like tidal heating can also deposit energy to the deep interior of the planet, the extent of which depends on various orbital and bulk planet properties.

The internal heat flux cannot be measured directly through transmission and emission spectroscopy of close-in exoplanet atmospheres because it typically only alters the temperature structure of the planet where its atmosphere is optically thick, leading to little or no affect on its photospheric temperatures. However, internal heat flux can indirectly affect the photospheric chemical abundances due to the vertical mixing phenomenon discussed previously (e.g., Fortney et al. 2020; Agúndez et al. 2014). If gases are mixed up to the photospheres of the planets from the deep optically thick atmosphere,

where internal heat flux affects chemistry, then they can alter the observable photospheric chemistry of the planet and let us infer the internal heat flux of the planet as well. This works for gases which are stable for long times and not chemically destroyed in the photosphere immediately after being transported. Gases such as CO and N_2 fit into this category as destroying them chemically at low temperature photospheres and converting them to gases like CH_4 and NH_3 is generally energetically prohibitive. Therefore, photospheric abundances of such gases are strongly influenced by the internal heat flux of the planet. Recently, *JWST* transmission spectroscopy observations of WASP-107b were used to constrain its internal heat flux by Welbanks et al. (2024) and Sing et al. (2024). Both of these analysis revealed a high T_{int} (≥ 345 K), which was interpreted as evidence for tidal heating of the planet's interior. Similar constraints on other transiting planets have also been obtained using *HST* (e.g., Barat et al. 2024). These studies are an excellent example of how understanding atmospheric chemistry can reveal details of close-in giant planet evolution.

The internal heat flux of a planet at a given age depends on the mass of the planet. For example, at a similar age, a more massive planet is expected to have a hotter interior than a less massive planet, if there are no external perturbations on the planet such as tidal heating. However, interior temperatures also depend on aspects of atmospheric physics. For example, the strength of vertical mixing plays a major role in affecting both atmospheric clouds and chemistry. Both of these things can delay/accelerate the cooling of planets over time (e.g., Morley et al. 2024; Saumon & Marley 2008).

Photochemistry – Planets can have significant X-ray and UV photons incident on them from their host stars. These photons can cause the photolysis of weakly bonded molecules such as CH_4, NH_3, H_2S, etc. in the upper atmosphere (e.g., Moses et al. 2011; Tsai et al. 2021, 2023c,a; Wogan et al. 2023; Hu 2021; Venot et al. 2012; Moses et al. 2016). This can trigger a whole new set of chemical reactions altering photospheric composition. The first concrete evidence of a photochemical by-product was confirmed with *JWST* in WASP-39b by the presence of photochemically produced SO_2 in its upper atmosphere (Tsai et al. 2023c; Ahrer et al. 2022; Alderson et al. 2022; Rustamkulov et al. 2022). While significant modeling work on understanding photochemistry in close-in planets has been done previously (e.g., Moses et al. 2011; Tsai et al. 2021, 2023c,a; Crossfield 2023; Zahnle et al. 2009; Venot et al. 2012), this *JWST* work demonstrated that photochemistry cannot be neglected while modeling the photospheric chemical na-

ture of planets and using abundances to infer planetary properties.

Additionally, photolysis of gases like CH_4 and NH_3 can lead to the production of C- and N- bearing molecules like C_2H_2 and HCN. These gases in the upper atmospheres of H_2/He-rich atmospheres can act as precursors for further reactions to form photochemical hazes (e.g., Morley et al. 2013, 2015; Fortney et al. 2013; Gao et al. 2020). The optical properties of these hazes are such that they can play a significant role in shaping the observable spectra of exoplanet atmospheres (e.g., Lavvas & Koskinen 2017; Kawashima & Ikoma 2018; Ohno & Kawashima 2020; Steinrueck et al. 2023; Arfaux & Lavvas 2022; Morley et al. 2015).

The discussion above shows that the observational data from transiting planets today is at a stage where its chemistry can be leveraged to not only understand atmospheric elemental compositions of planets but also should be leveraged to understand exoplanetary atmospheric processes better as well. These include constraining key atmospheric processes such as atmospheric dynamics and parameters like internal heat flux of planets. Therefore, it is necessary to explore how atmospheric dynamics and internal heat flux can influence the photospheric abundance of gasses in exoplanets with varying bulk properties such as equilibrium temperature, C/O ratio, metallicity, and varying amounts of incident UV flux. It is also important to identify the key molecules that can produce the best constraints on very uncertain parameters like K_{zz} in different parts of this vast parameter space.

This paper presents a broad parameter space study to address these questions. Our work is applicable to a wide variety of planets. In terms of internal heat flux, this includes sub-Neptune mass planets with lower internal heat fluxes, to Jupiter mass giant planets with much hotter interiors. In terms of planetary temperatures, we explore planets between cold giant planets ($T_{eq} \sim$ 400 K) to hot Jupiters ($T_{eq} \sim$ 1600 K). We also explore the atmospheric chemistry of planets with varying C- and O-abundances. We also investigate the effects of a wide range of the atmospheric mixing parameter K_{zz} and atmospheric metallicity on the chemistry of these planets.

We describe our modeling setup in §2 followed by the results presented in §3. We discuss the limitations and caveats in this analysis in §4 followed by summarizing our key conclusions in §5.

2. MODELING

The aim of the modeling presented in this work is to explore a significant parameter space of properties that can influence atmospheric chemistry of transit-
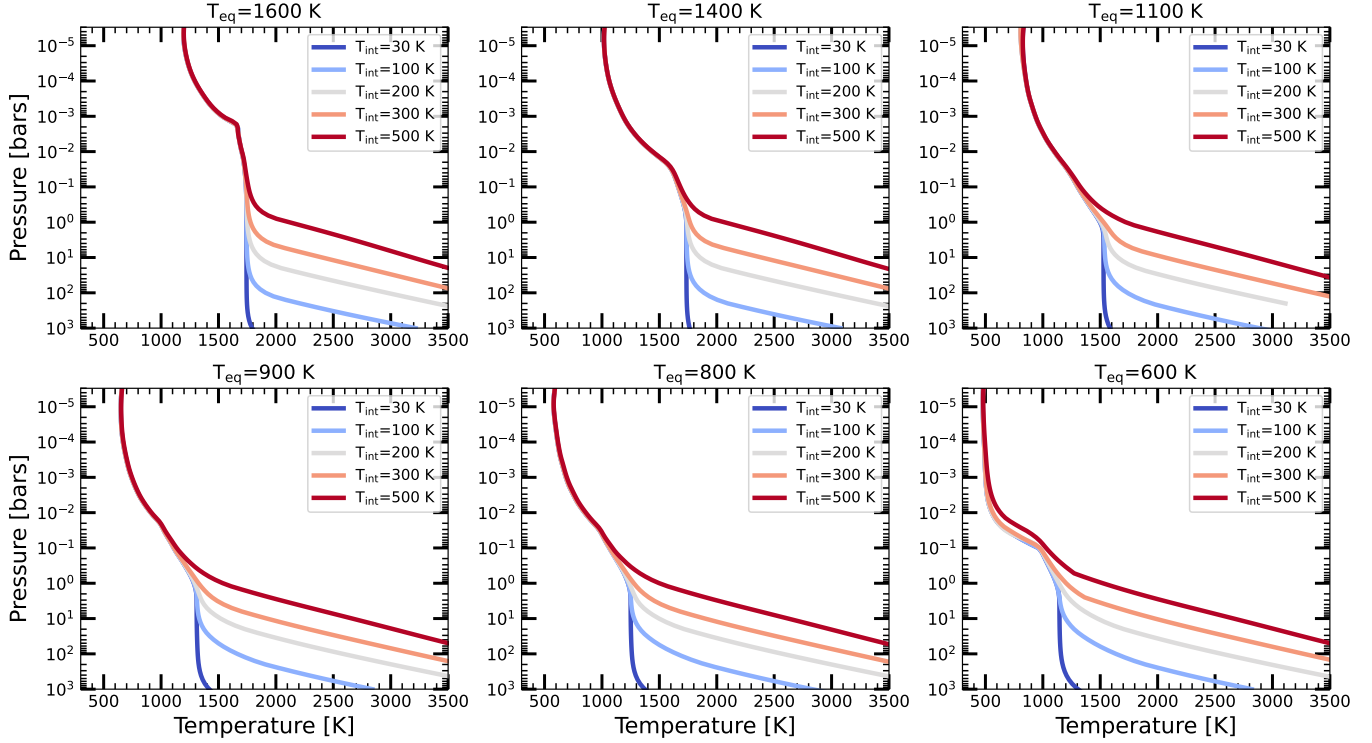
ing planets with H/He atmospheres. The parameters we consider in this study are the equilibrium temperature (T_{eq}), interior heat flux through the parameter T_{int}, strength of vertical mixing parameterized with K_{zz}, C/O ratio, and metallicity. The modeling setup to achieve this parameter space exploration can be divided into two different components – 1) 1D radiative–convective atmospheric modeling, and 2) chemical kinetics modeling. We describe each component in detail below.

2.1. 1D Radiative–Convective Equilibrium Models

We use the 1D radiative–convective equilibrium model PICASO (Mukherjee et al. 2023; Batalha et al. 2019) to generate atmospheric temperature–pressure ($T(P)$) profiles for irradiated planets. We generate the $T(P)$ profiles for a planet with gravity= 4.5 ms^{-2} around a star with T_{eff}=5327 K, $log(g)$=4.38, [M/H]= -0.03, and Radius= 0.932 R$_\odot$. These system parameters are chosen to be the same as WASP-39b. We divide the planet atmosphere into 91 plane-parallel levels (90 layers) logarithmically spaced in pressure between 10^{-6} to 100/5000 bars. We generate the $T(P)$ profiles using the heat recirculation factor rfacv= 0.5, which corresponds to the case of full heat redistribution across the planet. We place the planet at different distances from the star such that the T_{eq} of the planet (assuming 0 albedo) are 1600 K, 1400 K, 1100 K, 900 K, 800 K, 600 K, and 400 K. For each of these cases, we generate 5 different cases with different T_{int} values of 30 K, 100 K, 200 K, 300 K, and 500 K. The lowest value, 30 K, is representative of Gyr+ old sub-Neptunes (Lopez & Fortney 2014). Jupiter's value today is 100 K. More massive, younger, or inflated gas giants (such as by tidal heating or other factors) would have larger T_{int} values (Fortney et al. 2020). The equilibrium chemistry calculation and gaseous opacities used for computing these $T(P)$ profiles are the same as used in Mukherjee et al. (2024). Figure 1 shows these generated $T(P)$ profiles where each panel corresponds to a different T_{eq} case. Note that these radiative–convective–thermochemical–equilibrium (RCTE) models were calculated by including TiO and VO opacities, which are known to cause thermal inversions in atmospheres which have $T_{eq} \geq$ 1600 K. We generate these $T(P)$ profiles at 10×solar metallicity and solar C/O ratio (C/O= 0.458 (Lodders et al. 2009)) assuming thermochemical equilibrium throughout the atmosphere.

2.2. Chemical Kinetics Modeling

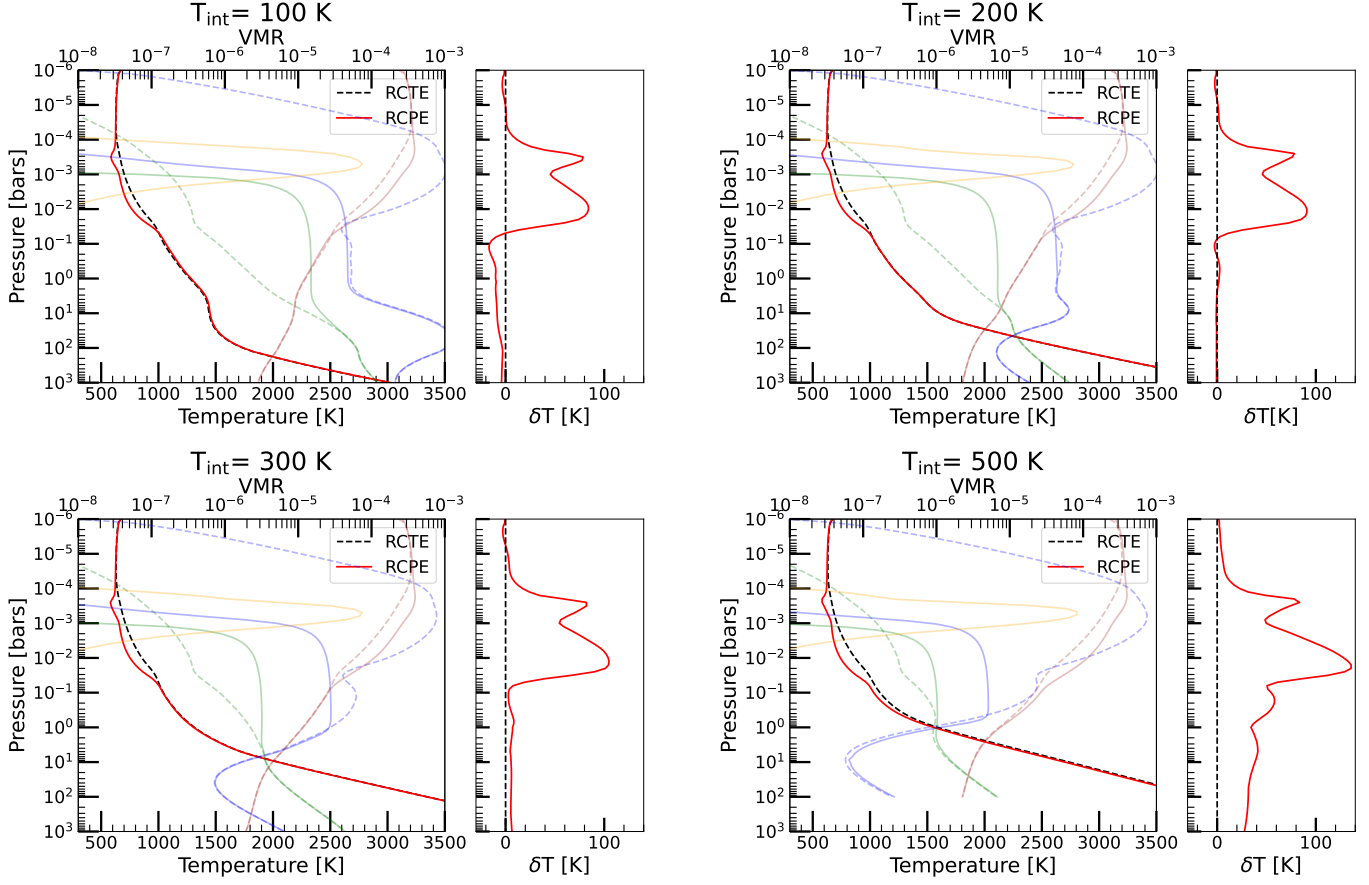To simulate disequilibrium chemistry within our model atmospheres, we use the python wrapped *Pho-*

Figure 1. $T(P)$ profiles computed using 1D radiative–convective–equilibrium modeling at various T_{eq} and T_{int} values are shown. Each panel shows the model $T(P)$ profiles computed for a T_{eq} value at five different T_{int} values between 30 K and 500 K. The six panels correspond to T_{eq}= 1600 K, 1400 K, 1100 K, 900 K, 800 K, and 600 K. The kink at 1 mbar and 1700 K in the hottest models (T_{eq}=1600 K) is due to a small amount of TiO opacity. All the $T(P)$ profiles have been computed for a planet with gravity=4.5 ms^{-2} around a star with T_{eff}= 5326.6 K, $log(g)$=4.38, and Radius=0.93$R_\odot$.

tochem[1] chemical kinetics model (Wogan et al. 2023, 2024). We use the $T(P)$ profiles computed using the method described in the previous section as inputs in the *Photochem* package. In addition to the *Photochem* package, we use the *Cantera* software (Goodwin et al. 2023) to simulate thermochemical equilibrium in the very deep atmosphere of the model planet atmospheres. For each model, we use the quench time approximation with chemical timescales from Zahnle & Marley (2014) to determine the quench pressures of key gases like CH$_4$, NH$_3$, CO$_2$, etc. At atmospheric levels with pressures much greater than the highest quench pressures among these gases (5-8 atmospheric levels deeper than the highest quench pressure), we use *Cantera* to calculate the thermochemical equilibrium state of the atmospheres. At pressures smaller than this pressure level we use *Photochem* to simulate chemical disequilibrium with its kinetics calculations. The convergence criteria used in our photochemistry modeling is presented in §4.4. This modeling setup helps us in calculating photochemical models significantly quicker than using the

chemical kinetics calculation for all the pressure layers in the atmosphere including the very high pressure and high temperature deep atmosphere where chemical reactions are expected to be very fast. The setup saves computational time by preventing the kinetics model from taking extremely small time steps to model the very rapid chemical reactions in the very deep atmosphere, which is bound to remain in thermochemical equilibrium anyway. To maintain sufficient accuracy in the 1D chemical kinetics calculations, we interpolate the atmospheric $T(P)$ profiles with 91 pressure levels to a finer grid of pressures with 180 pressure levels before ingesting them within *Photochem*.

For a given metallicity, we scale the C/H, O/H, N/H, S/H from the solar values with the metallicity factor in our model. To change the C/O ratio for a given metallicity, we change both the C/H and O/H such that (C+O)/H remains the same. This is crucial to maintain the same atmospheric metallicity while changing the C/O ratio of the atmosphere. To account for O-atoms locked up in various expected condensates such as silicates, we remove 20% of the O from the atmospheric gas phase.

[1] https://github.com/Nicholaswogan/photochem

Figure 2. $T(P)$ profiles computed assuming radiative–convective–thermochemical equilibrium (RCTE) and radiative–convective–photochemical equilibrium (RCPE) are shown with dashed black lines and solid red lines, respectively. The assumed T_{eq}, [M/H], and C/O of the model is 800 K, +1.0, and 1×solar, respectively. Each panel corresponds to a different T_{int} from 100 K to 500 K. The faded lines show the volume mixing ratios (top x-axis) of CH_4, NH_3, SO_2, and CO_2 in blue, green, orange, and brown, respectively. The dashed VMR profiles are from the RCTE models whereas the solid VMR profiles correspond to the RCPE models. The narrower panel accompanying each of the four panels shows the different in the $T(P)$ profile between the two modeling assumptions in each case as a function of pressure.

`PICASO` and *Photochem* can be fully and iteratively coupled, instead of `PICASO` using pre-computed equilibrium chemistry tables (e.g., Marley et al. 2021; Fortney et al. 2007; Morley et al. 2013; Mukherjee et al. 2023; Morley et al. 2014; Fortney et al. 2005, 2008), or using on-the-fly non-equilibrium chemistry due to mixing implemented using quench time approximation (e.g., Mukherjee et al. 2022, 2024). Figure 2 illustrates the difference in the $T(P)$ profile between a fully self-consistent treatment of photochemistry within the climate model and a profile computed assuming radiative–convective–thermochemical equilibrium (RCTE) for the same set of physical parameters – T_{eq}= 800 K, [M/H]=+1.0, and C/O=1×solar. The radiative–convective–photochemical equilibrium (RCPE) (e.g., Bell et al. 2023; Welbanks et al. 2024) model was computed by combining the *Photochem* kinetics model (Wogan et al. 2023) calculations within the `PICASO` cli-

mate calculation framework. Each panel of Figure 2 illustrates the difference between the $T(P)$ profiles for four different T_{int} values of 100 K, 200 K, 300 K, and 500 K with K_{zz}=10^9cm^{2}s^{-1}. The RCTE (dashed) and RCPE (solid) chemical profiles for CH_4 (blue), NH_3 (green), and SO_2 (orange) are also shown in each panel. It is clear that for lower values of T_{int}, the maximum difference in the $T(P)$ profile is typically around $\sim$ 100 K in the 0.1 mbar to 0.1 bar range. Whereas as the T_{int} increases, small differences of the order of $\sim$ 20 K remain in the profiles, even at deeper pressures till around 100 bars. This shows that the corrections in the $T(P)$ profiles due to radiative feedback from the changed atmospheric chemistry due to vertical mixing or photochemistry is an important effect, especially for high T_{int} values. This will be especially relevant for interpreting emission spectra of planets. Even though this work focuses on modeling disequilibrium chemistry ef-

fects, we choose not to use the RCPE approach for our $T(P)$ profile calculations mainly because this can vastly increase the computational time involved in running a 1D model. We make this choice because we focus on transmission spectroscopy in this paper where temperature has a relatively small effect compared to emission spectroscopy. Moreover, in our parameter space exploration, we vary both metallicity and C/O ratio but we do not self-consistently include the variation of the $T(P)$ profile with metallicity and C/O in our models. We discuss the effect of these approximations further in §4.

Our parameter space exploration (§3.1) is focused on investigating roles of C/O and K_{zz} across planets with different T_{eq} and T_{int}. For this, we run photochemical models for 13 different C/O values between a range of C/O ratios starting from 0.0458 to 1.125 with a step size of 0.0916, exploring the very O- rich to very C- rich atmospheres at $10\times$solar metallicity. We also vary the K_{zz} parameter between 10^6 to 10^{13} cm^{2}s^{-1} with steps of 1 in the $\log_{10}(K_{zz})$ space. This range reflects the huge range of uncertainty on this parameter covering cases of very slow vertical mixing to rapid mixing. Therefore, in the first parameter space exploration we compute chemical kinetics models for each $T(P)$ profile shown in Figure 1 for a range of C/O and K_{zz}. For each model, we use the X-ray/UV spectra for WASP-39b used in Tsai et al. (2023c). Note that we *do not* scale the UV flux incident on the planet as we move the planet closer or further away from the star to change its T_{eq}. We make this choice as we want to explore the chemical trends in atmospheres as a function of varying T_{eq} with a uniform X-ray/UV flux incident on the planet. This is to avoid changing this additional parameter while we sweep the T_{eq} parameter space. Our second part of the parameter space exploration (§3.2) is focused on exploring the role of metallicity, C/O, K_{zz}, and T_{int} on the photospheric abundances but at a fixed T_{eq}. We present the trends in photospheric abundance with varying T_{eq} in §3.3 and the sensitivity of the transmission spectra to various planetary parameters in §3.4. We also present trends in our estimates of photochemical precursors to haze/soot across the parameter space in §3.5.

3. RESULTS

3.1. *Exploring how abundances depend on K_{zz}, C/O, and T_{int} across different T_{eq}*

In this section, we present the variation of key molecular abundances at the pressures typically probed by transmission spectroscopy for transiting planets. The top three panels of Figure 3 shows an example of how CH$_4$ abundance profiles change with changing K_{zz}, T_{int}, and C/O, respectively for a planet with $T_{eq}=$ 800 K.

The middle and bottom three panels of Figure 3 shows the same but for SO$_2$ and CO$_2$, respectively. The approximate pressure range probed by transmission spectroscopy is shown with the red shaded region in each panel. It is clear that T_{int}, K_{zz}, and C/O can cause significant changes to the photospheric abundance of gases like CH$_4$ but Figure 3 also shows that not all gases are equally sensitive to all of these parameters.

In order to present the trends in photospheric abundance of gases with variations in these parameters, we use a box-shaped kernel between 10 mbar and 0.1 mbar which is also the region shaded in Figure 3. For each gas abundance profile, we calculate the logarithm of the average photospheric abundance using,

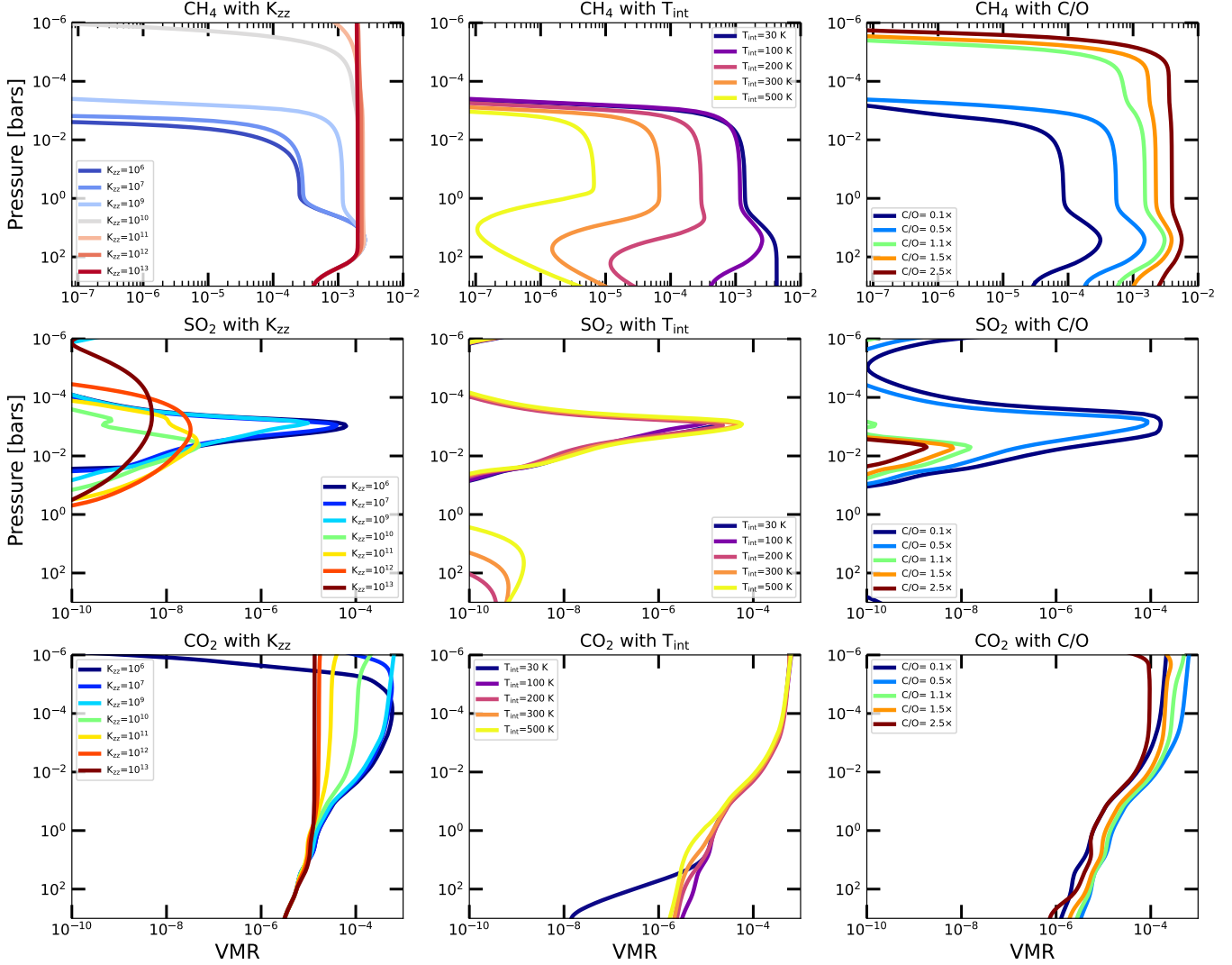$$log_{10}(X_{w}) = \frac{\int_{P_1}^{P_2} \log_{10}(X(p))dp}{\int_{P_1}^{P_2} dp} \quad (1)$$

where $X(P)$ is the volume mixing ratio profile of gas X, p_1 is 10 mbar, and p_2 is 0.1 mbar. This range covers a typical pressure range probed by transmission spectroscopy. We present the trends in X_w for various gases in the following sections.

3.1.1. *Trends in CH$_4$, CO, H$_2$O, and CO$_2$*

3.1.1.1. *CH$_4$ —*

CH$_4$ is one of the major C-bearing gases in giant planet atmospheres. Figure 4 shows the quantity X_w for CH$_4$ with a heat map as a function of K_{zz} and C/O at various T_{eq} and T_{int} values. Each row in Figure 4 corresponds to a different T_{eq} from 1100 K to 600 K, while each column corresponds to a different T_{int} from 30 K to 500 K. We do not show the heat maps computed for T_{eq} of 1400 and 1600 K here as they are qualitatively similar to the 1100 K case. The left most part of each sub-figure shows the trend in CH$_4$ X_w in the case of thermochemical equilibrium.

Figure 4 shows that for $T_{eq} \geq$ 1100 K, CH$_4$ only becomes abundant in the photosphere when the atmosphere is very C- rich with C/O $> 2\times$solar or when K_{zz} $\geq 10^{12}$ cm^{2}s^{-1}. Madhusudhan (2012) found very similar C/O dependence for CH$_4$, albeit their calculations assumed thermochemical equilibrium. The amount of CH$_4$ in the photosphere for these hotter planets shows some T_{int} dependence when the vertical mixing is extremely vigorous with $K_{zz} \geq 10^{12}$ cm^{2}s^{-1}. In these cases, a colder interior planet (e.g., $T_{int}=$ 30 K or 100 K) shows higher amount of photospheric CH$_4$ than planets with much hotter interior (e.g., $T_{int}=$ 500 K). This shows that the T_{int} parameter, which mostly affects the $T(P)$ and
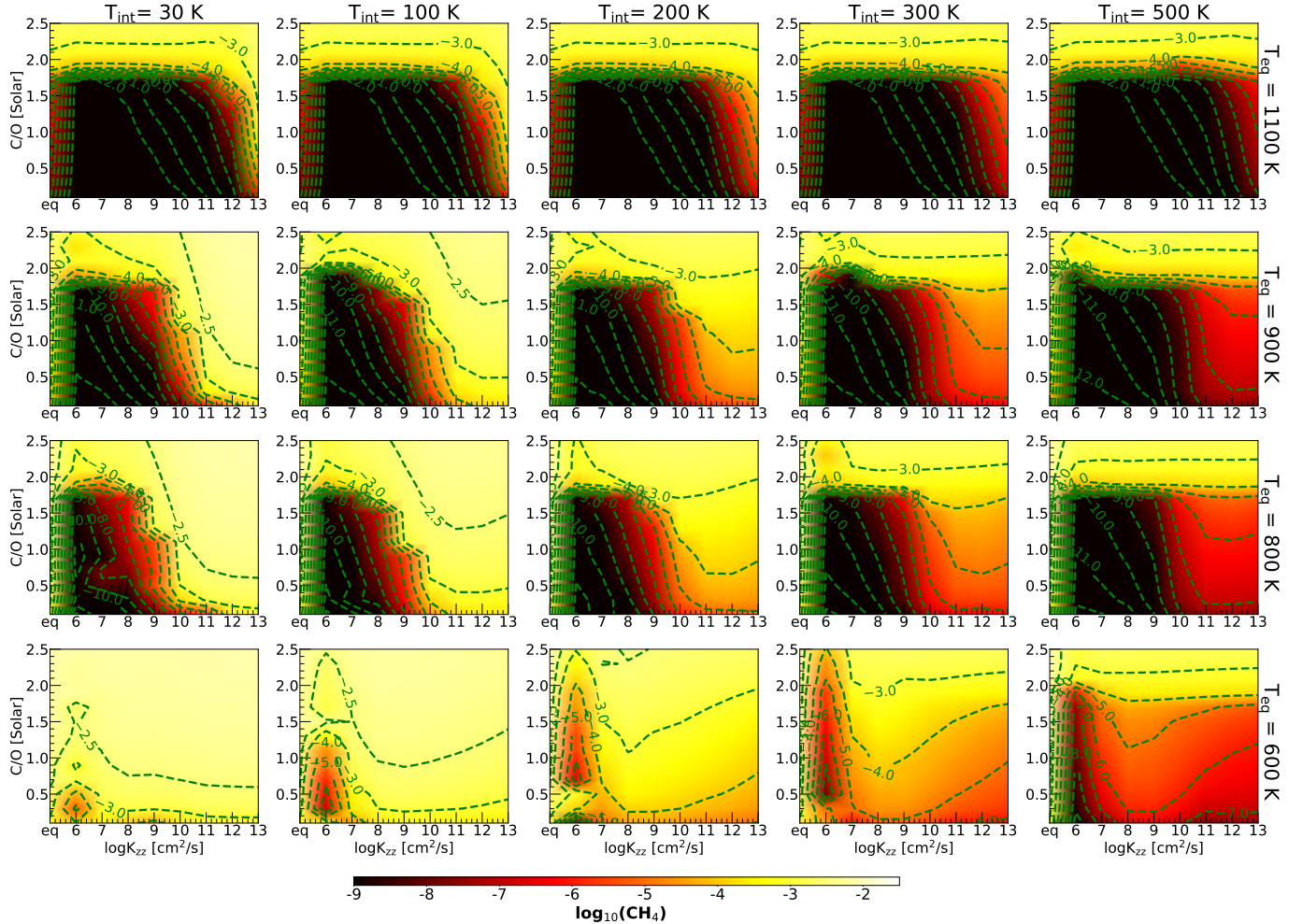
Figure 3. The dependence of chemical abundance profiles on K_{zz}, T_{int}, and C/O are shown in the left, middle, and right columns, respectively. The upper row shows this dependence for CH_4 while the middle and lower rows show this dependence for SO_2 and CO_2, respectively. The pressure values typically probed by transmission spectra are shown with the red shaded region.

chemistry in the deep atmosphere, already starts to affect the CH_4 abundance at much smaller pressures at T_{eq}=1100 K, when mixing is vigorous.

Figure 4 shows that for a given C/O, T_{int}, or K_{zz}, the CH_4 abundance is much higher in the $T_{eq} \leq 900$ K planets than the $T_{eq} \geq 1100$ K planets. For T_{eq}= 900 K, Figure 4 shows that the CH_4 abundance varies very strongly with K_{zz}. For a given C/O, the photospheric CH_4 abundance shows 6-7 orders of magnitude increase with the K_{zz} increasing by 7 orders of magnitude. The abundance of photospheric CH_4 is much lower than the expectations from thermochemical equilibrium for K_{zz} $\leq 10^{11}$cm^{2}s^{-1} when $T_{int} \leq$ 200 K. For stronger vertical mixing, the amount of CH_4 rises to thermochemical equilibrium expectations for these colder interior plan-

ets. Whereas, the CH_4 abundance is always lower than the expected amount from thermochemical equilibrium for hotter interiors for all the K_{zz} values explored in Figure 4. Equal abundance contours plotted on Figure 4 T_{eq}=900 K panels are nearly vertical which suggests that the variation of CH_4 abundance with changing K_{zz} is stronger than its variation with C/O. For a given C/O and K_{zz}, the CH_4 abundance typically decreases by 3-4 orders of magnitude with the T_{int} increasing from 30 K to 500 K for T_{eq}=900 K. Figure 4 shows that the qualitative behavior shown by the CH_4 abundance is very similar between T_{eq}=900 K and T_{eq}=800 K panels except the CH_4 abundances are higher in the T_{eq}=800 K panels than the T_{eq}=900 K panels for a given C/O, T_{int}, and K_{zz} value.
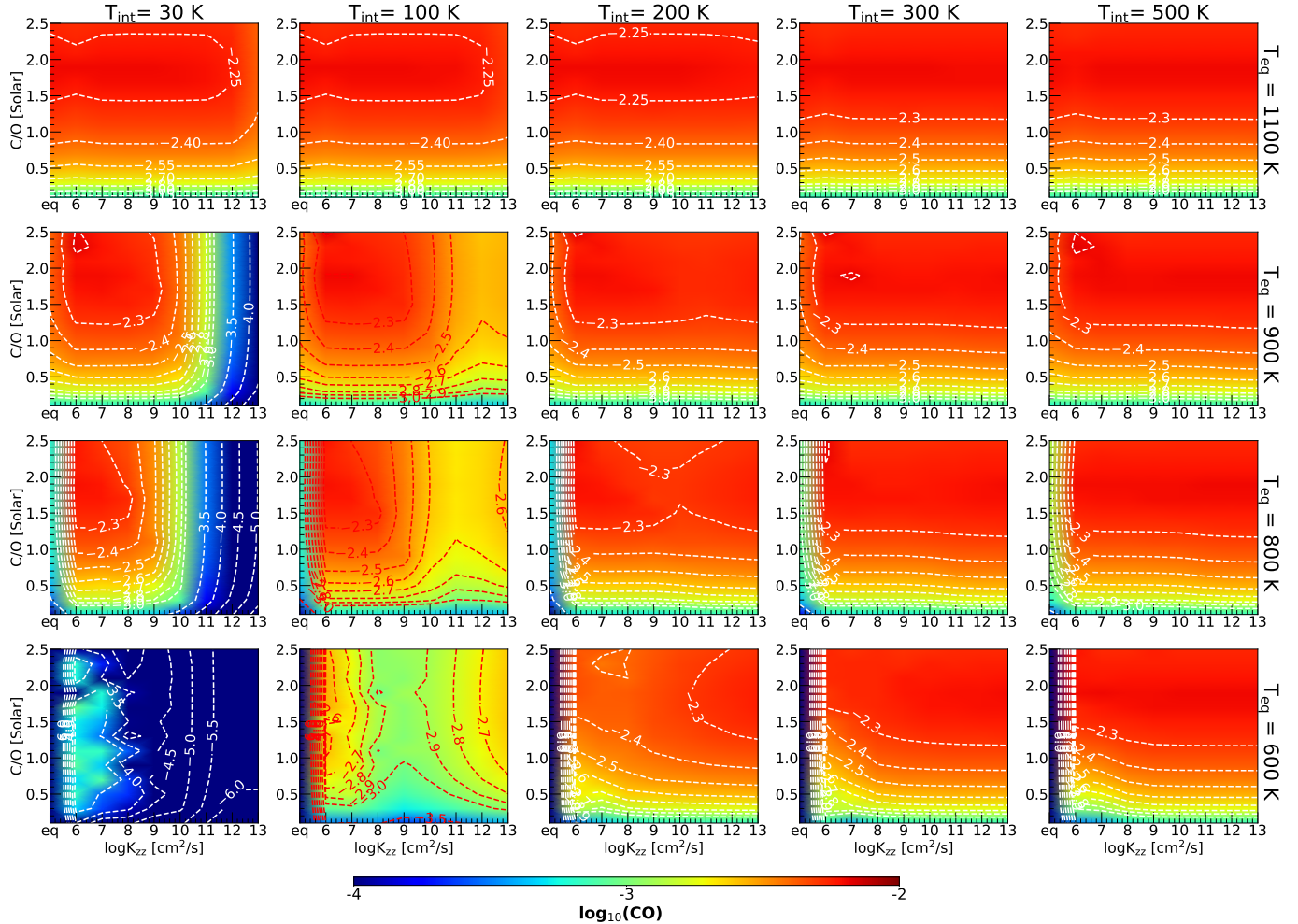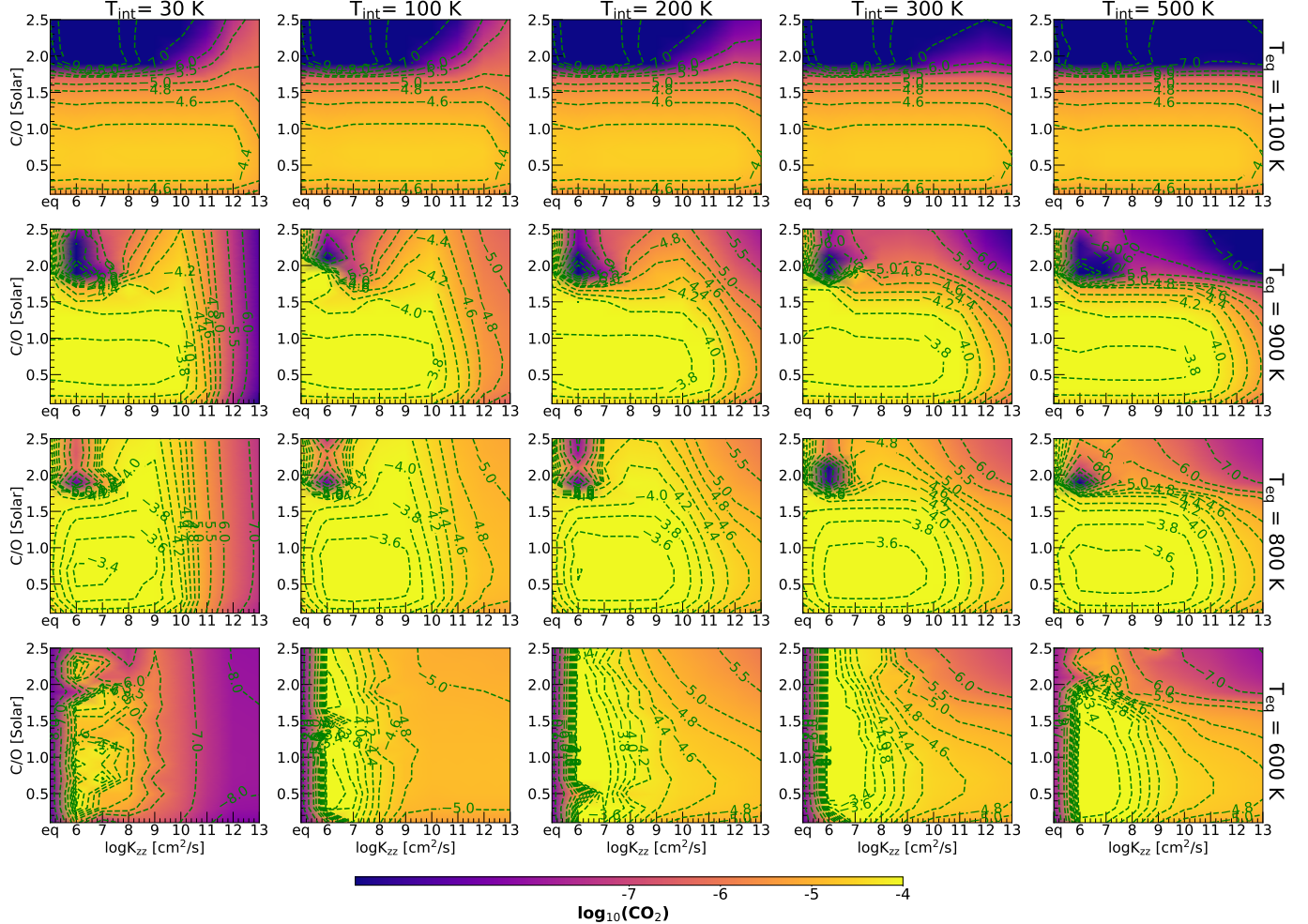
Figure 4. The weighted abundance of CH$_4$ calculated using Equation 1 as a function of C/O and K_{zz} in each panel. Each row corresponds to a different $T_{\rm eq}$ value from 1100 K to 600 K from top to bottom. Each column correspond to a different $T_{\rm int}$ value between 30 K and 500 K from left to right. Note that the C/O is shown relative to an assumed solar value of 0.458 in this plot.

The last row in Figure 4 shows CH$_4$ abundances for $T_{\rm eq}=$ 600 K. For these cold $T_{\rm eq}$ values, CH$_4$ abundance shows a significant increase compared to the $T_{\rm eq}=$ 800 K cases. This increase is especially high for $K_{zz} \lesssim 10^{10} {\rm cm}^2 {\rm s}^{-1}$. Also, the equal abundance contours for $T_{\rm eq}=$ 600 K, are nearly horizontal which shows that the CH$_4$ abundance is much more sensitive to C/O than K_{zz} for these cold planets. At $T_{\rm eq}=$ 600 K, for a given C/O and K_{zz} value, the CH$_4$ abundance shows a 2-3 orders of magnitude decrease with $T_{\rm int}$ increasing from 30 K to 500 K. The equal abundance contours shown in Figure 4 show that while interpreting the C/O of a planet from its measured CH$_4$ abundance, one should be particularly careful in parts of the parameter space where the contours in Figure 4 are not horizontal. This means that the same photospheric CH$_4$ abundance can be a result of a wide range C/O in these parts of the parameter space. This also suggests that the CH$_4$ abundance, if detected, can be a good diagnostic of K_{zz} in

parts of the parameter space where the equal abundance contours are nearly vertical. Figure 4 suggests that CH$_4$ becomes a favorable marker of vertical transport when $T_{\rm eq}$ is between 800–900 K, which is slightly colder than the 'sweet-spot' identified in the 3D models presented in Zamyatina et al. (2023). Note that we have shown these trends at a fixed metallicity (i.e., 10×solar).

3.1.1.2. CO—

Figure 5 presents the X_w for CO across different C/O ratios and K_{zz}. Again, each panel corresponds to a different $T_{\rm eq}$ and $T_{\rm int}$ combination. For $T_{\rm eq}=$ 1100 K, Figure 5 shows that the CO abundance is only sensitive to C/O showing a rapid increase with increasing C/O around C/O∼0.3×solar. Figure 5 suggests that the CO gas can be a great tracer of C/O in planets with $T_{\rm eq} \geq$ 1100 K irrespective of the strength of K_{zz}.
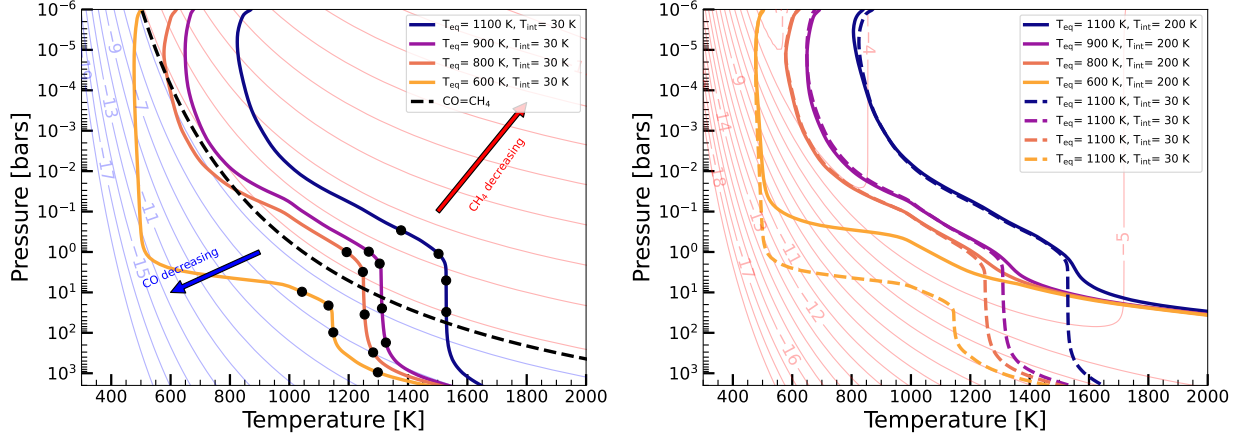
Figure 5. The weighted abundance of CO calculated using Equation 1 has been shown as a heat map as a function of C/O and K_{zz} in each panel. Each row corresponds to a different T_{eq} value from 1100 K to 600 K from top to bottom. Each column correspond to a different T_{int} value between 30 K and 500 K from left to right. Note that the C/O has been shown relative to the assumed solar value of 0.458 in this plot.

The CO abundane for a given C/O also shows almost no T_{int} dependence for $T_{eq} \geq 1100$ K. The difference in CO abundance between the thermochemical equilibrium and disequilibrium chemistry at T_{eq}= 1100 K and 900 K is almost negligible. However, some K_{zz} dependence of CO abundance appears at T_{eq}= 900 K, when $T_{int} \leq$ 100 K. For these cases, CO shows a decrease with increasing K_{zz} when $K_{zz} \geq 10^9 \text{cm}^2\text{s}^{-1}$. This decrease of CO abundance with increasing K_{zz} beyond $10^9\text{cm}^2\text{s}^{-1}$ is much more pronounced when T_{int}=30 K than the case of T_{int}= 100 K. Similar behavior is also shown by the T_{eq}= 800 K models, where the K_{zz} dependence of CO abundance for cold interior planets ($T_{int} \leq$ 100 K) sets in at a slightly lower K_{zz} of $10^8\text{cm}^2\text{s}^{-1}$. This suggests that for planets with T_{eq} at 800 K or 900 K and hot interiors ($T_{int} \geq$ 200 K), CO can be a great tracer of C/O, irrespective of K_{zz} and with minimal dependence on T_{int} as well. But for such planets with cold interiors

$T_{int} \leq$ 100 K, whether CO will trace the C/O of the atmosphere depends largely on the strength of K_{zz}.

The same behavior is not only shown but enhanced further in T_{eq}= 600 K planets shown in the last row of Figure 5. The CO abundance mainly depends on K_{zz} only in these cases for $T_{int} \leq$ 100 K and is dependant only on C/O for $T_{int} \geq$ 200 K. This suggests that for planets with colder T_{eq} ($\leq$ 900 K) and cold interiors ($T_{int} \leq$ 100 K), CO abundance can be a tracer of K_{zz}, whereas for all the other cases of hotter planets or hotter interiors, CO abundance is a great tracer of atmospheric C/O.

The CO abundance in planets with cold interiors and colder T_{eq} values shows a decrease with increasing K_{zz}, beyond a certain K_{zz} value, because their $T(P)$ profiles straddle the CO=CH_4 equal abundance curve (Fortney et al. 2020). This has been shown in Figure 7 right panel, where the black dashed curve shows the CO=CH_4 equal

Figure 6. The weighted abundance of CO_2 calculated using Equation 1 has been shown as a heat map as a function of C/O and K_{zz} in each panel. Each row corresponds to a different T_{eq} value from 1100 K to 600 K from top to bottom. Each column correspond to a different T_{int} value between 30 K and 500 K from left to right. Note that the C/O has been shown relative to the assumed solar value of 0.458 in this plot.

abundance curve and the solid $T(P)$ profiles represent T_{int}=30 K models with T_{eq} lying between 1100 K and 600 K. CO abundance decreases in the bottom left direction of the figure and CH_4 abundance decreases towards the top right direction of the plot. The black points on each $T(P)$ profile show the quench points for CO, when the K_{zz} is 10^6, 10^8, 10^{10}, and 10^{12} cm^{2}s^{-1}. The CO abundance remains almost constant with changing K_{zz} if the quench pressure lie in the CO dominated region, which is the top right part above the CO=CH_4 equal abundance curve. If quenching happens in this region, the quenched CO abundance is expected to be insensitive to K_{zz}. However, if CO is quenched in the lower left half, where CO abundance is rapidly decreasing, then the CO abundance shows a rapid decrease with increasing K_{zz}. This decrease is sharper because of the isothermal nature of the $T(P)$ profile, which are far from

being parallel to the equal abundance contours of CO in this part of the $T - P$ space.

Another important behavior reflected in Figure 5 is that the photospheric CO abundance remains the same between thermochemical equilibrium and chemical disequilibrium for $T_{eq} \geq 900$ K, but for colder planets, the CO abundance in the thermochemical equilibrium cases are smaller than the models with low K_{zz} values ($K_{zz} \leq 10^7$cm^{2}s^{-1}), irrespective of T_{int}. This suggests that even though the CO abundance can act as a tracer of C/O (without any K_{zz} dependence) in planets with hot interiors, disequilibrium chemistry calculations must still be used to interpret the correct C/O of a planet from its measured CO abundance. This behavior is a direct effect of the shape of the $T(P)$ profiles of these planets, when their T_{eq} is ≤ 800 K and can also be understood with the left panel of Figure 7. The $T(P)$ profiles of planets with $T_{eq} \leq 800$ K transition from the CO-

Figure 7. Left panel: The $T(P)$ profiles of planets with T_{int}= 30 K and T_{eq} between 1100 and 600 K are shown with the four solid lines. The black dashed line shows the CO=CH_4 equal abundance curve from chemical equilibrium calculations at [M/H]=+1.0 and C/O=1×solar. Equal abundance contours for CO and CH_4 are shown in blue and red, respectively. The four black markers on each $T(P)$ profile show the quench pressures of CO for 10^6, 10^8, 10^{10}, and 10^{12} cm^{2}s^{-1}. **Right panel:** The $T(P)$ profiles of planets with T_{int}= 200 K and T_{eq} between 1100 and 600 K are shown with the four solid lines, whereas the dashed lines show the models for T_{int}= 30 K. Equal abundance contours for CO_2 from thermochemical equilibrium are shown in red.

dominated to the CH_4 dominated regions in the $T-P$ space, as shown in Figure 7. This leads to a sharp decrease in photospheric CO in these objects. However, even for low K_{zz} values (e.g., 10^6 cm^{2}s^{-1}), the CO gets quenched at much deeper pressures, where their $T(P)$ profiles cross equal abundance contours corresponding to higher CO abundance than the low photospheric CO abundance expected from thermochemical equilibrium. As the CO abundance becomes roughly constant on the top right side of the CO=CH_4 line, this doesn't happen when $T_{eq} \geq 900$ K.

3.1.1.3. CO_2 —

Figure 6 shows the X_w for CO_2. At T_{eq}= 1100 K, the CO_2 abundance shows a sharp decrease when C/O $\geq$ 1.9×solar. This behaviour is unlike CO, which doesn't show such a sharp change in its abundance when C/O is $\geq$ 1.9×solar as shown in the top panels of Figure 5. CO_2 shows this sharp decline beyond C/O $\geq$ 1.9×solar due to the unavailability of enough O- atoms to form CO_2 when the C/O is approaching 1. At this T_{eq}, CO_2 remains practically independent of K_{zz} across all T_{int} values, except for some slight K_{zz} sensitivity for $K_{zz} \geq$ 10^{12}cm^{2}s^{-1}. However, Figure 6 also shows that the photospheric CO_2 abundance doesn't show much change with changing C/O between 0.3×solar$\leq$C/O$\leq$1.2×solar across all T_{int} values. This might limit the utility of CO_2 as a C/O diagnostic for this range of C/O values. This suggests the CO_2 can be a good tracer for C/O in these $T_{eq} \geq 1100$ K planets, except for very high strengths of

vertical mixing or for 0.3×solar$\leq$C/O$\leq$1.2×solar. CO_2 also doesn't show much dependence on T_{int} at this T_{eq}.

CO_2 has a larger K_{zz} dependence for planets with $T_{eq} \leq$ 900 K. For T_{eq}= 900 K and T_{int}= 30 K, the CO_2 remains insensitive to K_{zz} for $K_{zz} \leq 10^9$cm^{2}s^{-1}. However, the CO_2 shows very strong sensitivity to K_{zz} for higher values of K_{zz} causing the CO_2 abundance to drop by two orders of magnitude with K_{zz} increasing by four orders of magnitude. This behavior is present for hotter T_{int} models as well, albeit with a slower decrease of CO_2 abundance with increasing K_{zz}. With increasing T_{int}, the K_{zz} value at which CO_2 transitions from being insensitive to sensitive to K_{zz} also shifts slowly towards higher value. The T_{eq}= 800 K models shown in the third row of Figure 6, also show the same qualitative behavior as the T_{eq} =900 K models, but with an even stronger dependence of CO_2 abundance on K_{zz} once the K_{zz} value is higher than the "transition" K_{zz} value. This behavior can be readily understood with the right panel of Figure 7, which shows the $T(P)$ profiles for T_{int}= 200 K and 30 K models with solid and dashed lines, respectively. Each profile corresponds to a different T_{eq}. The equal abundance contours for CO_2 from thermochemical equilibrium are shown with the red lines. For planets with hotter T_{eq} or hotter T_{int}, most of the $T(P)$ profile lie in parts of the $T-P$ space where the CO_2 equal abundance contours appear less dense. This suggests that a large change in quench pressure of CO_2 due to changing K_{zz} will only cause a small change in the quenched CO_2 abundance for such $T(P)$ profiles. However, for planets with colder T_{eq} or colder T_{int}, the $T(P)$ profiles traverse a denser region of equal abundance contours of CO_2. For

these models, a change in quench pressure of CO_2 due to changing K_{zz} will produce a much more pronounced effect on the quenched CO_2 abundance. These models suggest that for T_{eq}=800 and 900 K planets, irrespective of T_{int}, the CO_2 abundance remains sensitive to K_{zz} to varying degrees if K_{zz} is higher than a "transition" value which is typically somewhere between 10^9-10^{10}cm^{2}s^{-1}. Other than the coldest interior case of T_{int}=30 K, the CO_2 abundance doesn't show very strong dependence on T_{int}.

Although for T_{eq}≥800 K, the photospheric CO_2 abundances between thermochemical equilibrium and low K_{zz} values are nearly the same, this breaks down for T_{eq}= 600 K. The CO_2 abundance shows a sharp increase between thermochemical equilibrium models and K_{zz}=10^6cm^{2}s^{-1} for these models. This effect can be understood with the interplay between the 'U' shaped CO_2 equal abundance contours and the $T(P)$ profiles shown in the right panel of Figure 7. Most of the $T(P)$ profiles of planets with T_{eq}≥800 K remain in the $T-P$ space where the CO_2 contours are less dense and nearly vertical. As a result, the equilibrium abundance of CO_2 monotonically and slowly increases with decreasing pressure in these objects. Therefore, there is generally not a large difference between the quenched abundance and chemical equilibrium abundance of CO_2 in these objects. However, the T_{eq}= 600 K model has a complex shape with a nearly horizontal region traversing the densely packed contours, where the chemical equilibrium CO_2 abundance decreases rapidly. If the CO_2 abundance is quenched in this region, the quenched abundance will be significantly higher than expected equilibrium chemistry abundance of CO_2 in the photosphere. Moreover, at T_{eq}=600 K, CO_2 depends almost solely depends on K_{zz}, and not C/O, for T_{int}≤100 K. Some C/O dependence of the photospheric CO_2 abundance sets in for higher T_{int} values. This suggests that near T_{eq}=600 K, the CO_2 abundance can be a good tracer of K_{zz} for planets with cold interiors ($T_{int} \leq 100$ K) but for planets with hotter interiors, it can be quite degenerate between K_{zz} and C/O.

3.1.1.4. H_2O—
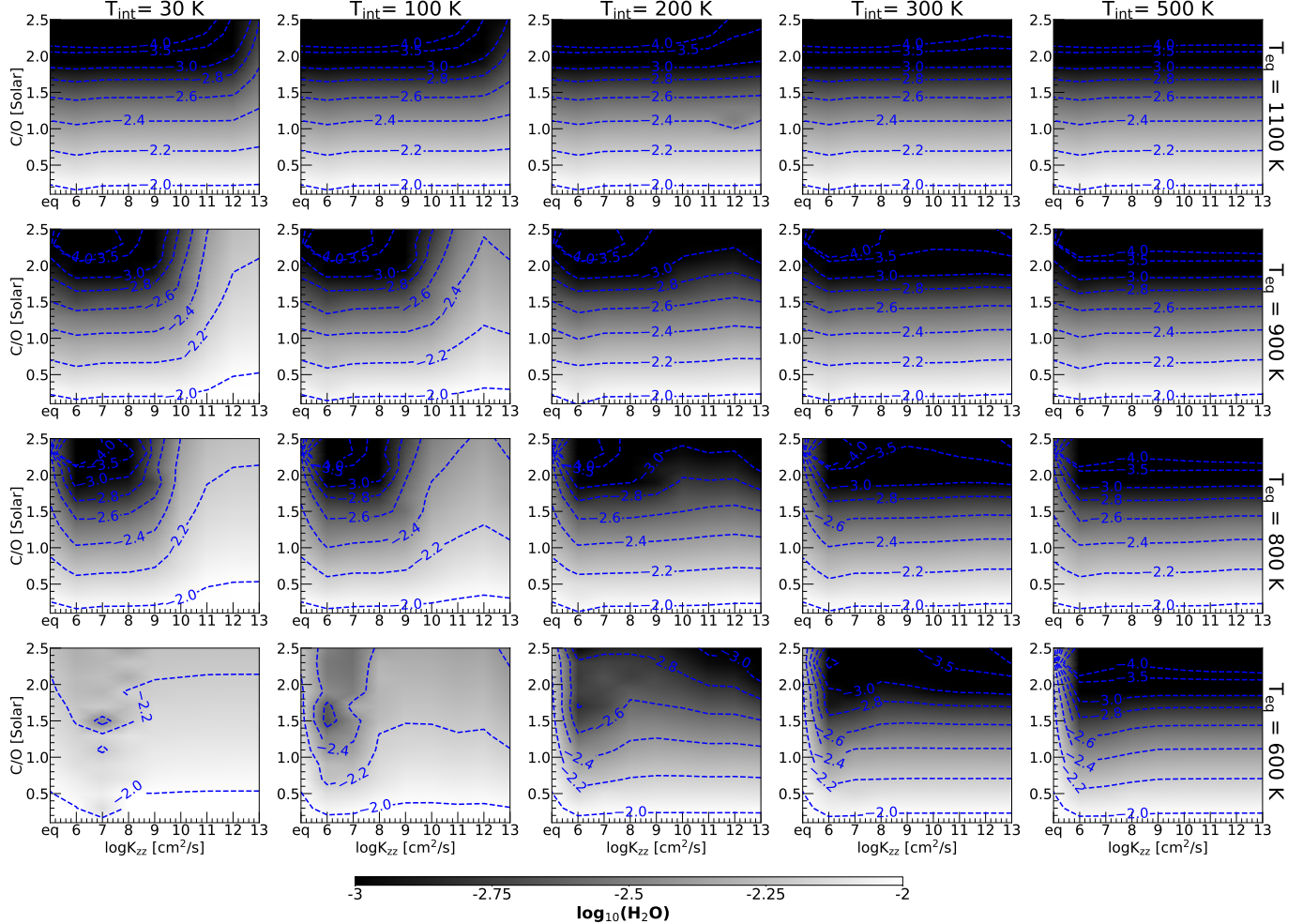
The X_w for H_2O is shown in Figure 8. The range of variation in X_w for H_2O is much lower when compared with other gases shown in Figures 4, 5, and 6. H_2O shows strong sensitivity to C/O when T_{eq}= 1100 K without much dependence on K_{zz}. At T_{eq}= 900 K, when the $T_{int} \geq$ 200 K, this behaviour of H_2O abundance being only dependant on C/O continues. The dependence of H_2O abundance on T_{int} is also extremely

weak in these cases. H_2O starts to show some K_{zz} dependence when $K_{zz} \geq 10^{10}$cm^{2}s^{-1} for $T_{int} \leq 100$ K at T_{eq}= 900 K. This behaviour continues for T_{int}≤ 100 K at T_{eq}= 800 K as well, except the K_{zz} dependence of H_2O abundance sets in a lower value of K_{zz}≥10^9cm^{2}s^{-1}. The H_2O abundance shows an increase with K_{zz} beyond this value which is also accompanied by a sharp decrease in CO and CO_2 abundance seen in this part of the parameter space in Figures 5 and 6, especially at T_{int}= 30 K. The H_2O abundance shows a decrease between thermochemical equilibrium and the K_{zz}=10^6cm^{2}s^{-1} chemical disequilibrium calculations for models with T_{eq}≤800 K. This decrease is particularly strong for C/O≥1.7×solar for T_{eq}= 800 K models. This decrease in H_2O abundance between thermochemical equilibrium and K_{zz}=10^6cm^{2}s^{-1} is also seen for T_{eq}=600 K models. However, the amount of decrease seen in these models increases with increasing T_{int} at this T_{eq}. This highlights that for these hotter T_{int} values ($T_{int} \geq$ 200 K) at $T_{eq} \leq$ 900 K, H_2O can still be a good tracer of C/O but chemical disequilibrium calculations must still be carried out to interpret the C/O from H_2O abundance accurately. The T_{eq}=600 K models shown in the last row of Figure 8 show much less sensitivity to K_{zz} compared to the T_{eq}=900 K and 800 K models. This behavior is similar to the smaller sensitivity shown by CH_4 abundance to K_{zz} in Figure 4 at T_{eq}= 600 K.

3.1.2. Trends in NH_3 and HCN

3.1.2.1. NH_3—

Figure 9 shows the X_w metric for NH_3. NH_3 neither contains C- or O- and therefore is expected to not depend strongly on C/O. All panels of Figure 9 reflect this behavior. At T_{eq}= 1100 K, the photospheres are very NH_3 poor. For T_{eq}= 900 K, the photospheric NH_3 abundance slowly starts to rise, much more for the colder T_{int} models. The vertical equal abundance contours in Figure 9 show that NH_3 is very sensitive to K_{zz} in addition to high sensitivity to T_{int}. Similar to the CH_4 behavior seen in the previous section, NH_3 abundance monotonically increases with K_{zz}. For the coldest interior of T_{int}= 30 K at T_{eq}= 900 K or 800 K, NH_3 abundance increases by 7 orders of magnitude between K_{zz} of 10^6cm^{2}s^{-1} and 10^{13}cm^{2}s^{-1}. The equal abundance curves for NH_3 are known to be nearly parallel to the adiabats for H_2/He gas mixture in the deep atmosphere (Zahnle & Marley 2014; Fortney et al. 2020; Ohno & Fortney 2023a). This means that if NH_3 is quenched in the deep convective atmosphere, its photospheric abundance will not be very sensitive to K_{zz}. NH_3 can become

Figure 8. The weighted abundance of H₂O calculated using Equation 1 has been shown as a heat map as a function of C/O and K_{zz} in each panel. Each row corresponds to a different T_{eq} value from 1100 K to 600 K from top to bottom. Each column correspond to a different T_{int} value between 30 K and 500 K from left to right. Note that the C/O has been shown relative to the assumed solar value of 0.458 in this plot.

more sensitive to K_{zz} if it is quenched in the radiative atmosphere in irradiated planets, where the lapse rate of the $T(P)$ profile is very different than the adiabatic lapse rate. The photodissociation of NH₃ due to the incident UV radiation also depends on K_{zz}. A low K_{zz} in the upper atmosphere causes the NH₃ abundance to be depleted very rapidly with decreasing pressure. The depletion of NH₃ with decreasing pressure is much less if the K_{zz} in the upper atmosphere is high. Both of these effects shape the K_{zz} dependence of the NH₃ abundance shown in Figure 9 in the pressures typically probed by transmission spectroscopy.

At $T_{eq} \leq 900$ K, the NH₃ abundance also declines by several orders of magnitude as T_{int} rises from 30 K to 500 K. Similar to the findings of Ohno & Fortney (2023a), we also find that when $T_{int} \leq 200$ K, the photospheric NH₃ abundance shows a very sharp rise with T_{eq} below T_{eq}=800 K when vertical mixing is slow

($K_{zz} \leq 10^8$cm²s⁻¹). But when vertical mixing is faster, the photospheric NH₃ abundance shows a much more gradual rise with T_{eq}, as was also found by Ohno & Fortney (2023a). Even though detecting NH₃ has proven to be a difficult task so far with *JWST* (Welbanks et al. 2024), its abundance can be of great use for reducing the degeneracies discussed in the previous section arising from just fitting CH₄ abundances and measuring K_{zz} and T_{int}, especially for warm planets.

3.1.2.2. *HCN—*

HCN is a molecule which is quenched due to K_{zz} as well as produced photochemically. Moreover, unlike NH₃, it has C- and therefore should be sensitive to C/O. Figure 10 shows the X_w calculated for HCN. As expected, photospheric HCN shows sensitivity to both C/O and K_{zz}, and also depends on T_{int}. Figure 10 shows

that the disequilibrium chemistry abundance of HCN is much higher than the expected thermochemical equilibrium abundance. The equal abundance contours in the top row for $T_{\rm eq}$= 1100 K run diagonally which shows that same HCN abundance can be very degenerate corresponding to a wide range of C/O ratios and K_{zz} for these hotter planets. At $T_{\rm eq}$= 900 K ,800 K and 600 K, the HCN abundance is mostly sensitive to K_{zz} and not much to C/O if K_{zz} is either low or very high. The HCN abundance is not sensitive to either K_{zz} or C/O for intermediate values of K_{zz}.

3.1.3. *Trends in Sulfur Species*
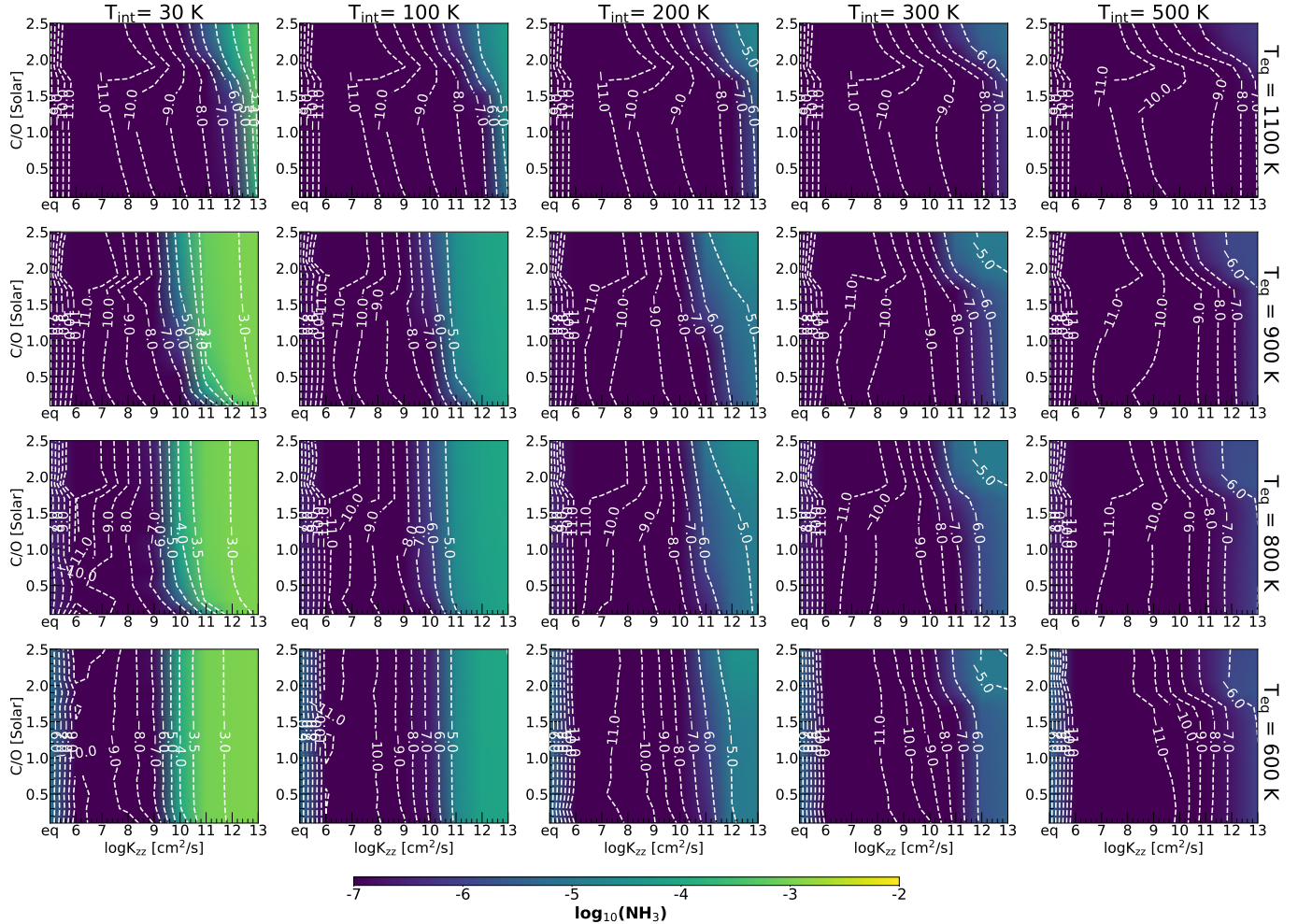
The detection of SO_2 in WASP-39b has garnered great interest in the community due to its photochemical origin. Figure 3 shows how SO_2 is produced in a narrow pressure region in the upper atmosphere. But as transmission spectra of gas giant planets probes this particular pressure region as well, SO_2 features can be easily observed in transmission spectroscopy. Figure 11 shows the X_w for SO_2. At all $T_{\rm eq}$ values except for 600 K, SO_2 shows a sharp increase from thermochemical equilibrium to disequilibrium chemistry cases. For $T_{\rm eq}$= 1100 K, the SO_2 abundance only depends on C/O and shows a small dependence on K_{zz}. For lower C/O values than 1.7×solar, the SO_2 abundance increases very slowly with increasing K_{zz} for $K_{zz} \leq 10^{12} {\rm cm}^2 {\rm s}^{-1}$ followed by a small decrease for higher K_{zz} values. The nearly horizontal equal abundance contours in the top row of Figure 11 shows that the SO_2 abundance is much more sensitive to C/O than K_{zz} at $T_{\rm eq}$=1100 K. The SO_2 abundance shows a gradual decrease with increasing C/O, which is expected as the SO_2 molecule contains two O- atoms and no C- atoms. The decrease of SO_2 with increasing C/O is particularly rapid when C/O≥1.7×solar for these hot planets, similar to CO_2. This is again because of the lack of enough O- atoms to form SO_2 in these very C- rich atmospheres. For these hotter planets, SO_2 also remains independent of $T_{\rm int}$.

For 800 K≤$T_{\rm eq}$≤ 900 K, the SO_2 abundance is overall higher than the $T_{\rm eq}$=1100 K. The SO_2 abundance starts to show strong dependence on K_{zz} at this $T_{\rm eq}$, especially for high K_{zz} values. This dependence particularly sets in when the K_{zz} is higher than another "transition" value of K_{zz}. Below this transition value, the SO_2 shows little to no dependence on K_{zz}, but once the K_{zz} is higher than this value, SO_2 abundance shows a rapid decline with increasing K_{zz}. Figure 11 second row shows that this transition K_{zz} depends on both C/O and $T_{\rm int}$. For example, at $T_{\rm eq}$=900 K, this "transition" K_{zz} can be identified to be around $10^{10} {\rm cm}^2 {\rm s}^{-1}$ when $T_{\rm int}$=30 K. But this "transition" K_{zz} is higher at K_{zz}=$10^{12} {\rm cm}^2 {\rm s}^{-1}$

for $T_{\rm int}$=300 K. Qualitatively similar behavior is also exhibited in the $T_{\rm eq}$=800 K models. SO_2 shows another interesting behavior for $T_{\rm int}$≤200 K where the SO_2 shows a rapid increase with K_{zz} when C/O≥1.5×solar and K_{zz} is between 10^{10}-$10^{12} {\rm cm}^2 {\rm s}^{-1}$. The SO_2 abundance then declines rapidly when K_{zz} is increased further, which is the effect discussed just above. This rapid increase of SO_2 with increasing K_{zz} before showing a decline occurs for C/O≥1.0×solar in the $T_{\rm eq}$=800 K models shown in the third row of Figure 11.

The SO_2 abundance in the photosphere of the $T_{\rm eq}$= 600 K models declines by several orders of magnitude than the $T_{\rm eq}$=800 K models. This decline is close to 6-7 orders of magnitude for values of K_{zz} lower or higher than a narrow range of K_{zz} between 10^{10}≤K_{zz}≤$10^{12} {\rm cm}^2 {\rm s}^{-1}$, when $T_{\rm int}$=30 K. For this narrow range of K_{zz} values, the decline is only about by ∼ 1-2 order of magnitudes. For higher $T_{\rm int}$ values, this narrow range of K_{zz} where SO_2 is still relatively more abundant than the rest of the parameter space, still exists. However, this region of the parameter space shrinks progressively along both the C/O and K_{zz} direction with increasing $T_{\rm int}$. This shows that below $T_{\rm eq}$≤600 K, it is very difficult to photochemically produce a detectable amount of SO_2, unless the atmospheric metallicity is much higher than 10× solar. The depletion of SO_2 at cool $T_{\rm eq}$ is consistent with previous work and is attributed to the depletion of OH radicals that are needed to form SO_2 (Tsai et al. 2023b)

SO_2 is not the only important S- bearing molecule in these atmospheres. Figure 12, upper set of panels, shows the volume mixing ratio of various S-bearing molecules as a function of $T_{\rm eq}$ and C/O at a fixed K_{zz}=$10^9 {\rm cm}^2 {\rm s}^{-1}$ and $T_{\rm int}$=200 K. The volume mixing ratios at 1 mbar are shown. The right-most panel in the middle row of Figure 12 shows that the SO_2 abundance in the photosphere declines sharply when $T_{\rm eq}$≤ 600 K or C/O ≥2×solar. The same behaviour is also shown by SO. Figure 12 also shows that SO is an almost equally abundant product of photochemistry expected in the same part of the parameter space as SO_2. Comparing the SO and SO_2 panels in Figure 12 also shows that SO declines slower with increasing $T_{\rm eq}$ compared to SO_2. As both SO and SO_2 decline at high C/O≥2×solar, most of the S- in the photosphere goes into CS instead. With the decline of SO and SO_2 at $T_{\rm eq}$≤ 600 K, CS and CS_2 also start to carry a large fraction of the S- inventory. This is particularly interesting in the context of the recent tentative detection of CS_2 in the atmosphere of TOI-270 d with *JWST* (Benneke et al. 2024; Holmberg & Madhusudhan 2024), which has a $T_{\rm eq}$ between 350-380 K but is inferred to be much more metal rich than 10×solar.

Figure 9. The weighted abundance of NH$_3$ calculated using Equation 1 has been shown as a heat map as a function of C/O and K_{zz} in each panel. Each row corresponds to a different T_{eq} value from 1100 K to 600 K from top to bottom. Each column correspond to a different T_{int} value between 30 K and 500 K from left to right. Note that the C/O has been shown relative to the assumed solar value of 0.458 in this plot.
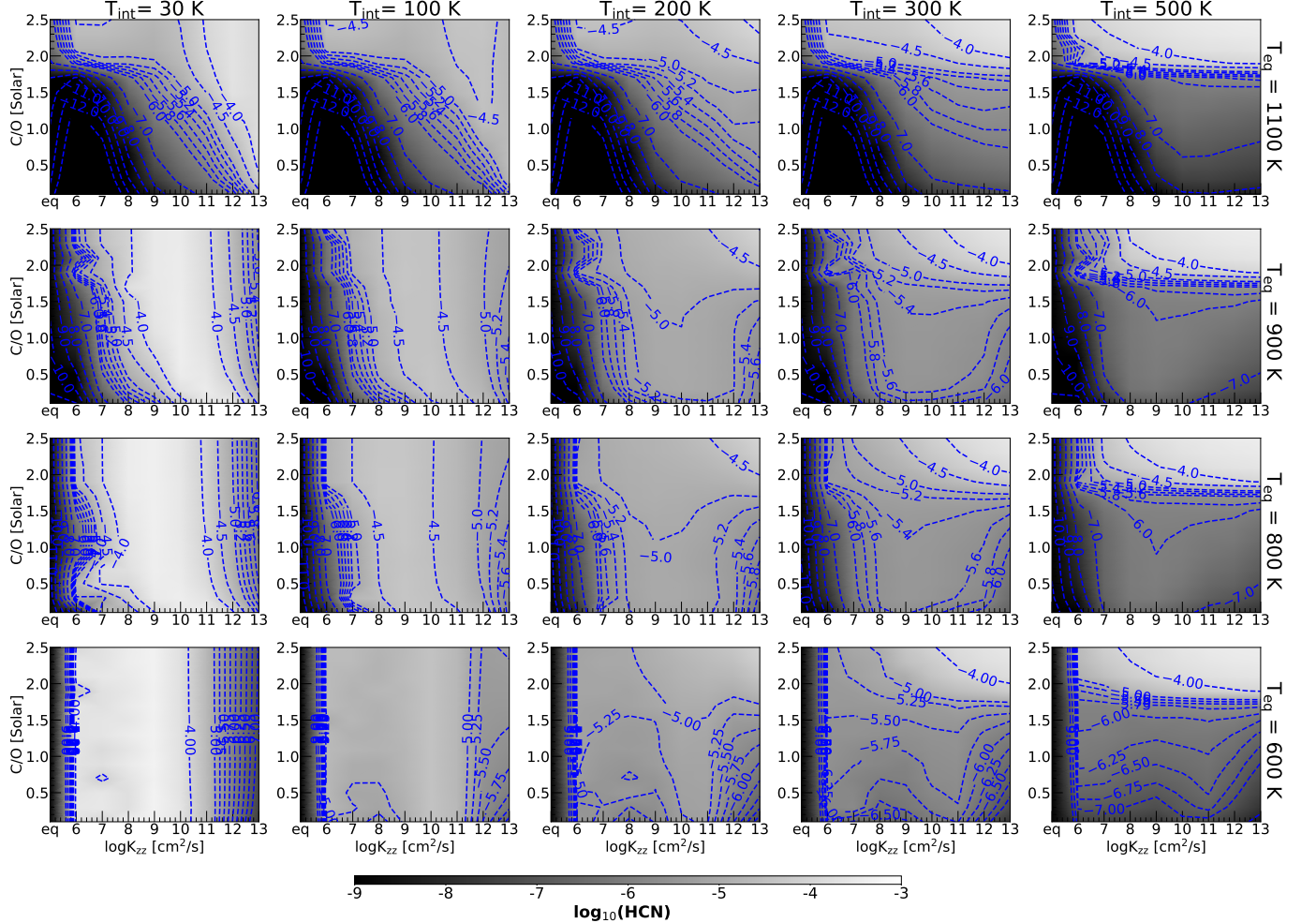
Among the other S$_x$ kind of molecules S$_2$ seems the most abundant. Molecules like S$_3$ and S$_4$ are at least 4-6 orders of magnitude less abundant than S$_2$. Interestingly, the abundance of S$_8$ is almost negligible for $T_{eq} \geq 600$ K, but Figure 12 shows that S$_8$ and OCS shows a very sharp increase in abundance for $T_{eq} \leq 400$ K. Figure 12 shows that among the H$_x$S gases, H$_2$S is more abundant than HS at 1 mbar, especially for $T_{eq} \geq 1200$ K. We note that S- polymerization kinetics is still not very well understood (e.g., Zahnle et al. 2016) and there is also significant uncertainty in the OCS recombination rates (e.g., Ranjan et al. 2020; Tsai et al. 2021).

Figure 12, lower set of panels, shows the abundance of the same gases but at 0.1 bar instead. It is clear that almost all of the S- is present in the form of H$_2$S with a minor amount in the form of HS in the deeper atmospheres. The abundance of gases like SO, SO$_2$, and CS, which are the dominant S- bearers near the pressures

probed by transmission spectroscopy, are much lower at these deeper pressures. This is expected as these gasses are photochemically enhanced at the smaller pressures. Interestingly, even though CS is more abundant than CS$_2$ in the upper atmosphere probed by transmission spectroscopy, CS$_2$ appears to be more abundant molecule in the deeper atmosphere probed by emission spectroscopy. The most abundant S- carrying gas after H$_2$S in the deeper atmosphere is HS for $T_{eq} \geq 1000$ K. But below $T_{eq} \leq 1000$ K, CS$_2$ becomes the second-most abundant S- carrying gas after H$_2$S in the deep atmosphere. For T_{eq} lower than 500 K, OCS replaces CS$_2$ as the second most S- carrying gas after H$_2$S.

3.2. *Exploring how abundances depend on K_{zz}, C/O, and T_{int} across different metallicities*

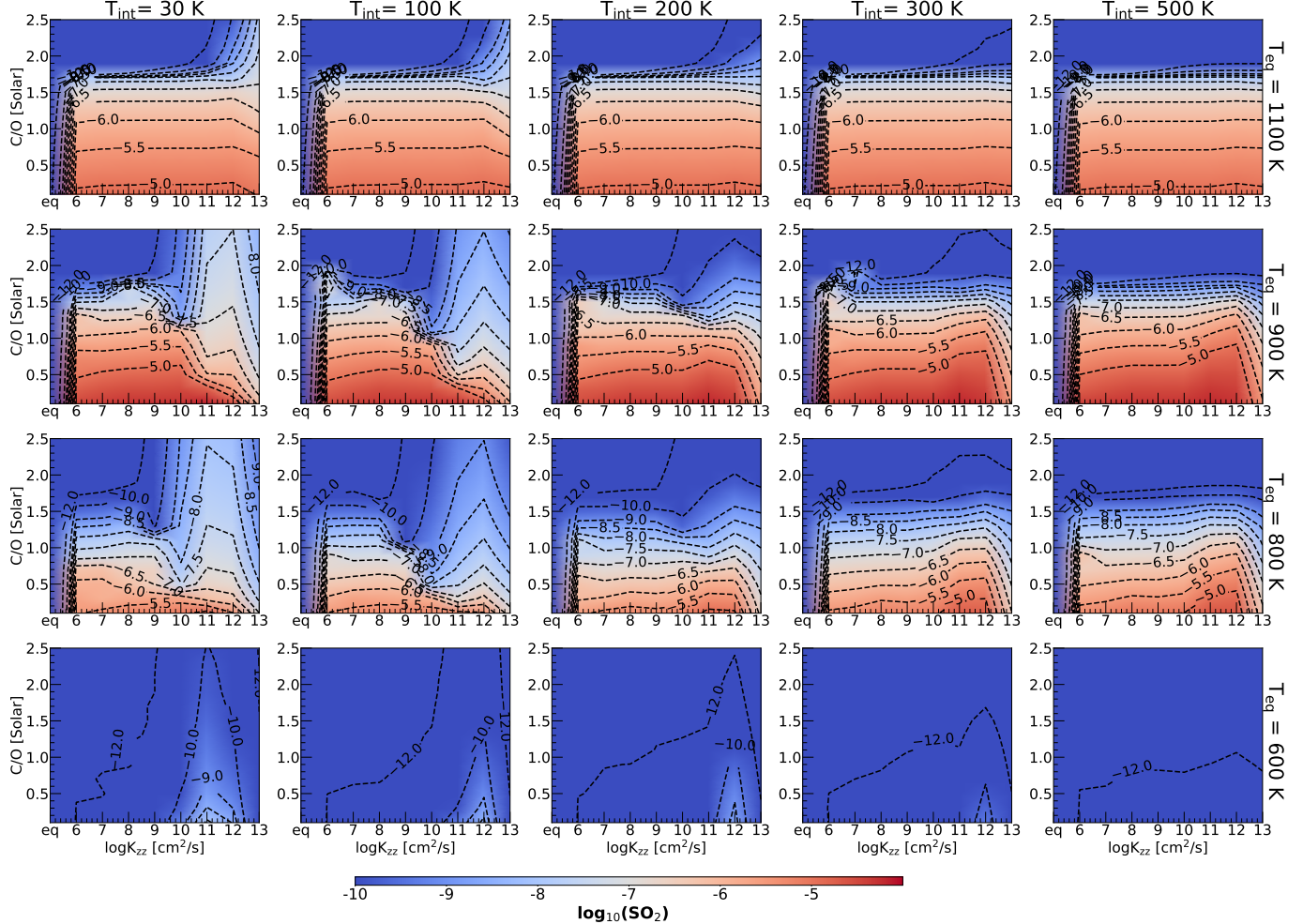Metallicity scales the abundance of C-, O-, N-, and S- relative to H in our modeling framework. §3.1 showed
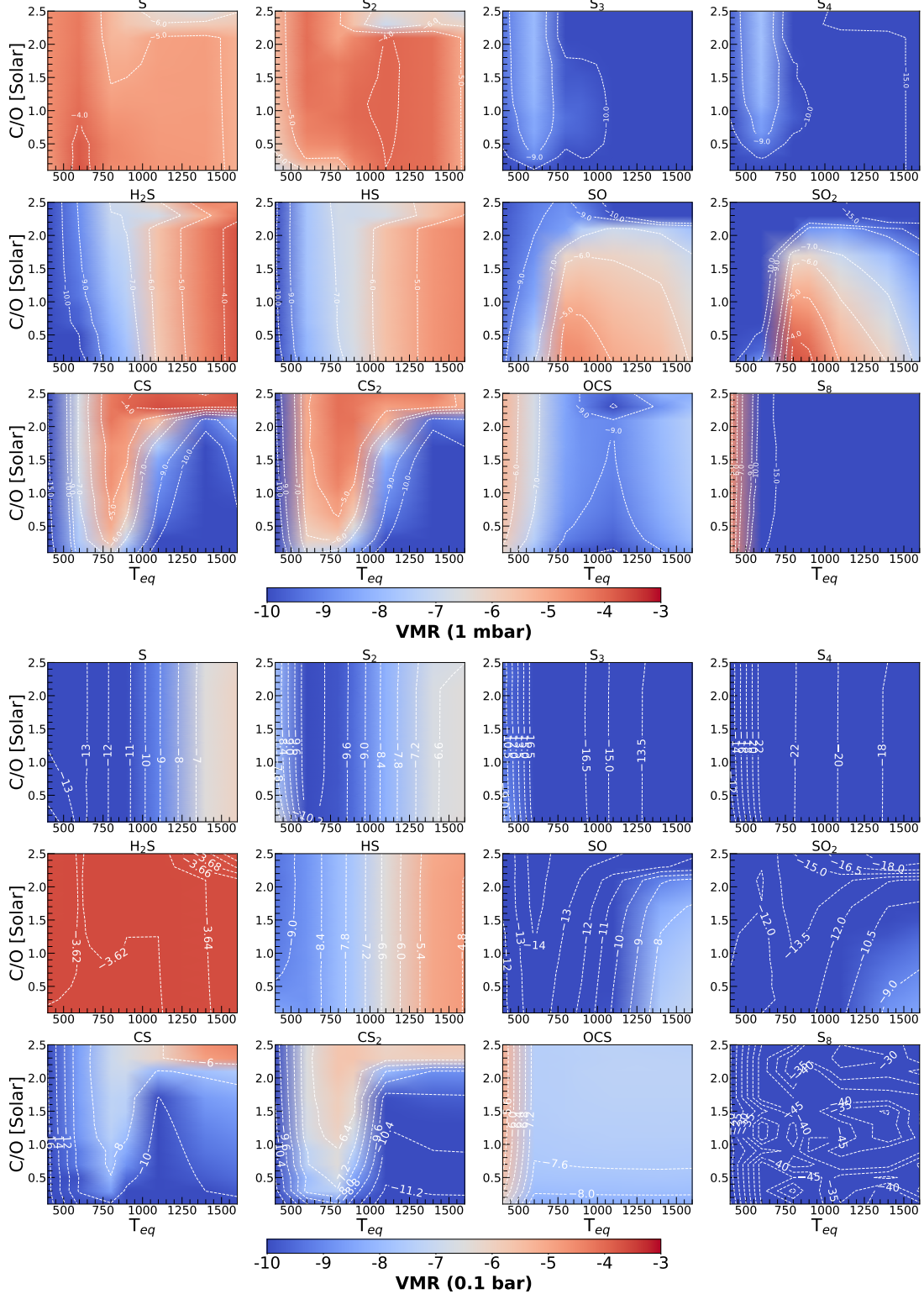
Figure 10. The weighted abundance of HCN calculated using Equation 1 has been shown as a heat map as a function of C/O and K_{zz} in each panel. Each row corresponds to a different T_{eq} value from 1100 K to 600 K from top to bottom. Each column correspond to a different T_{int} value between 30 K and 500 K from left to right. Note that the C/O has been shown relative to the assumed solar value of 0.458 in this plot.

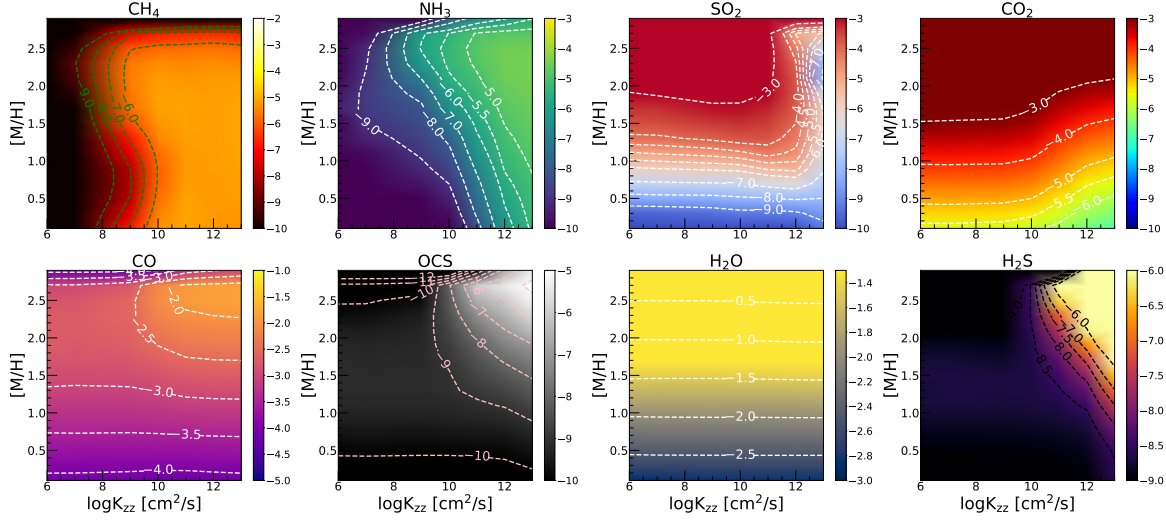that C/O can be degenerate with K_{zz} and T_{int} for most gases at small or big parts of the parameter space. Here, we explore how atmospheric metallicity influences photospheric abundance of gases across the same parameter space. We use models for a planet with T_{eq}= 800 K for this purpose with a T_{int}=200 K.

Figure 13 shows X_w for CH_4, NH_3, SO_2, CO_2, CO, OCS, H_2O, and H_2S as a function of [M/H] and K_{zz} in the different panels. These models are shown for a very O- rich atmosphere with C/O=0.1× solar whereas Figure 14 shows the same quantities but for C/O=1×solar. The CH_4 panel of Figure 13 shows that at C/O=0.1×solar, increasing K_{zz} leads to increase in CH_4 when $K_{zz} \leq 10^{10} cm^2 s^{-1}$. This holds true at C/O=1×solar in Figure 14 too. The overall CH_4 abundances are much lower in the C/O=0.1×solar than the C/O=1×solar, as expected. The equal abundance contours for CH_4 in the C/O=0.1×solar case (Figure 13)

are nearly vertical which suggests that the photospheric CH_4 abundance varies a lot with changing K_{zz}, but not much with [M/H]. This holds true at C/O=1×solar as well (Figure 14) but only for [M/H]≤+0.5 and [M/H]≥+1.0. For intermediate metallicities, Figure 14 shows that CH_4 abundance can depend both on [M/H] and K_{zz}, increasing as both of these parameters are increased. For metallicities higher than [M/H]=+2.5, CH_4 abundance starts to decrease rapidly with increasing metallicity for the very O- rich case shown in Figure 13. This behavior is also present but to a smaller extent in the solar C/O models in Figure 14. Note that our models do not account for graphite saturation (Moses et al. 2013b), which could draw down the CH_4 concentration and impact other carbon-bearing species in Figure 14 for high metallicities ([M/H] > 2).

NH_3 abundance in Figures 13 and 14 also show increase with increasing K_{zz}. The equal abundance con-

Figure 11. The weighted abundance of SO_2 calculated using Equation 1 has been shown as a heat map as a function of C/O and K_{zz} in each panel. Each row corresponds to a different T_{eq} value from 1100 K to 600 K from top to bottom. Each column correspond to a different T_{int} value between 30 K and 500 K from left to right. Note that the C/O has been shown relative to the assumed solar value of 0.458 in this plot.

tours of NH_3 are along the diagonal direction, which suggests that the NH_3 abundance shows a dependence on both [M/H] and K_{zz}. For a given K_{zz}, higher [M/H] values produces more photospheric NH_3 than lower [M/H] values, except for [M/H]$\geq$+2.5 models with C/O=0.1×solar. Both SO_2 and CO_2 show much stronger [M/H] dependence than K_{zz} dependence, unlike CH_4 and NH_3. This is expected as both SO_2 and CO_2 require one C- or S- and two O- atoms per molecule. It is interesting that for very O- rich atmospheres (Figure 13), the rate of increase of SO_2 with increasing [M/H] slows down considerably for high [M/H] values. This behavior also happens in the C/O=1×solar atmospheres in Figure 14, but not to the extent present in Figure 13. The metallicity dependence of SO_2 only disappears when the K_{zz} is higher than a threshold value. Beyond this value, the SO_2 abundance shows a sharp decline with increasing K_{zz} without much [M/H] depen-

dence. In Figure 13, this threshold appears to be close to $10^{12} cm^2 s^{-1}$, whereas in Figure 14, the threshold is near $10^{11} cm^2 s^{-1}$. The CO_2 abundance also shows some K_{zz} dependence for high K_{zz} values, but not to the extent of the sharp change shown by SO_2. For a given [M/H], the CO_2 abundance shows a slight increase with increasing K_{zz} when the K_{zz} is higher than $10^{11} cm^2 s^{-1}$. For lower K_{zz} values, the CO_2 abundance solely depends on [M/H] (for a fixed C/O).
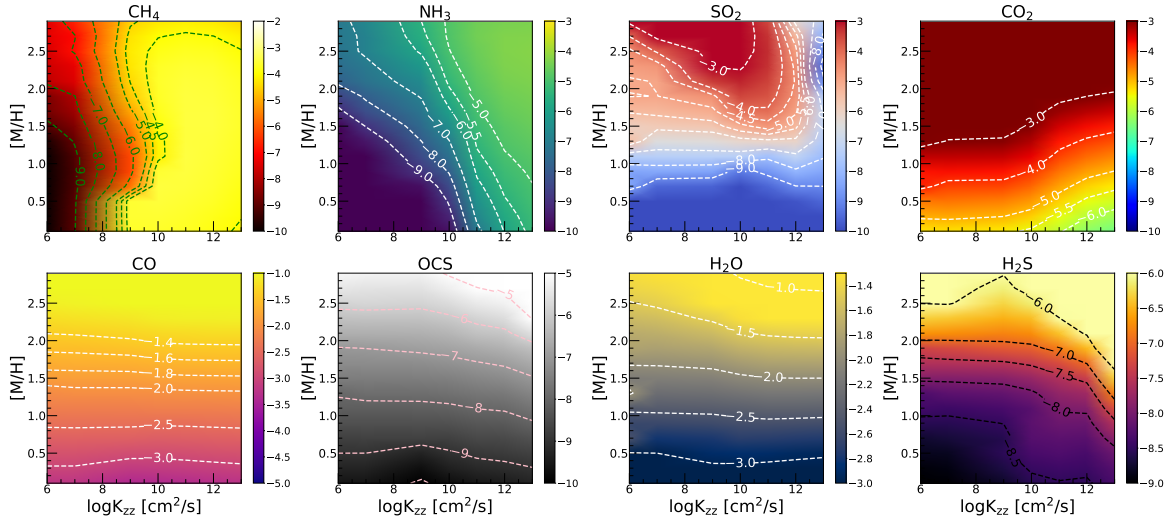
Like CO_2, CO shows little to no dependence on K_{zz} and strong dependence on metallicity. The main reason behind this is the relatively higher T_{int}=200 K of these models. Interestingly, CO abundances in Figure 13 are generally lower than the CO abundances in Figure 14. This is the case as CO contains equal numbers of C- and O- atoms, so its abundance is diminished in a very O- rich and C- poor atmosphere. CO also shows some minor dependance on K_{zz} in the very O- rich atmospheres

Figure 12. The top set of panels show the abundance of various Sulfur species at 1 mbar as a heat map as a function of C/O and $T_{\rm eq}$ in each panel. Each panel corresponds to a different S- bearing gas. All models shown here have $T_{\rm int}$=200 K and K_{zz}=10^{9}cm^{2}s^{-1}. The lower panels show the abundance of the same species but at 0.1 bar instead. This is to show the abundance of S- bearing gases both at pressures probed by transmission and emission spectroscopy, respetively.

Figure 13. Each panel shows how X_w for a different gas varies with [M/H] and K_{zz} as a heat map. All the models shown here have T_{eq}= 800 K, T_{int}= 200 K, and C/O= 0.1×solar.

Figure 14. Each panel shows how X_w for a different gas varies with [M/H] and K_{zz} as a heat map. All the models shown here have T_{eq}= 800 K, T_{int}= 200 K, and C/O= 1×solar.

(Figure 13) when [M/H]$\geq$+2.0. OCS also shows a similar behavior as CO, where its abundance is diminished in the very O- rich/C- poor atmospheres compared to solar C/O atmospheres. The OCS abundance seems to primarily depend on atmospheric [M/H] unless K_{zz} is high. For high K_{zz}, the OCS abundance starts to increase with increasing K_{zz} and this increase is particularly rapid for significantly metal-enriched atmospheres. This behavior is also mimicked by H_2S, where its much less abundant in the O- rich/C- poor atmosphere than the solar C/O atmosphere. The photospheric abundance of H_2S also shows a rapid increase with increasing K_{zz} beyond a threshold value, particularly in high [M/H] atmospheres. Figures 13 and 14 show that H_2O abundance in the photosphere only depends on [M/H], with almost no K_{zz} dependence at all.

3.3. Chemical Transitions with T_{eq}

Fortney et al. (2020) and Ohno & Fortney (2023a) presented how fundamental chemical transitions in the atmosphere, like from being CO rich to CH_4 rich, can depend on both T_{int} and K_{zz} in addition to T_{eq}. Recently, Bell et al. (2023) reported the discovery of CH_4 in the atmosphere of WASP-80b detected in both transmission and emission spectroscopy of the planet with *JWST*. There have been efforts to measure the T_{eq} value below which CH_4 first starts to appear in observations of exoplanetary atmospheres. But this can be a complex function of T_{int}, K_{zz}, C/O, and [M/H] (e.g., Fortney et al. 2020).

Figure 15 presents these transitions/behavior from our photochemical 1D chemical kinetics grid for three pairs of molecules – CO-CH_4, N_2-NH_3, and H_2S-SO_2-S at [M/H]=+1.0. The top row panels in Figure 15 shows how CO and CH_4 photospheric abundance change with decreasing T_{eq} for T_{int}=30 K, 100 K, 200 K, and 500 K from left to right, respectively. Each panel in Figure 15 shows three colored solid lines denoting the CH_4 abundance for three different K_{zz} values, whereas the dotted lines indicate the CO abundance in each case. It is clear that the upper atmosphere probed by transmission spectroscopy can only have $CH_4\geq$CO in planets with cold interiors $T_{int} \sim$ 100 K or lower. For hotter interiors, CO always remains the majority C- carrier molecule with higher abundance than CH_4. This transition was seen to be happening at or below T_{int}=150 K too by Fortney et al. (2020), even though they used quench-time approximation for approximating the effect of K_{zz} on chemistry and also did not treat photochemistry in their models. We note that this threshold of T_{int}=150 K was found at 3×solar metallicity in Fortney et al. (2020) instead of the 10×solar metallicity assumed
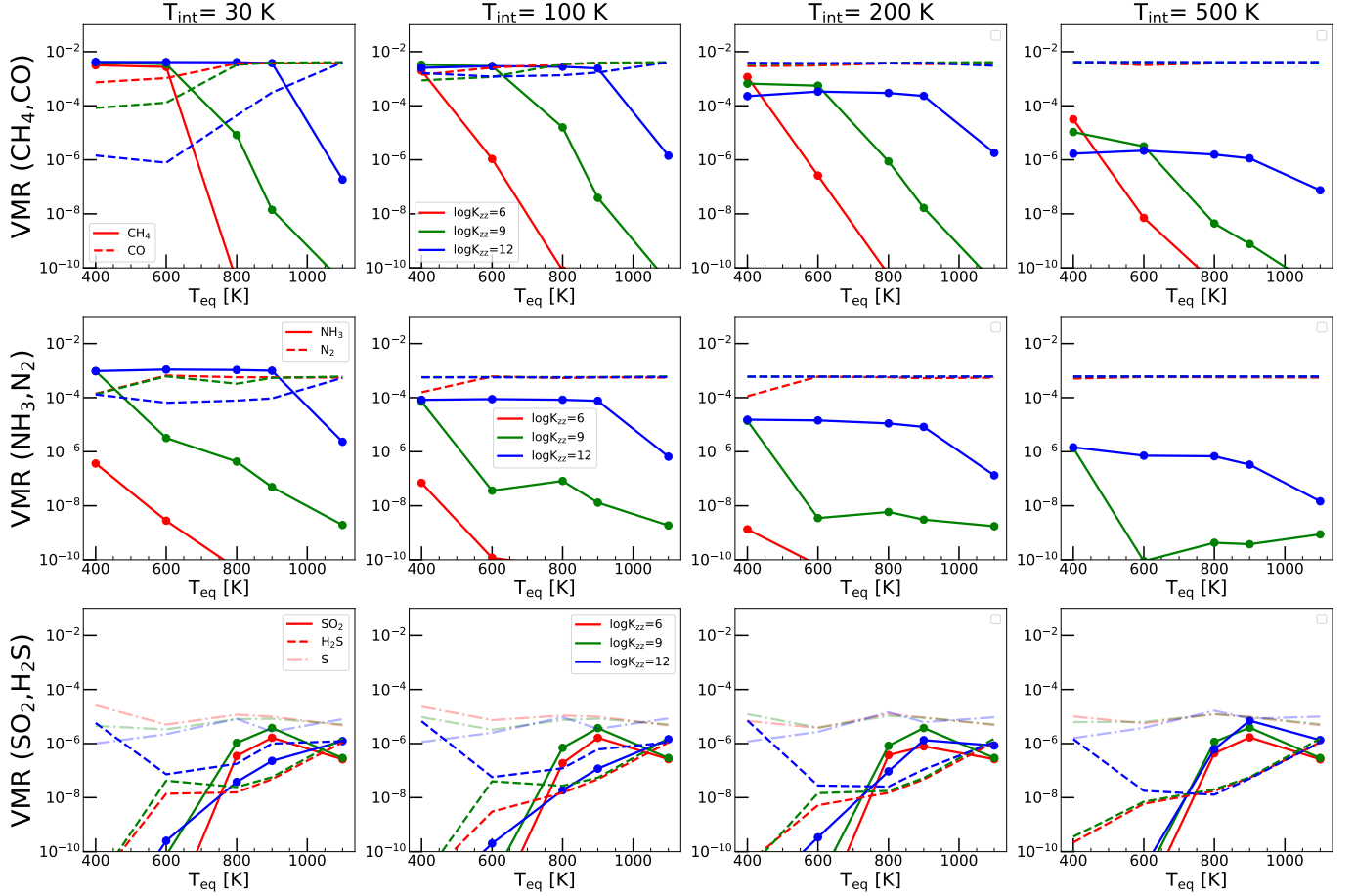
in our analysis. Figure 15 also shows that the T_{eq} value where this transition from CO rich to CH_4 rich occurs is a very strong function of K_{zz}. When K_{zz}=10^{12}cm^{2}s^{-1}, this transition happens near T_{eq}= 1000 K for atmospheres with $T_{int}\leq$100 K. But, for K_{zz}=10^9cm^{2}s^{-1} or K_{zz}=10^6cm^{2}s^{-1} , atmospheres can remain CO rich for T_{eq} above 600 K. When T_{int}= 500 K, shown in the right most column of Figure 15, the CH_4 abundance is still an order of magnitude lower than CO even for T_{eq}= 400 K.

The second row of Figure 15 shows the same quantities as the first row but for NH_3 (solid lines) and N_2 (dashed lines) instead. Figure 15 second row shows that the NH_3 can only become the major N- carrier if the T_{int} is 30 K. Even for such cold interior, the mixing needs to be high to make NH_3 carry most of the N- atoms in the photosphere. For example, the NH_3 in the photosphere still remains almost two orders of magnitude lower than that of N_2 abundance if K_{zz}=10^6cm^{2}s^{-1}, even if T_{int}=30 K. This result is also consistent with the findings of both Fortney et al. (2020) and Ohno & Fortney (2023a). Ohno & Fortney (2023b) found that NH_3 can become the dominant carrier of N- atoms in giant planets only in a small parameter space where the planet has a low mass and is very old, such that the interior is sufficiently cool and vertical mixing can dredge the NH_3 up to the upper atmosphere.

The last row of Figure 15 shows the behavior of the abundance of three major S- carrying species – H_2S (dashed lines), SO_2 (solid lines), and S (faded dash-dotted lines) as a function of T_{eq}. The notable thing in Figure 15 is that neither SO_2 or H_2S carries majority of the S- inventory of the atmosphere, not atleast at [M/H]=+1.0. Instead, neutral S- atoms form a much more substantial fraction of the total S- inventory in the upper atmosphere than SO_2. These are shown with the faded dash dotted lines in all the panels and the same phenomenon is also shown in Figure 12. This was seen in previous work (e.g., Tsai et al. 2023c,b) as well. Figure 15 also shows how the SO_2 abundance peaks near T_{eq}= 900 K but gradually decreases when the T_{eq} increases further. But the decrease of SO_2 with decreasing T_{eq} is much more rapid as was also seen in Figure 12.

3.4. Sensitivity of Transmission Spectrum to K_{zz} and T_{int}

While we have presented our results on the detailed chemical abundances at different parts of the parameter space till now, here we present how this chemistry affects the observable – the transmission spectra. The top panel of Figure 16 shows the transmission spectra computed from the T_{eq}= 800 K, T_{int}= 200 K, C/O=1.1×solar, and
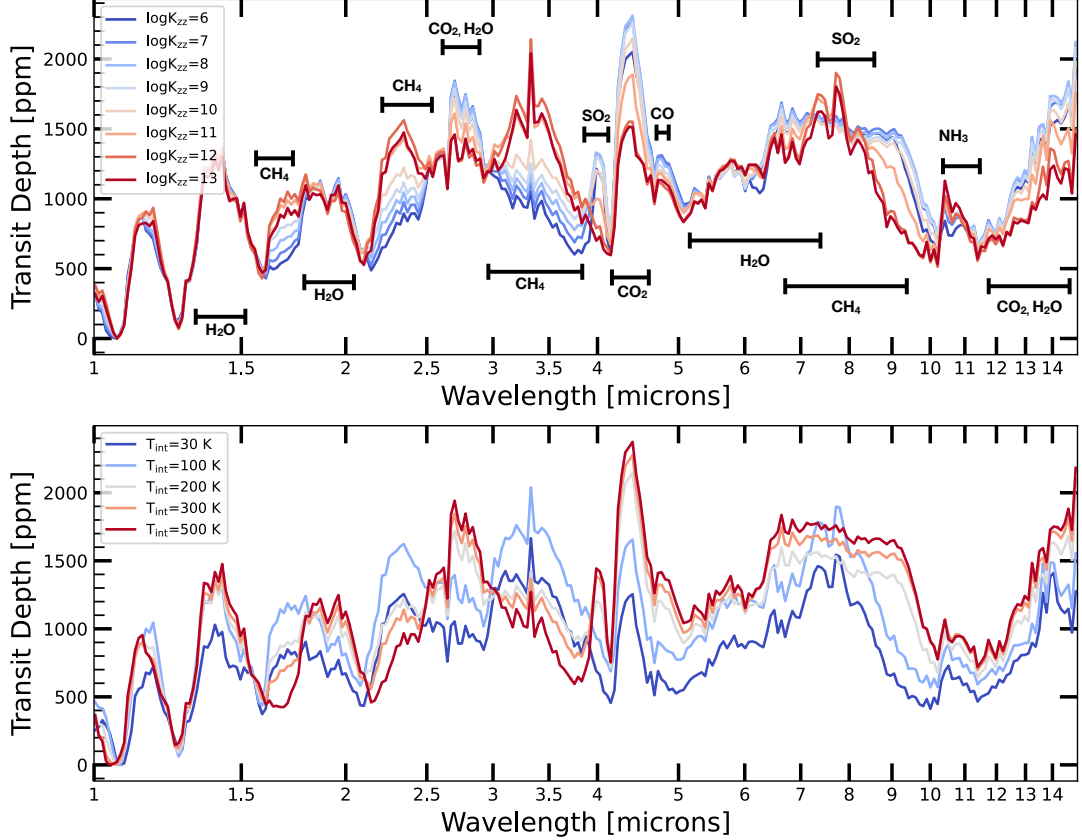
Figure 15. The variation of photospheric abundance of key atmospheric gases as a function of T_{eq} is shown here. Each column shows the variation for a different value of T_{int}. The top row shows the evolution of CH_4 and CO abundance with T_{eq}. The middle and last row shows the same for N_2-NH_3, and H_2S-SO_2-S, respectively. In each panel, the three colored lines shows the abundances for a three different values of K_{zz}. The C/O has been fixed to be 1×solar in these models.

[M/H]=+1.0 models for a range of different K_{zz} values. It is clear that certain parts of the transmission spectra are quite sensitive to K_{zz} while others are not as much. For example, the CH_4 band between 3-3.5 μm, and the SO_2 band at 4μm and 7-10 μm are quite sensitive to K_{zz}. On the other hand, the H_2O bands between 1-1.5 μm does not show as much sensitivity to K_{zz}.

The lower panel in Figure 16 shows the sensitivity of the transmission spectrum to T_{int} with a fixed $K_{zz}=10^{10}$cm^{2}s^{-1}. The T_{int} has been varied from 30 K to 500 K. It is clear that the spectra is very CH_4 dominated for cold interiors with T_{int}=30 K and 100 K. As the T_{int} increases further, the effect of CH_4 on the spectra slowly decreases. Looking at Figure 16, it is not exactly clear at how the transmission spectrum responds to changing K_{zz} and T_{int} in different parts of the vast parameter space explored in this work. Therefore, we present those trends in the upcoming section by computing the differential of the transmission spectra at each wavelength bin with changing K_{zz} and T_{int}.

3.4.1. Dependence of spectra on K_{zz}

To highlight the wavelength ranges where the transmission spectra changes the most when a parameter like K_{zz} is changed, we first renormalise all the transmission spectra across our grid such that the minimum transit depth of each transmission spectra is zero. Then, we calculate the change in the renormalised transit depth within each wavelength bin from one grid point to the next grid point. For example, to highlight which part of the transmission spectra changes the most with a change in K_{zz} near T_{int}=30 K, T_{eq}=800 K, C/O=0.1×solar, [M/H]=+1.0, and $K_{zz}=10^8$cm^{2}s^{-1}, we calculate $dF(\lambda)/dlogK_{zz}=$ $(F(\lambda,K_{zz}=10^8)$-$F(\lambda,K_{zz}=10^7))/(log_{10}(10^8)$-$log_{10}(10^7))$, where F denotes the renormalized transmission spectra at the above mentioned grid point parameters. We plot this quantity $dF(\lambda)/dlogK_{zz}$ in the top left panel of Figure 17 as a function of K_{zz} with a color map. Each row in Figure 17 shows the same quantity for a different T_{int} value while each column corresponds to a different
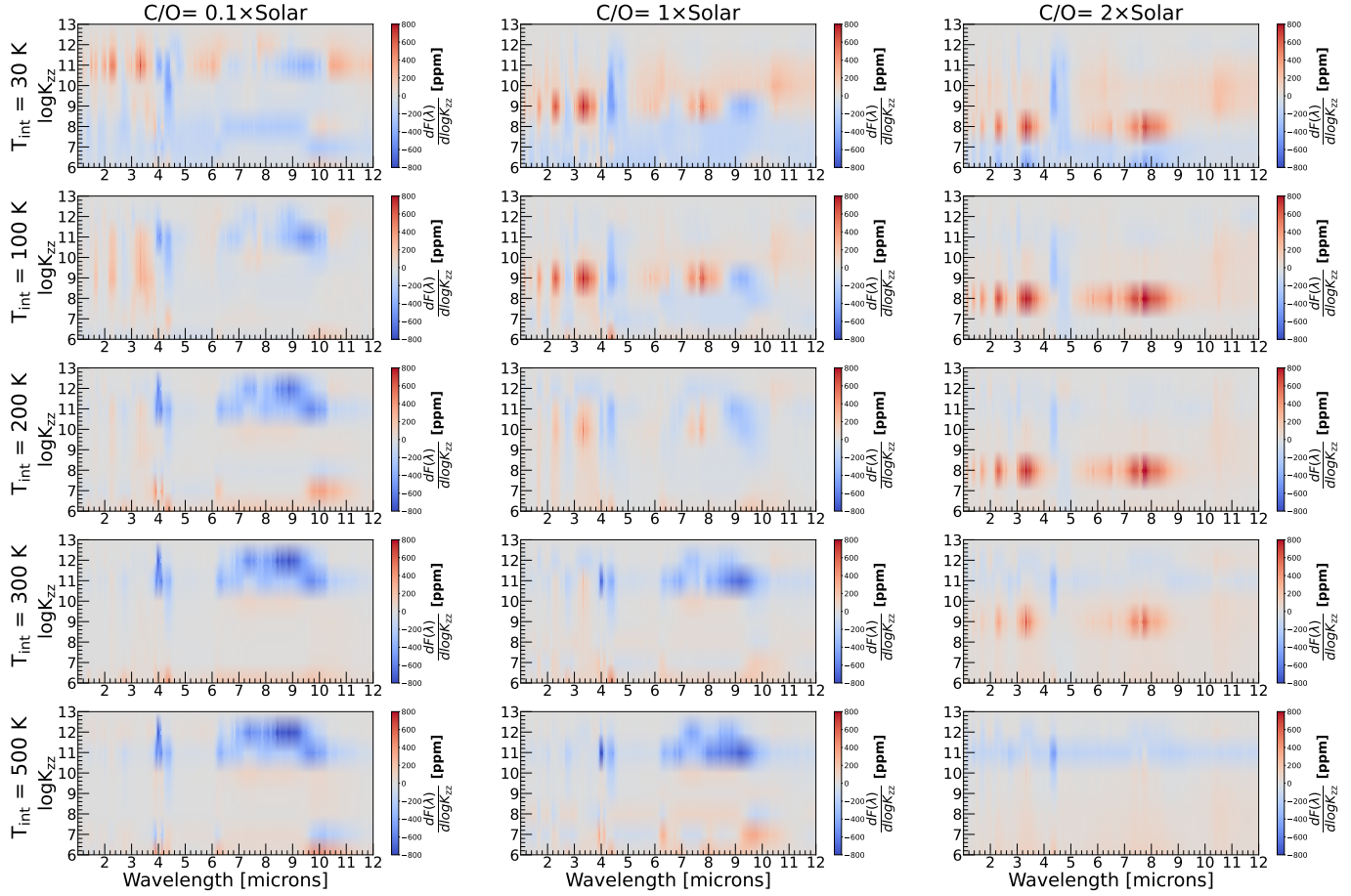
Figure 16. The top panel shows the variation of transmission spectra with changing K_{zz} while the bottom panel shows the variation of the transmission spectra of the planet with changing T_{int}. The models shown here are for T_{eq}=800 K, [M/H]=+1.0, and C/O=1×solar. The T_{int} has been fixed at 200 K for the top panel while the K_{zz} has been fixed at 10^{10}cm^{2}s^{-1} in the bottom panel. Note that the transmission spectra have been renormalized in such a manner that the minimum transit depth of each model is set at zero.

C/O for a fixed T_{eq}= 800 K. The $dF(\lambda)/dlogK_{zz}$ quantity shows how the transit depth in a given wavelength change in parts-per-million (ppm) in a particular part of the parameter space if K_{zz} is changed by one order of magnitude there. We note that the $dF(\lambda)/dlogK_{zz}$ quantity is sparsely sampled in the K_{zz} direction, and as a result the trends shown in Figure 17 and 18 may appear smoother than expected. This quantity helps us to identify which are the best wavelength range or molecular features to constrain K_{zz} in a particular part of the parameter space.

Figure 17 top row shows that if the interior of the planet has T_{int}=30 K, the CH$_4$ and CO$_2$ bands near 3.3 μm and 4.2-4.3μm, respectively, show the most sensitivity to changing K_{zz}. However, it is clear that the maximum change on the spectra due to changing K_{zz} appears at different K_{zz} values depending on the C/O. For example, in the C/O=0.1×solar panel on the top left, the maximum change in the CH$_4$ feature appears at high K_{zz} values near 10^{10}cm^{2}s^{-1}. This region of maximum sensitivity of the CH$_4$ band shifts to lower

K_{zz}=10^8cm^{2}s^{-1} value when the C/O is 1×solar and to even lower K_{zz}= 10^7cm^{2}s^{-1} when the C/O is 2×solar in the top row. However, Figure 17 top row shows that the CO$_2$ band near 4.2-4.3 μm remains quite sensitive to K_{zz} for almost all K_{zz} values in this cold interior scenario.

As the T_{int} is increased from 30 K to 500 K (moving from the top towards the bottom row in Figure 17), the sensitivity of the CH$_4$ bands to K_{zz} slowly diminishes while the SO$_2$ bands near 4μm and 7-9 μm become increasingly sensitive to changing K_{zz}. This happens only in the C/O = 0.1× and 1×solar columns. The sensitivity of the SO$_2$ bands set in particularly for high values of K_{zz} above 10^{10}cm^{2}s^{-1}. The rest of the transmission spectra still remains sensitive to K_{zz} but to a smaller degree. When C/O=2×solar, the CH$_4$ bands remain the most sensitive parts of the transmission spectra till T_{int}≤300 K. The sensitivity of the 4.2-4.3 μm CO$_2$ slowly diminishes in this case as the interior warms up from a T_{int} of 30 K to 500 K.

Figure 17. Sensitivity of the transmission spectra to changing K_{zz} is shown here as a function of K_{zz} and wavelength. Each column corresponds to a different C/O value whereas each row shows models for different T_{int} values. All models shown here have T_{eq}=800 K. A brighter red or a brighter blue color indicates that the transmission spectra is very sensitive to changing K_{zz} at that K_{zz} and wavelength value.
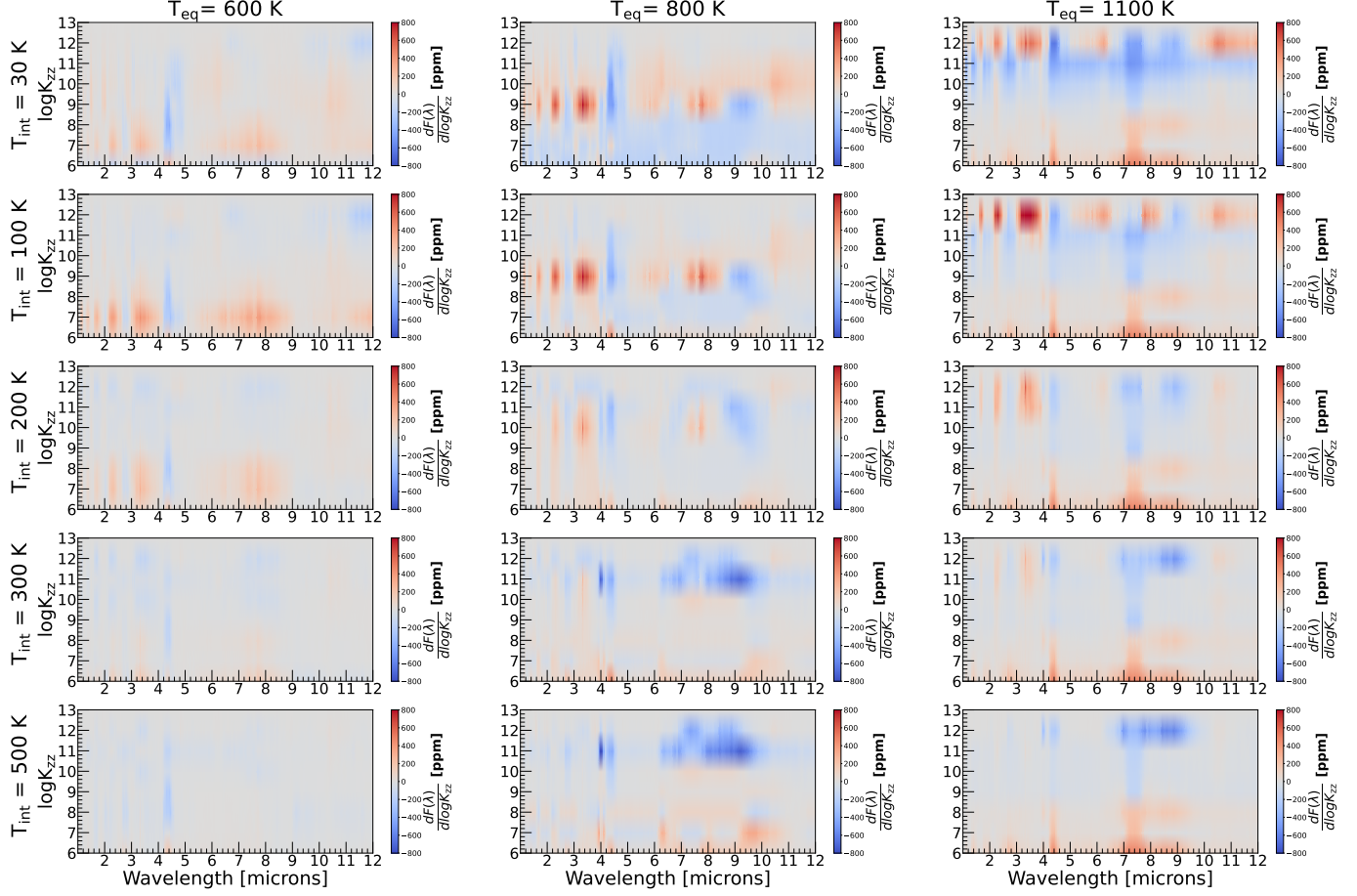
Next, we present the trends in $dF(\lambda)/dlogK_{zz}$ at three different T_{eq} values in Figure 18, instead of the three different C/O values shown in Figure 17. Each column in Figure 18 shows the trends for T_{eq}= 600 K, 800 K, and 1100 K while the C/O has been fixed at 1×solar. Figure 18 shows that transit depths at T_{eq}= 600 K are much less sensitive to K_{zz} than those at T_{eq}= 800 K and T_{eq}= 1100 K. At T_{eq}= 600 K, most of the sensitivity of the spectrum arises in the CO_2 bands (4.2-4.3 μm) and CH_4 bands (3-4 μm and others) at low values of T_{int}. The CH_4 bands show some sensitivity but only when K_{zz} is low whereas the CO_2 band shows sensitivity for a larger range of K_{zz} values. When the $T_{int} \geq 300$ K, there is reduced sensitivity to K_{zz} across the transmission spectrum at T_{eq}=600 K.

The trends in the middle column of Figure 18 and the middle panel of Figure 17 represent the same set of models, so we don't describe them again here. The T_{eq}=1100 K models shown in the right columns of Figure 18 show that the CH_4 bands (between 3-4μm and

others) are particularly sensitive to K_{zz}, especially at high K_{zz} values but this sensitivity diminishes slowly with increasing T_{int} value. The CO_2 feature (4.2-4.3 μm) shows high sensitivity to K_{zz} across all K_{zz} values, but this sensitivity slowly diminishes with increasing T_{int} at T_{eq}=1100 K. While the 4 μm SO_2 feature doesn't show much sensitivity to K_{zz} for this T_{eq} value, but the 7-9 μm SO_2 is very sensitive to K_{zz} throughout all T_{int} and K_{zz} values for the T_{eq}=1100 K case. As it is not possible to present these trends for the whole suite of models within this paper in a wavelength resolved manner, we now move on to showing sensitivity of the transmission spectra to changing T_{int} instead of changing K_{zz}.

3.4.2. *Dependence of spectra on T_{int}*

Figure 19 presents the sensitivity of the transmission spectra to changing T_{int} when the T_{int} changes within our five T_{int} grid points of 30 K, 100 K, 200 K, 300 K, and 500 K. As our T_{int} grid points are non-uniformly spaced, unlike for K_{zz}, we plot the quantity $dF(\lambda)$ here, which is simply the difference in the renormalized transit depths
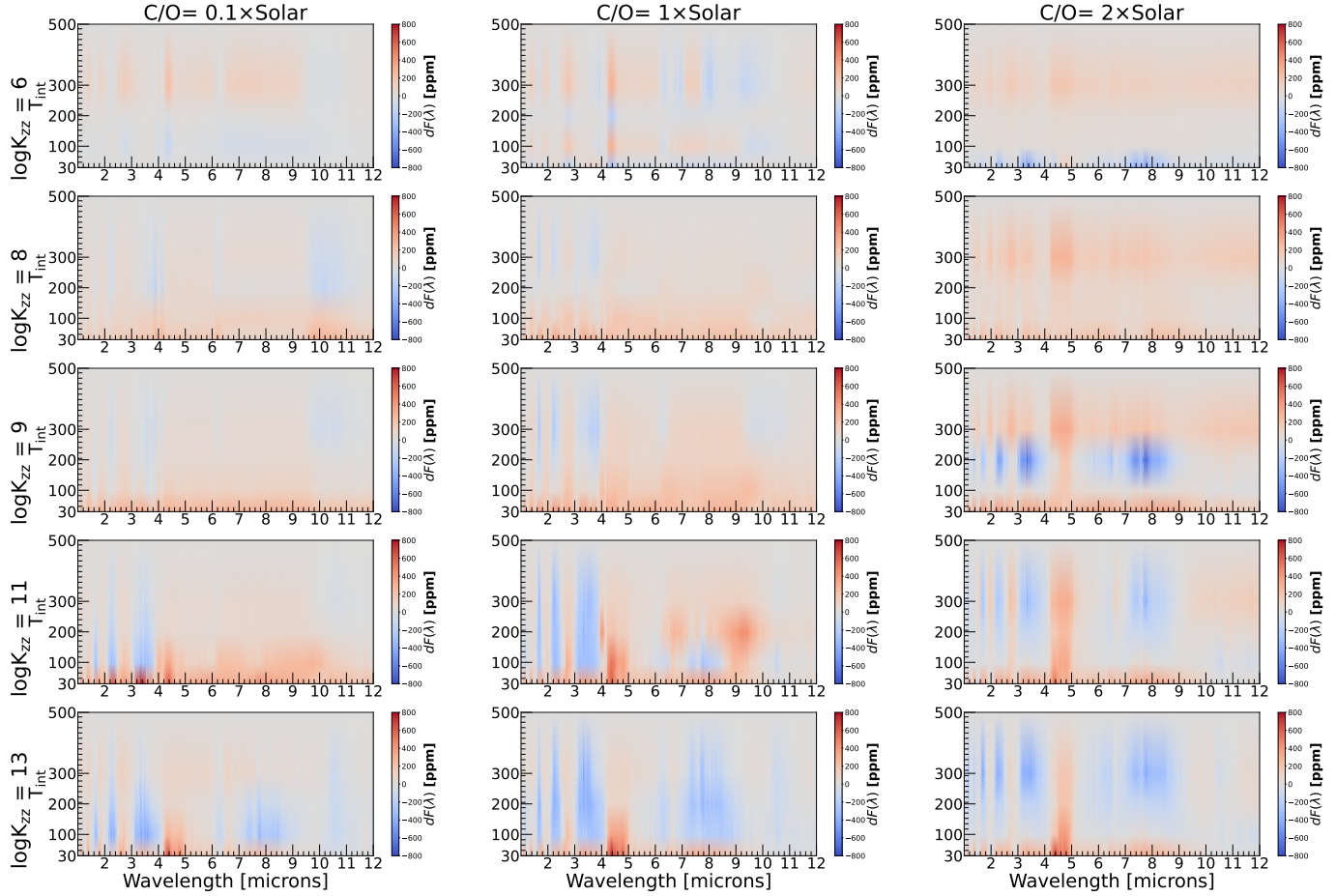
Figure 18. Sensitivity of the transmission spectra to changing K_{zz} is shown here as a function of K_{zz} and wavelength. Each column corresponds to a different T_{eq} value whereas each row shows models for different T_{int} values. All models shown here have C/O=1×solar. A brighter red or a brighter blue color indicates that the transmission spectra is very sensitive to changing K_{zz} at that K_{zz} and wavelength value.

between two T_{int} values. Like Figure 17, each column of Figure 19 also represents different C/O values. But unlike Figure 17, each row of Figure 19 represents a different value of K_{zz} with K_{zz} increasing from the top to the bottom row. It is clear that for the very O- rich case of C/O=0.1×solar shown in the left columns, the sensitivity of the transmission spectra is very subtle to changing T_{int}, especially for low K_{zz} values. But as the K_{zz} values increase, the CH$_4$ band between (3-4 μm) starts to show high sensitivity to changing T_{int}.

The C/O=1×solar models shown in middle column of Figure 19 show a relatively higher level of sensitivity to changing T_{int} value compared to the C/O=0.1×solar models, especially for $K_{zz} \geq 10^9$cm^{2}s^{-1}. Most of the sensitivity here is shown in the CH$_4$ bands (3-4 μm and others) and the sensitivity of the CH$_4$ bands to changing T_{int} increases with increasing K_{zz} at this C/O value. The CO$_2$ absorption bands also show high sensitivity to changing T_{int} values, especially for higher K_{zz} values. For the C/O=2×solar models shown in Figure 19, most

of the sensitivity of the transit depth is mainly seen in the CH$_4$ bands (3-4μm and others) and the the CO$_2$ band between 4.2-4.3 μm.

Figure 20 shows the sensitivity of the transmission spectra at three different T_{eq} values shown in each column for 600 K, 800 K, and 1100 K from left to right, respectively. The C/O ratio has been fixed to 1×solar for this purpose. It is clear that the overall sensitivity of the transmission spectra to changing T_{int} diminishes with increasing T_{eq}. For T_{eq}=600 K, the CH$_4$ and CO$_2$ bands show the most sensitivity to changing T_{int}. This sensitivity increases progressively from low K_{zz} to high K_{zz} at T_{int}=600 K. The T_{eq}=1100 K models shown in the right column show much lower sensitivity of the transit depths to changing T_{int} than the T_{eq}=600 K and T_{eq}=800 K models. This is especially true for $K_{zz} \leq 10^9$cm^{2}s^{-1}. However, when K_{zz} is higher than this value, some T_{int} sensitivity starts to appear in the spectrum. This sensitivity appears primarily in the
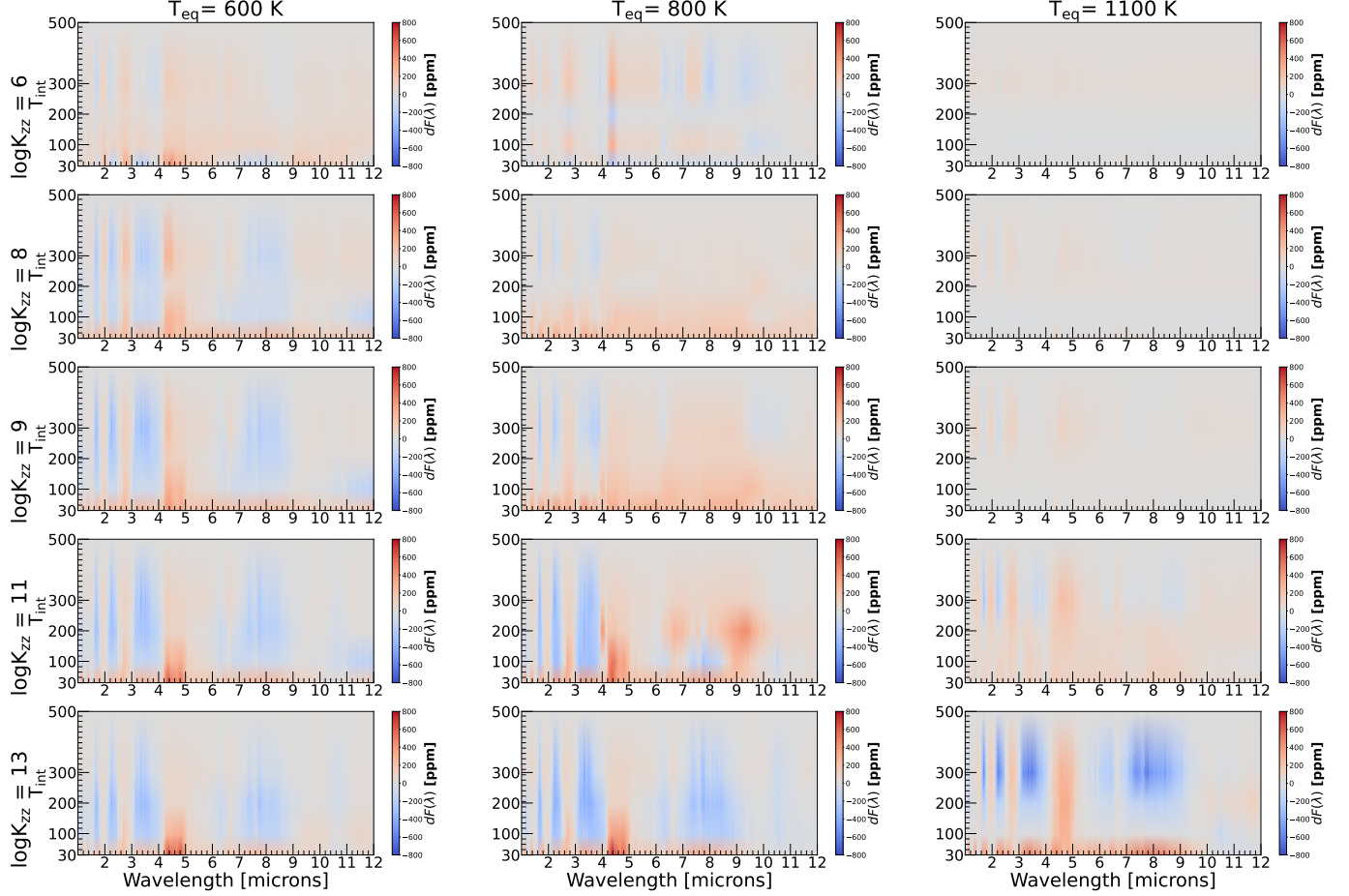
Figure 19. Similar to Figure 17 but the sensitivity of transmission spectra to changing $T_{\rm int}$ is shown here as a function of $T_{\rm int}$ and wavelength, instead of K_{zz} in Figure 17. Each column corresponds to a different C/O value whereas each row shows models for different K_{zz} values. All models shown here have $T_{\rm eq}$=800 K. A brighter red or a brighter blue color indicates that the transmission spectra is very sensitive to changing $T_{\rm int}$ at that $T_{\rm int}$ and wavelength value.

CH_4, CO_2 and CO bands (4.5-4.8 μm) in the $K_{zz}=10^{11}$ and $10^{13} cm^2 s^{-1}$ cases.

Our sensitivity analysis of the transmission spectra reveals that the different wavelength regions in the transmission spectra show complex sensitivity with changing K_{zz} and $T_{\rm int}$ in different parts of the C/O, $T_{\rm eq}$, K_{zz}, and $T_{\rm int}$ parameter space. This suggests that the precision to which parameters like $T_{\rm int}$ and K_{zz} can be constrained for giant transiting planets depends on where that planet lands in this multi-dimensional parameter space. This kind of analysis can also be used to carefully design the wavelength region and the required signal-to-noise to achieve a certain science goal (like constraining $T_{\rm int}$ to a certain precision) with instruments like *JWST*. We avoid presenting similar analysis for eclipse spectroscopy as we chose to ignore the disequilibrium chemistry processes self-consistently within our $T(P)$ profile calculation and that would matter for emission spectra of these planets to a much larger extent than the transmission spectra analysis presented here.

3.5. *Precursors to Soot/Haze*

Photolysis of C- bearing gases (e.g., CH_4) in the upper atmospheres of gas giants can lead to formation of gases like C_2H_2, C_2H_4, C_2H_6, etc, which in turn can act as precursors to haze/soot creation, if the conditions are favorable to further polymerization of these gases (e.g., Fortney et al. 2013; Morley et al. 2013, 2015). This polymerization can be enabled by the reducing nature of the upper atmosphere of these planets. Hazes can have large impact on the observed transmission, reflection, and emission spectra of exoplanets (e.g., Morley et al. 2013; Fortney et al. 2013; Morley et al. 2015; Ohno & Kawashima 2020; Sing et al. 2016). While the *Photochem* kinetics model doesn't track the growth of these hydrocarbons to large polymers, we can still quantitatively estimate the abundances of these haze precursors across the vast parameter space explored in this work. We adopt the methodology presented in Morley et al. (2015) to estimate the column density of haze precursors above 10^{-3} bars. Following Morley et al. (2015)
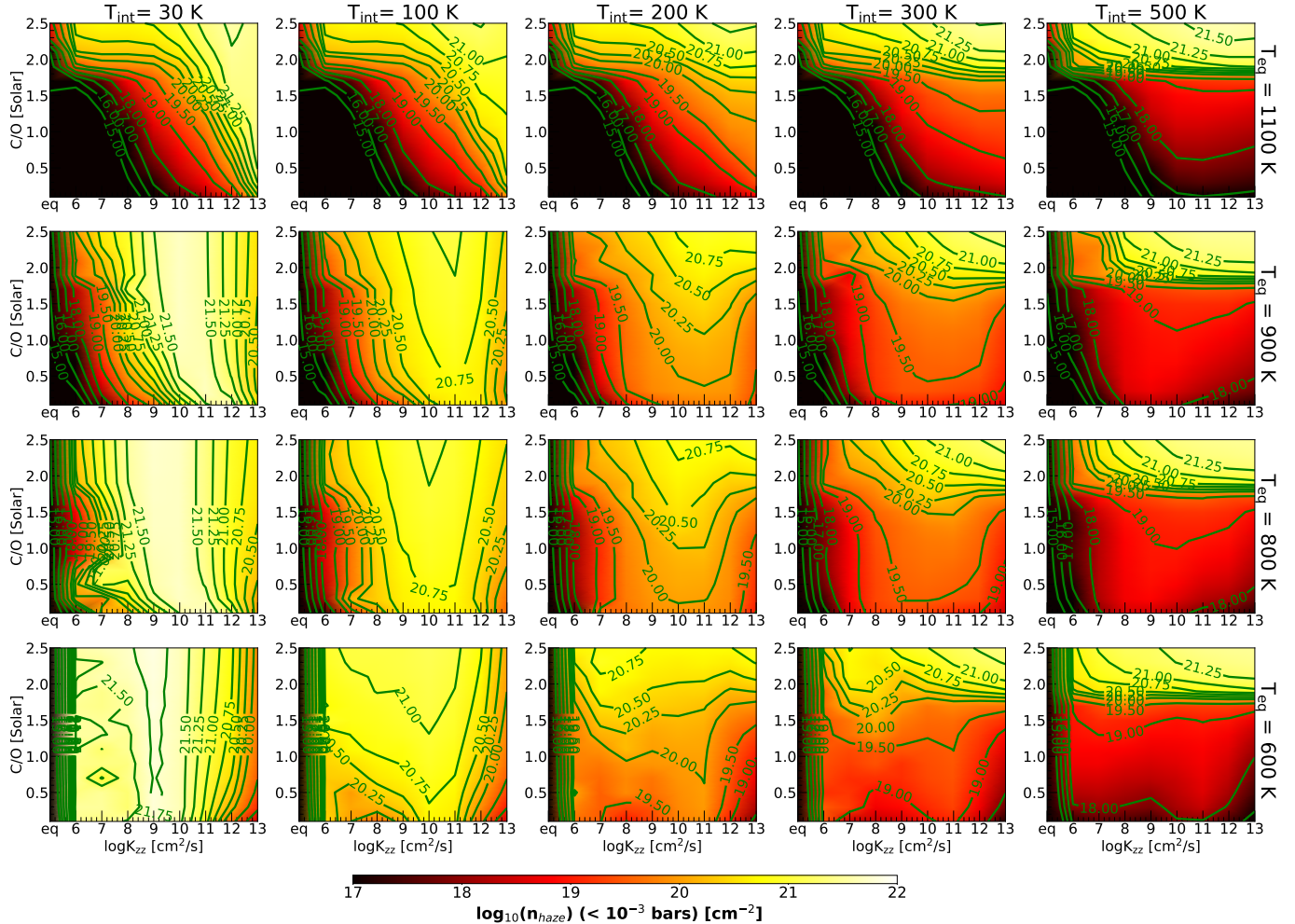
Figure 20. Sensitivity of the transmission spectra to changing $T_{\rm int}$ is shown here as a function of $T_{\rm int}$ and wavelength. Each column corresponds to a different $T_{\rm eq}$ value whereas each row shows models for different K_{zz} values. All models shown here have C/O=1×solar. A brighter red or a brighter blue color indicates that the transmission spectra is very sensitive to changing $T_{\rm int}$ at that $T_{\rm int}$ and wavelength value.

and Tsai et al. (2021), we include the following C- bearing molecules to estimate the abundance of haze/soot precursors– C_2H_2, C_2H_4, C_2H_6, C_4H_2, HCN, CH_3CN, and CS_2. We calculate the column density of these gases at pressures smaller than 10^{-3} bars across our model grid.

Each panel of Figure 21 shows the logarithm of the column density of these precursors as a function of C/O and K_{zz}. Similar to Figure 4, each column represents a value of $T_{\rm int}$ while each row represents a different value of $T_{\rm eq}$. Figure 21 shows that the abundance of haze precursors can be very strongly dependant on K_{zz} in planets with $T_{\rm int} \leq 100$ K. This sensitivity of the haze precursor column density to K_{zz} diminishes with increasing $T_{\rm int}$ at all $T_{\rm eq}$ values. For $T_{\rm eq} \leq 900$ K models with $T_{\rm int}$=30 K, the abundance of haze precursors increases first as a function of increasing K_{zz} before reaching a peak, beyond which it decreases with increasing K_{zz}, for a fixed C/O. The value of K_{zz} where this peak in haze precursor abundance occurs is a strong function of

$T_{\rm eq}$. For $T_{\rm eq}$=1100 K and $T_{\rm int}$=30 K, this peak happens at or beyond K_{zz}=10^{13}cm^2/s, whereas at $T_{\rm eq}$=800 K and $T_{\rm int}$=30 K, this peak occurs at K_{zz}=10^{10}cm^2/s. At $T_{\rm eq}$=600 K, the peak occurs near K_{zz}=10^8cm^2/s, when $T_{\rm int}$=30 K. Similar to the findings of Fortney et al. (2013); Morley et al. (2015), we also find that the abundance of haze precursors shows an increase with decreasing $T_{\rm eq}$ between $T_{\rm eq}$=1100 K and $T_{\rm eq}$= 900 K for a fixed C/O and K_{zz}. Below $T_{\rm eq}$=900 K, for models with $T_{\rm int} \leq 100$ K, whether the column density of precursors increases or decreases with decreasing $T_{\rm eq}$ depends largely on the K_{zz} and C/O. However, when the $T_{\rm int} \geq 200$ K, the column density of the precursors do not show much change with decreasing $T_{\rm eq}$ below $T_{\rm eq}$= 900 K, for a given C/O and K_{zz} value.

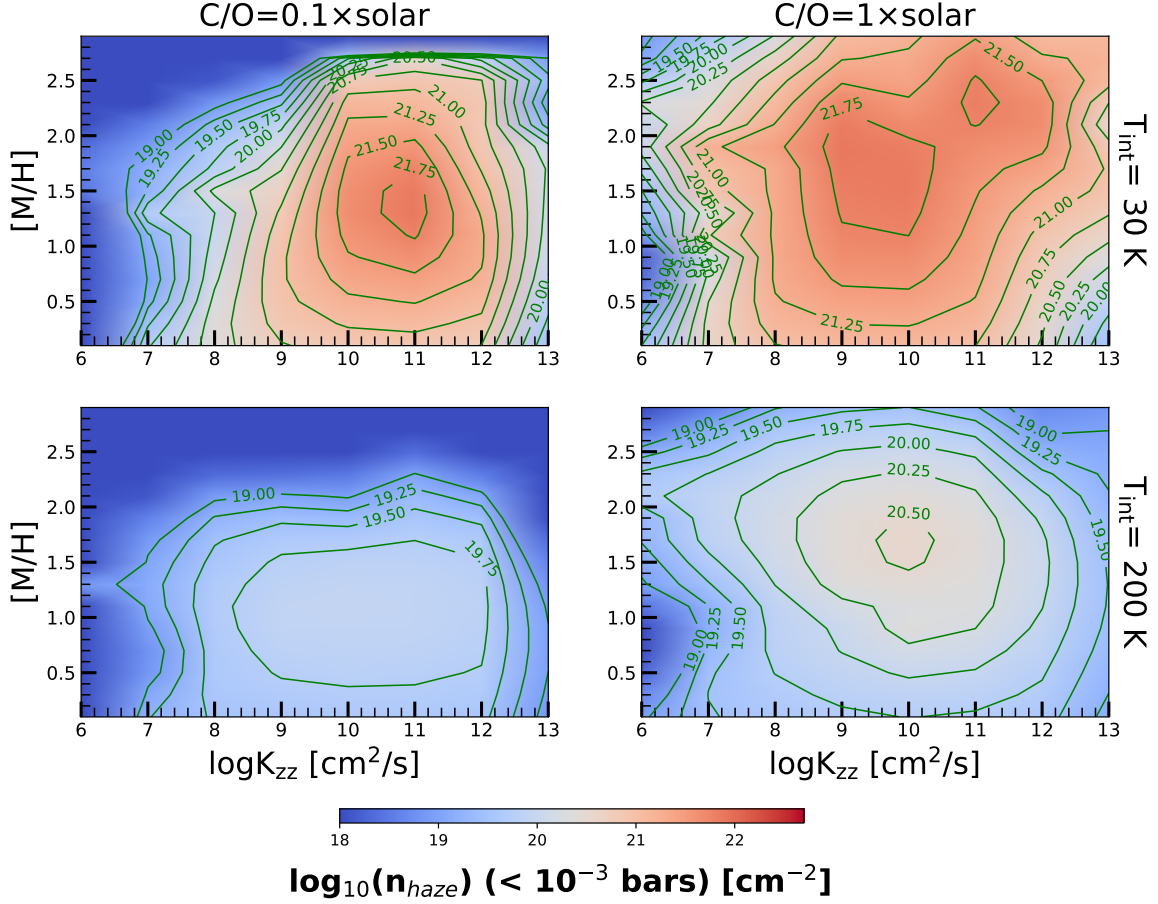Above $T_{\rm int} \geq 100$ K, C/O starts to influence the column density of haze precursors significantly, in addition to K_{zz}. Figure 21 shows that the influence of C/O on the precursors becomes stronger with increasing $T_{\rm int}$ for all $T_{\rm eq}$. For planets with $T_{\rm int} \geq 300$ K, the precursor

Figure 21. The column density of haze precursors at pressures smaller than 10^{-3} bars has been shown as a heat map as a function of C/O and K_{zz} in each panel. Each row corresponds to a different T_{eq} value from 1100 K to 600 K from top to bottom. Each column correspond to a different T_{int} value between 30 K and 500 K from left to right. The abundance of gases– C_2H_2, C_2H_4, C_2H_6, C_4H_2, HCN, CH_3CN, and CS_2 were used to compute the column density of the haze precursor molecules.

column density shows a sharp increase when C/O $\geq$ 2×solar. In these very C- rich atmospheres with hot interiors, the abundance of the precursors mostly remain independent of K_{zz}. For a given value of C/O and K_{zz}, Figure 21 also shows that the abundance of the precursors show an overall decline with increasing T_{int} for all T_{eq} values. This can be seen in the overall fading of the brightness of the panels in Figure 21 as one goes from left to right. Figure 21 proves that the precursors to larger haze molecules in the upper atmosphere of H_2/He rich atmospheres show very complex dependence on K_{zz}, T_{int}, C/O, and T_{eq}. For planets with hotter interiors both C/O and K_{zz} influence the availability of haze precursors in the upper atmosphere, but for planets with low T_{int}, K_{zz} almost solely influences the column density of these precursors in the upper atmosphere. This suggests that for low mass planets at old ages, C/O might not be very correlated to the abun-

dance of hazes in their atmospheres. However, these results are only for 10×solar metal enrichment.

Figure 22 shows the how the column density of the haze precursors vary with metallicity and K_{zz}. The top rows show models with T_{int}=30 K while the bottom row shows models with T_{int}= 200 K. The left and right columns show models at C/O= 0.1×solar and C/O=1×solar, respectively. All the models shown in Figure 22 are for T_{eq}=800 K. Figure 22 shows that the amount of haze precursors in the upper atmosphere generally depends both on [M/H] and K_{zz}, to varying degrees, in all the four panels. When T_{int}=30 K and C/O=0.1×solar (top left panel), the amount of haze precursor starts to show some [M/H] dependence when the K_{zz} is between 10^9 and 10^{12}cm^{2}s^{-1}. At K_{zz} values lower or higher than this range, the abundance of haze precursors shows strong dependence on K_{zz}. For C/O=1×solar and T_{int}=30 K models shown in the top

Figure 22. The column density of haze precursors at pressures smaller than 10^{-3} bars has been shown as a heat map as a function of [M/H] and K_{zz} in each panel. The top row corresponds to $T_{\rm int}=$ 30 K, while the bottom row shows models with $T_{\rm int}=$ 200 K. The $T_{\rm eq}$ has been set to 800 K for all the panels. The left column shows models for C/O=0.1×solar while the right column shows models at C/O=1×solar. The abundance of gases– C_2H_2, C_2H_4, C_2H_6, C_4H_2, HCN, CH_3CN, and CS_2 were used to compute the column density of the haze precursor molecules.

right panel, the abundance of haze precursors show [M/H] dependence when $10^8 \leq K_{zz} \leq 10^{10} {\rm cm^2 s^{-1}}$. For K_{zz} outside this range, the haze precursor column density becomes very sensitive to mixing with little to no dependence on [M/H]. When the $T_{\rm int}$ is higher (bottom panels), the sensitivity of the haze precursors to [M/H] and K_{zz} are also different.

At $T_{\rm int}$=200 K, the C/O=0.1× cases show dependence of the precursor column density to [M/H] when $10^8 \leq K_{zz} \leq 10^{12}$ cm^{2}s^{-1}. But even when K_{zz} lies in between these values, the variation of the precursor abundances with changing [M/H] is much less rapid in this hotter interior model compared to the top panel. However, outside this range of K_{zz} values, the precursor show strong dependence on K_{zz}. When the atmosphere becomes more C- rich in these hotter interior models (bottom right panel), the haze precursor abundance shows greater metallicity dependence. For these

models, the haze precursors become sensitive to K_{zz} for $K_{zz} \geq 10^{12}$ cm^{2}s^{-1} and $K_{zz} \leq 10^8$ cm^{2}s^{-1}.

The maximum abundance of haze precursors occurs between +1.0≤[M/H]≤+1.5 for the top left panel, while the bottom left panel shows maximum precursors between +0.5≤[M/H]≤+1.5. For the top and bottom right panels, maximum precursor abundances are reached between +1.3≤[M/H]≤+2.5 and +1.5≤[M/H]≤+2.0, respectively. The top right panel, with C/O=1×solar and $T_{\rm int}=$ 30 K, also shows that the maximum haze precursor abundance extends to higher metallicities (e.g., [M/H]=+2.5), if K_{zz} is high. All the panels show that the haze precursor abundances can be very low if mixing is not vigorous enough. Comparing the top to the bottom panel in both the columns of Figure 22 shows that planets with lower $T_{\rm int}$ show enhanced levels of haze precursors at all [M/H], K_{zz}, and C/O values compared to planets with hotter interiors. Both Figure 21 and Figure 22 therefore suggest that the atmospheres of lower mass

planets at older ages might have a higher haze content than higher mass planets. However, this only holds true if their interiors have not been heated through external perturbations.

4. DISCUSSION

4.1. *Radiative-convective-Photochemical-Equilibrium*

Figure 2 has already established that there can be significant differences in the $T(P)$ structure calculated using RCTE and RCPE models. This has been shown in previous studies as well (e.g., Drummond et al. 2016; Bell et al. 2023; Welbanks et al. 2024). This self-consistency between disequilibrium chemistry and $T(P)$ profiles has been found to be important for atmospheric models used to interpret the emission spectra of brown dwarfs and directly imaged planets (Mukherjee et al. 2023, 2022; Lacy & Burrows 2023; Phillips et al. 2020; Karalidi et al. 2021; Mukherjee et al. 2024). For the high signal-to-noise spectra of these objects, these atmospheric details matter.

However, we have ignored the self-consistent approach for the bulk of this work as it is not expected to matter much in a parameter space exploration and identification of major trends in chemistry, which is the main focus of this work. The correction of $T(P)$ profile due to RCPE calculations relative to RCTE models will typically be dependant on K_{zz}. Figure 23 shows the $T(P)$ profiles computed with RCPE modeling for three different K_{zz} values for a T_{eq}=800 K object with [M/H]=+1.0 and solar C/O. We calculate these RCPE profiles for two T_{int} values of 100 K and 500 K, which are shown in Figure 23 along with the RCTE $T(P)$ profiles computed in each case. The chemical abundances in each model for CH_4, NH_3, and SO_2 are also shown. It is clear that the correction on the $T(P)$ profiles relative to RCTE models is quite a strong function of both K_{zz} and T_{int}. For example, the absolute δT in the T_{int}=500 K cases are larger but not very K_{zz} dependant, whereas the absolute δT is relatively lower but much more K_{zz} dependant in the T_{int}=100 K. Moreover, we also find that the RCPE models have slightly different radiative-convective boundaries from the RCTE models too. This sensitivity can have modest effects on the absolute abundances presented in this work but does not appear to be strong enough to alter the trends presented here.

We have also made this simplification because here we only explore the effect of the planetary parameters on *transmission spectra* of planets. Drummond et al. (2016) has shown that the effect of the difference between the RCTE and RCPE calculations is much stronger for *eclipse spectroscopy*. Figure 23 reiterates this point and su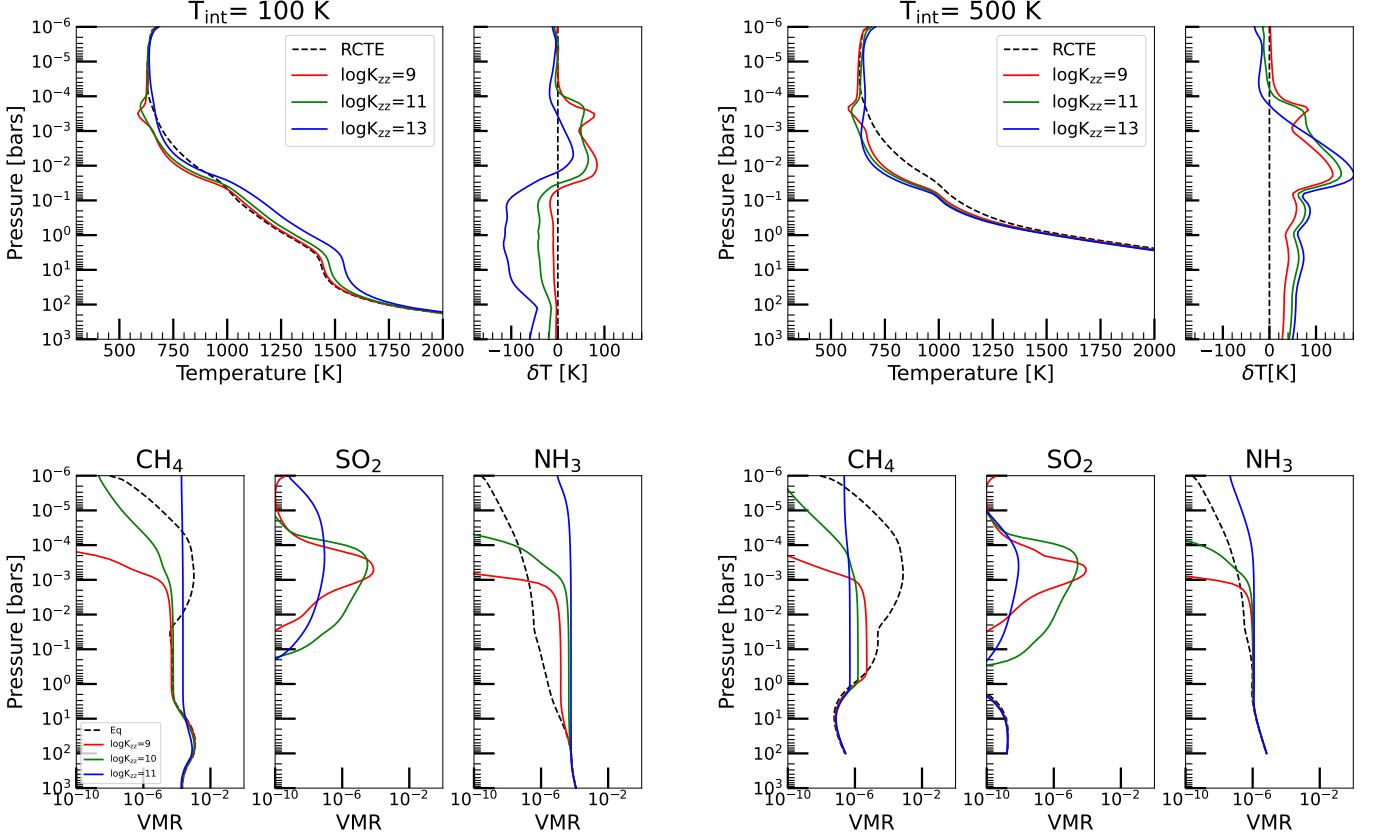ggests that RCPE models should be used when eclipse spectroscopy data of warm and cold transiting planets are interpreted.

4.2. *Dependence of Photochemical Calculations on the UV spectra of host stars*

Figure 3 shows that photochemistry shapes a significant portion of the abundance profiles of gases like CH_4 and SO_2 in/near the pressures typically probed by transmission spectroscopy. Therefore, another planetary parameter which can be influential on the photospheric abundances of gases in irradiated giant planets is the host star X-ray/UV spectra incident on the planetary atmosphere.

The black-dashed line in the bottom panel of Figure 24 shows the nominal UV spectra used for the parameter space exploration presented in §3. The other colored lines show the same UV spectra multiplied with different factors of $100\times$, $10\times$, $0.1\times$, and $0.01\times$. The top panels in Figure 24 show the chemical abundance profiles calculated for the same planet but with these different incident UV fluxes on the planet. We use the T_{eq}= 800 K, T_{int}= 300 K, K_{zz}= 10^6cm^{2}s^{-1}, and C/O= $1.1\times$solar case for all results presented in this section. Abundance profiles for SO_2, CH_4, NH_3, and CO_2 are shown from top left to right, respectively. It is clear that changes in the whole UV flux by five orders of magnitude does not cause the peak SO_2 abundance to change much, but instead has a significant impact on the pressure where it is produced, which can change by two orders of magnitude. For CH_4 and NH_3, that same change in UV flux can cause the pressure at which they are photochemically depleted to change by a factor of 10. On the other hand, the UV flux has almost no effect on the CO_2 abundance profiles. The middle panels in Figure 24 show the effect of UV flux on the abundances when K_{zz}=10^{10}cm^{2}s^{-1}. The effect of the UV flux on the abundances are more pronounced in this case compared to the lower K_{zz} case shown in the top panel. Additionally, CO_2 shows much stronger variation in the upper atmosphere with changing UV flux when the mixing is strong. This exercise shows that having constraints on the overall flux levels of UV photons incident on giant planets is important for interpreting abundances of some gases like SO_2 or CH_4 from observations.

We further explore the sensitivity of atmospheric chemistry to different wavelength regions of the UV spectrum. We take the nominal UV spectra from Figure 24 and divide it into a large number of wavelength bins. Then, we boost the flux at each wavelength bin by a factor of $100\times$ and recalculate the chemistry while keeping the rest of the fluxes in other wavelength bins the same. Figure 25 shows the results from this exercise.

Figure 23. Difference between the $T(P)$ profiles calculated using the RCPE model for three different K_{zz} values and the RCTE model is shown in the top left panel for a T_{int}=100 K model. The same differences are shown for a T_{int}=500 K model in the top right panel. The three bottom left panels show the abundance profiles for each model for CH$_4$, SO$_2$, and NH$_3$ at T_{int}=100 K. The same quantities for the T_{int}= 500 K model are shown in the three bottom right panels. All the models shown here are for T_{eq}=800 K, [M/H]=+1.0, and C/O=1×solar.

The nominal UV spectra are shown in the three panels in light gray, and the many vertical lines at the bottom of each panel depict the wavelength bins that we use. Each panel shows the quantity,
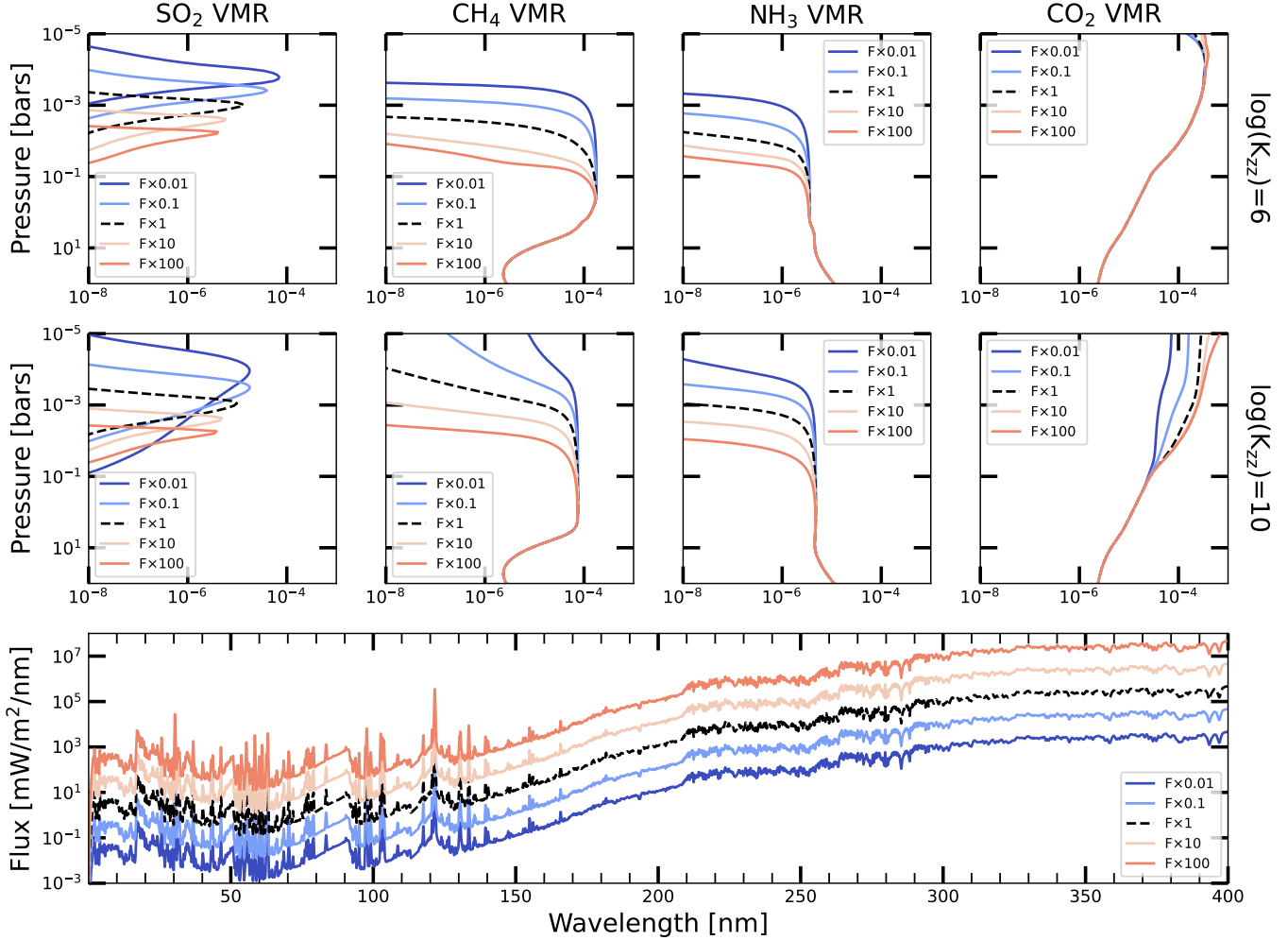
$$Y = log\left(\frac{X(F(w) \times 100)}{X(F(w))}\right) \qquad (2)$$

as a heat map, where $X(F(w) \times 100)$ is the abundance of a gas X calculated when the UV flux at wavelength w has been boosted by a factor of 100. $X(F(w))$ is the abundance of the same gas calculated using the nominal UV flux. When Y in Equation 2 is greater/lower than zero, it means that the boost in UV flux in that wavelength bin causes an increase/decrease in the abundance of molecule X relative to the abundance calculated using the nominal UV flux.

The top left most panel in Figure 25 shows Y for SO$_2$. It shows that the SO$_2$ abundance near 0.1 to 3 mbar shows a decrease if the UV flux between 200 to 240 nm is boosted by a factor of 100. This sensitivity is due to the high UV cross-section of SO$_2$ between 200-240 nm

shown in Figure 26 in Appendix §7. It also shows that the SO$_2$ abundance is slightly enhanced between 1-10 mbar if the UV flux near 350-400 nm is boosted. The SO$_2$ also shows a small increase near the 0.1 mbar level if the UV flux between 300-340 nm is increased. Both of these enhancements in SO$_2$ are linked with the additional destruction of S$_2$ and CS$_2$ when the flux between 300-400 nm is increased. This can be seen in the bottom left and bottom middle panels of Figure 25. This enhanced destruction of S$_2$ and CS$_2$ is due to the strong UV cross-sections of S$_2$ and CS$_2$ between 300-400 nm and 300-350 nm, respectively. Interestingly, the Y map for H$_2$O in the bottom left panel shows the opposite behavior than SO$_2$ when fluxes in the same wavelength ranges are boosted. But this is not visible in the plot as we choose to keep the same color scale across all panels in Figure 25 so that the sensitivity of each gas to changing UV flux can be compared with the rest.

The top middle panel in Figure 25 shows Y for CH$_4$. CH$_4$ abundance shows a small decrease near 0.1-3 mbar region when fluxes between 350-400 nm are boosted.
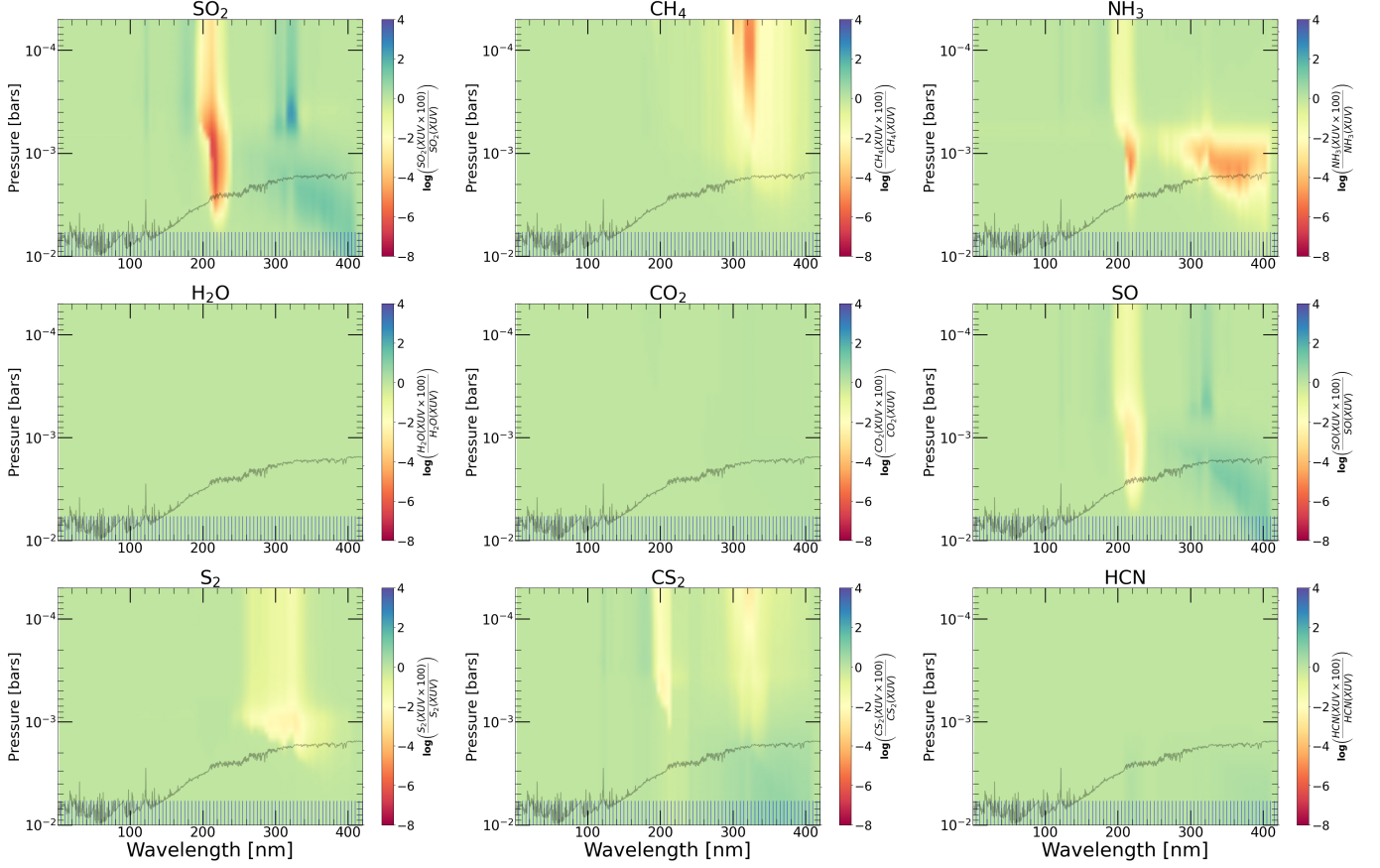
Figure 24. The upper set of panels show the change in abundance profile of key molecules due to change in the X-ray/UV flux incident on the planet when $K_{zz}=10^6 \mathrm{cm}^2\mathrm{s}^{-1}$. Profiles for SO_2, CH_4, NH_3, and CO_2 are shown from left to right, respectively. The black-dashed line shows the profile for the nominal case. The middle row compares the abundances when $K_{zz}=10^{10}\mathrm{cm}^2\mathrm{s}^{-1}$. The lower panel shows the X-ray/UV spectrum used to calculate each of these models.

CH_4 also shows a sharp decrease near the 0.1-0.6 mbar level when flux between 300-350 nm is increased by a factor of 100. Like SO_2, NH_3 abundance also shows a sharp decrease between 0.1-3 mbar when flux between 200-240 nm is increased. This is also related to the high UV cross-section of NH_3 (see Figure 26) between 200-240 nm. Between 0.8-2 mbar, NH_3 shows a depletion when UV fluxes at wavelengths higher than 300 nm are boosted. Comparing Figure 24 and Figure 25 shows that determining the level of UV flux incident on the whole planet in very broad wavelength bands is much more important than determining the very detailed nature of the UV SED to interpret the chemical abundances in irradiated planet atmospheres and connecting them to planetary bulk properties. However, we note that photochemical kinetics calculations are highly non-linear in nature and our calculations have several simplifications.

For example, a more comprehensive radiative–transfer approach like Monte–Carlo radiative transfer and $T - P$ dependant UV cross-sections might provide additional insights.

4.3. *Effect of Condensation on Chemical Kinetics Calculations*

Our photochemical model does not track alkali metals and other condensibles relevant to the deep portions of gas-giant atmospheres. In reality, species like Na_2S and MnS, which we do not model, should condense at relatively high pressures and temperatures which may prevent some amount of sulfur from reaching the upper atmosphere (e.g., Morley et al. 2012). Therefore, our omission of these species should cause our simulations to over-predict the abundance of sulfur gases (e.g., SO_2) in the upper atmosphere. However, we expect our

Figure 25. This plot shows how the abundance of a certain gas changes at a given pressure when the UV flux at a given wavelength bin is increased by a factor of $\times 100$. This has been quantified with Y in Equation 2. This Y quantity has been plotted as a heat map in each panel for SO_2, CH_4, NH_3, H_2O, CO_2, SO, S_2, CS_2, and HCN. The X-axis in each panel is the wavelength of the UV flux and the Y-axis is pressure in the atmosphere. The wavelength bins used for boosting the UV fluxes are also shown as vertical lines at the bottom of each panel along with the nominal UV spectra incident on the planet. A positive value for Y at a given pressure and wavelength means that the molecular abundance has increased relative to the nominal case when UV flux at those wavelengths were boosted. A negative Y value corresponds to a decrease instead.

over-prediction to be small and inconsequential, because sulfur should be far more abundant than the alkali metals. For example, the Sun has $\sim 10\times$ more sulfur atoms than sodium atoms (Lodders et al. 2009), meaning Na_2S condensation could, at most, only sequester about 5% of the available sulfur. In summary, we expect the lack of condensibles in our photochemical model to cause our results to over-estimate the sulfur in the upper atmosphere by an amount that does not effect our overall conclusions which is based on order-of-magnitude trends in sulfur bearing species.

4.4. *Steady-State Convergence of Chemical Kinetics Model*

To achieve a photochemical steady-state, the *Photochem* code integrates the photochemical equations forward in time until the atmosphere ceases to change. Our code identifies convergence to such a steady-state with

the following criteria:

$$\Delta y_{\max} = \max \left| \frac{f_{ij}(t_n) - f_{ij}(t_n/2)}{f_{ij}(t_n)} \right| \qquad (3)$$

$$\frac{\Delta y_{\max}}{\Delta t} = \frac{\Delta y_{\max}}{t_n/2} \qquad (4)$$

Here, f_{ij} is the mixing ratio of species i in layer j, and t_n is the current integration time, making $\Delta y_{\max}$ the maximum relative change over the last $t_n/2$ seconds. We assume a steady-state is achieved when $\Delta y_{\max} < 0.05$ and $\frac{\Delta y_{\max}}{\Delta t} < 10^{-4}$. From testing, these criteria appear appropriate over a wide parameter space. Furthermore, the VULCAN photochemical code (Tsai et al. 2017) uses similar convergence requirements that have proved reliable for warm gas-rich planets (e.g., Tsai et al. (2023c)).

Photochem, like many other chemical kinetics models (e.g., VULCAN (Tsai et al. 2021)), computes the atmospheric chemistry in a grid of atmospheric altitudes instead of the pressure space used in the PICASO climate

model. As a result, as the chemistry of the atmosphere evolves in the chemical kinetics model, the mean molecular weight of the atmosphere also changes. So, when the altitudes are converted back to pressures after the kinetics models have converged, the $T(P)$ profile effectively becomes ever so slightly different than the input $T(P)$ profile. To avoid this, the *Photochem* code adaptively re-grids and adjusts the temperature profile during integration as to ensure the $T(P)$ profile matches the input `PICASO` $T(P)$ profile. This approach is particularly very important for the RCPE models we have presented in this work, where the chemical kinetics model is iteratively coupled directly with the climate model.

5. CONCLUSIONS

We have explored the variation of atmospheric chemistry in close-in giant transiting exoplanets across a vast parameter space of bulk planetary properties like T_{eq}, T_{int}, [M/H], and C/O. Our exploration includes chemical disequilibrium processes such as vertical mixing and photochemistry and is applicable for a wide variety of planets in terms of their mass, age, and proximity to their host stars. We have arrived at the following conclusions from this exploration,

1. We have shown that the the photospheric abundances of gases like CH_4 can be sensitive to just the K_{zz} parameter or just the C/O ratio or can also be quite degenerate between the two depending on the bulk properties of the planet like T_{int} or T_{eq} and also atmospheric properties like the vigor of vertical mixing. We have identified these trends in this work at different parts of the parameter space.

2. We have shown that CO is a good tracer of the C/O ratio and remains largely independent of K_{zz}, unless the T_{int} of the planet is ≤ 100 K. For these cold interior planets, CO can become much better tracers of K_{zz} than C/O.

3. CO_2 on the other hand shows strong sensitivity to K_{zz} if the $T_{eq} \leq 900$ K. This sensitivity is particularly enhanced for cold interiors. We also show that NH_3 is an excellent tracer of K_{zz}, without much dependence on C/O, as expected.

4. Photochemically produced SO_2 on the other hand depends quite strongly on the C/O of the planet unless the K_{zz} exceeds high values like $\sim 10^{11} \mathrm{cm^2 s^{-1}}$. We also show that SO_2 abundance shows a very sharp decline once the $T_{eq} \leq 600$ K. For these colder T_{eq} planets, we find that the S- content of the photosphere is carried by other gases like CS, CS_2, and S_8. We also find that atomic S is a major carrier of S- near the photosphere irrespective of T_{eq}.

5. We also explore how the abundances of some key gases in the atmosphere behave in the [M/H] vs. K_{zz} space. Among other trends, we find that other S- carriers like OCS and H_2S can show a rapid increase with K_{zz} in the photosphere, especially for metal enriched objects.

6. In order to explore the major chemical transitions in the atmosphere with T_{eq}, we explore the T_{eq} vs. abundance trends of gas combinations like CO-CH_4, NH_3-N_2, and SO_2-H_2S-S. Our findings on these key transitions reflect the findings from previous work (Fortney et al. 2020; Ohno & Fortney 2023b,a; Baxter et al. 2021; Hobbs et al. 2021; Polman et al. 2023). Interestingly, we find that even in the photosphere, atomic S can carry a significant fraction of the S- inventory along with H_2S and SO_2.

7. In order to explore how sensitive is the transmission spectra to parameters like K_{zz} and T_{int} in different parts of the parameter space, we present a wavelength resolved sensitivity analysis of the transmission spectra to these parameters. We find that the sensitivity of the transmission spectra to these parameters is quite complex. In some parts of the parameter space, the CH_4 absorption bands might show great sensitivity to K_{zz}, while in some parts the CO_2 or SO_2 bands might show the highest sensitivity to changing K_{zz} or T_{int}.

8. We calculate the column number density of molecules like C_2H_x, HCN, etc, which can act as precursors to photochemical hazes in the upper atmosphere. We find that these precursors molecules show very strong dependence on K_{zz} and almost no dependence on C/O for planets with cold interiors ($T_{int} \leq 100$ K) at 10×solar metallicity. We also find that planets with low T_{int} are likely to have significantly higher abundance of haze precursors in the upper atmosphere compared to planets with hotter interiors. This is especially relevant to older low mass planets with no external heating.

There are several aspects of our modeling of giant planet atmospheric chemistry which can be improved in the near future. These include inclusion of more elements in our chemical kinetics calculations and inclusion of condensation and rainout chemistry within our chemistry calculation as well. We think that the assumptions made in our modeling approach are sufficient for

the typical quality of transmission spectra obtained with *JWST*, especially in the near-future. But these kind of improvements might lead to new avenues of characterizing the physics and chemistry of giant planet atmospheres and also their bulk properties.
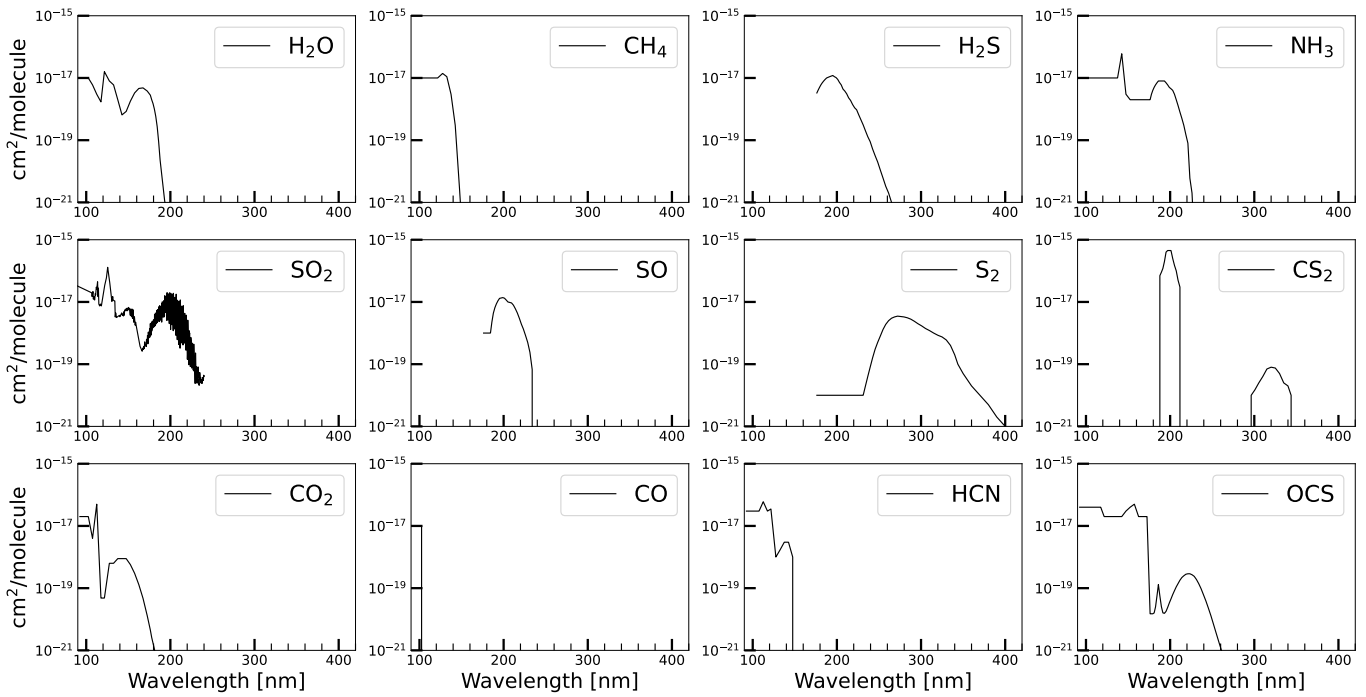
6. ACKNOWLEDGEMENT

Software: PICASO 3.0 (Mukherjee et al. 2023), PICASO (Batalha et al. 2019), pandas (McKinney 2010), NumPy (Walt et al. 2011), IPython (Pérez & Granger 2007), Jupyter (Kluyver et al. 2016), matplotlib (Hunter 2007), the model grid will be formally released via Zenodo.

7. APPENDIX

Here we present the UV cross-sections of key gases used in the *Photochem* chemical kinetics model. Figure 26 shows the UV cross-section used in this work for 12 major molecules. Each panel shows the cross-section for a different molecule.

REFERENCES

Agúndez, M., Venot, O., Selsis, F., & Iro, N. 2014, ApJ, 781, 68, doi: 10.1088/0004-637X/781/2/68

Ahrer, E.-M., Stevenson, K. B., Mansfield, M., et al. 2022, arXiv e-prints, arXiv:2211.10489, doi: 10.48550/arXiv.2211.10489

Alderson, L., Wakeford, H. R., Alam, M. K., et al. 2022, arXiv e-prints, arXiv:2211.10488, doi: 10.48550/arXiv.2211.10488

Allen, M., Yung, Y. L., & Waters, J. W. 1981, Journal of Geophysical Research: Space Physics, 86, 3617, doi: https://doi.org/10.1029/JA086iA05p03617

Arfaux, A., & Lavvas, P. 2022, MNRAS, 515, 4753, doi: 10.1093/mnras/stac1772

August, P. C., Bean, J. L., Zhang, M., et al. 2023, ApJL, 953, L24, doi: 10.3847/2041-8213/ace828

Barat, S., Désert, J.-M., Vazan, A., et al. 2024, Nature Astronomy, 8, 899, doi: 10.1038/s41550-024-02257-0

Batalha, N. E., Marley, M. S., Lewis, N. K., & Fortney, J. J. 2019, ApJ, 878, 70, doi: 10.3847/1538-4357/ab1b51

Baxter, C., Désert, J.-M., Tsai, S.-M., et al. 2021, A&A, 648, A127, doi: 10.1051/0004-6361/202039708

Bean, J. L., Xue, Q., August, P. C., et al. 2023, Nature, 618, 43, doi: 10.1038/s41586-023-05984-y

Beatty, T. G., Welbanks, L., Schlawin, E., et al. 2024, ApJL, 970, L10, doi: 10.3847/2041-8213/ad55e9

Beiler, S., Cushing, M., Kirkpatrick, D., et al. 2023, arXiv e-prints, arXiv:2306.11807, doi: 10.48550/arXiv.2306.11807

Bell, T. J., Welbanks, L., Schlawin, E., et al. 2023, Nature, 623, 709, doi: 10.1038/s41586-023-06687-0

Benneke, B., Roy, P.-A., Coulombe, L.-P., et al. 2024, arXiv e-prints, arXiv:2403.03325, doi: 10.48550/arXiv.2403.03325

Cooper, C. S., & Showman, A. P. 2006, ApJ, 649, 1048, doi: 10.1086/506312

Crossfield, I. J. M. 2023, ApJL, 952, L18, doi: 10.3847/2041-8213/ace35f

Drummond, B., Tremblin, P., Baraffe, I., et al. 2016, A&A, 594, A69, doi: 10.1051/0004-6361/201628799

Drummond, B., Mayne, N. J., Manners, J., et al. 2018, ApJL, 855, L31, doi: 10.3847/2041-8213/aab209

Drummond, B., Hébrard, E., Mayne, N. J., et al. 2020, A&A, 636, A68, doi: 10.1051/0004-6361/201937153

Feinstein, A. D., Radica, M., Welbanks, L., et al. 2022, arXiv e-prints, arXiv:2211.10493, doi: 10.48550/arXiv.2211.10493

Fortney, J. J., Lodders, K., Marley, M. S., & Freedman, R. S. 2008, ApJ, 678, 1419, doi: 10.1086/528370

Fortney, J. J., Marley, M. S., & Barnes, J. W. 2007, ApJ, 659, 1661, doi: 10.1086/512120

Fortney, J. J., Marley, M. S., Lodders, K., Saumon, D., & Freedman, R. 2005, ApJL, 627, L69, doi: 10.1086/431952

Fortney, J. J., Mordasini, C., Nettelmann, N., et al. 2013, ApJ, 775, 80, doi: 10.1088/0004-637X/775/1/80

Fortney, J. J., Visscher, C., Marley, M. S., et al. 2020, AJ, 160, 288, doi: 10.3847/1538-3881/abc5bd

Freytag, B., Allard, F., Ludwig, H. G., Homeier, D., & Steffen, M. 2010, A&A, 513, A19, doi: 10.1051/0004-6361/200913354

Fu, G., Welbanks, L., Deming, D., et al. 2024, Nature, 632, 752, doi: 10.1038/s41586-024-07760-y

Gagnebin, A., Mukherjee, S., Fortney, J. J., & Batalha, N. E. 2024, ApJ, 969, 86, doi: 10.3847/1538-4357/ad452d

Gao, P., Thorngren, D. P., Lee, G. K. H., et al. 2020, Nature Astronomy, doi: 10.1038/s41550-020-1114-3

Figure 26. The UV cross section as a function of wavelength for different gases are shown in each panel. These cross-sections were used in our chemical kinetics modeling.

Goodwin, D. G., Moffat, H. K., Schoegl, I., Speth, R. L., & Weber, B. W. 2023, Cantera: An Object-oriented Software Toolkit for Chemical Kinetics, Thermodynamics, and Transport Processes, https://www.cantera.org, doi: 10.5281/zenodo.8137090

Goyal, J. M., Mayne, N., Sing, D. K., et al. 2018, MNRAS, 474, 5158, doi: 10.1093/mnras/stx3015

Grant, D., Lewis, N. K., Wakeford, H. R., et al. 2023, ApJL, 956, L32, doi: 10.3847/2041-8213/acfc3b10.3847/2041-8213/acfdab

Hobbs, R., Rimmer, P. B., Shorttle, O., & Madhusudhan, N. 2021, Monthly Notices of the Royal Astronomical Society, 506, 3186, doi: 10.1093/mnras/stab1839

Holmberg, M., & Madhusudhan, N. 2024, A&A, 683, L2, doi: 10.1051/0004-6361/202348238

Hu, R. 2021, ApJ, 921, 27, doi: 10.3847/1538-4357/ac1789

Hubeny, I., & Burrows, A. 2007, ApJ, 659, 1458, doi: 10.1086/512179

Hunter, J. D. 2007, Computing in Science & Engineering, 9, 90, doi: 10.1109/MCSE.2007.55

Inglis, J., Batalha, N. E., Lewis, N. K., et al. 2024, ApJL, 973, L41, doi: 10.3847/2041-8213/ad725e

Karalidi, T., Marley, M., Fortney, J. J., et al. 2021, ApJ, 923, 269, doi: 10.3847/1538-4357/ac3140

Kawashima, Y., & Ikoma, M. 2018, ApJ, 853, 7, doi: 10.3847/1538-4357/aaa0c5

Kawashima, Y., & Min, M. 2021, A&A, 656, A90, doi: 10.1051/0004-6361/202141548

Kirk, J., Ahrer, E.-M., Claringbold, A. B., et al. 2024, arXiv e-prints, arXiv:2410.08116, doi: 10.48550/arXiv.2410.08116

Kluyver, T., Ragan-Kelley, B., Pérez, F., et al. 2016, in ELPUB, 87–90

Komacek, T. D., Showman, A. P., & Parmentier, V. 2019, ApJ, 881, 152, doi: 10.3847/1538-4357/ab338b

Kothari, H., Cushing, M. C., Burningham, B., et al. 2024, ApJ, 971, 121, doi: 10.3847/1538-4357/ad583b

Lacy, B., & Burrows, A. 2023, ApJ, 950, 8, doi: 10.3847/1538-4357/acc8cb

Lavvas, P., & Koskinen, T. 2017, ApJ, 847, 32, doi: 10.3847/1538-4357/aa88ce

Lee, E. K. H., Tan, X., & Tsai, S.-M. 2023, MNRAS, 523, 4477, doi: 10.1093/mnras/stad1715

Lodders, K. 2004, ApJ, 611, 587, doi: 10.1086/421970

Lodders, K., & Fegley, B. 2002, Icarus, 155, 393, doi: 10.1006/icar.2001.6740

Lodders, K., Palme, H., & Gail, H. P. 2009, Landolt Börnstein, 4B, 712, doi: 10.1007/978-3-540-88055-4_34

Lopez, E. D., & Fortney, J. J. 2014, ApJ, 792, 1, doi: 10.1088/0004-637X/792/1/1

Madhusudhan, N. 2012, ApJ, 758, 36, doi: 10.1088/0004-637X/758/1/36

Madurowicz, A., Mukherjee, S., Batalha, N., et al. 2023, AJ, 165, 238, doi: 10.3847/1538-3881/acca7a

Marley, M. S., Saumon, D., Visscher, C., et al. 2021, ApJ, 920, 85, doi: 10.3847/1538-4357/ac141d

McKinney, W. 2010, in Proceedings of the 9th Python in Science Conference, ed. S. van der Walt & J. Millman, 51 – 56

Mendonça, J. M., Tsai, S.-m., Malik, M., Grimm, S. L., & Heng, K. 2018, ApJ, 869, 107, doi: 10.3847/1538-4357/aaed23

Menou, K. 2019, Monthly Notices of the Royal Astronomical Society: Letters, 485, L98, doi: 10.1093/mnrasl/slz041

Menou, K., & Rauscher, E. 2009, ApJ, 700, 887, doi: 10.1088/0004-637X/700/1/887

Miles, B. E., Skemer, A. J. I., Morley, C. V., et al. 2020, AJ, 160, 63, doi: 10.3847/1538-3881/ab9114

Mollière, P., van Boekel, R., Dullemond, C., Henning, T., & Mordasini, C. 2015, ApJ, 813, 47, doi: 10.1088/0004-637X/813/1/47

Mollière, P., Molyarova, T., Bitsch, B., et al. 2022, ApJ, 934, 74, doi: 10.3847/1538-4357/ac6a56

Mordasini, C., van Boekel, R., Mollière, P., Henning, T., & Benneke, B. 2016, ApJ, 832, 41, doi: 10.3847/0004-637X/832/1/41

Morley, C. V., Fortney, J. J., Kempton, E. M. R., et al. 2013, ApJ, 775, 33, doi: 10.1088/0004-637X/775/1/33

Morley, C. V., Fortney, J. J., Marley, M. S., et al. 2012, ApJ, 756, 172, doi: 10.1088/0004-637X/756/2/172

—. 2015, ApJ, 815, 110, doi: 10.1088/0004-637X/815/2/110

Morley, C. V., Marley, M. S., Fortney, J. J., et al. 2014, ApJ, 787, 78, doi: 10.1088/0004-637X/787/1/78

Morley, C. V., Mukherjee, S., Marley, M. S., et al. 2024, arXiv e-prints, arXiv:2402.00758, doi: 10.48550/arXiv.2402.00758

Moses, J. I., Madhusudhan, N., Visscher, C., & Freedman, R. S. 2013a, ApJ, 763, 25, doi: 10.1088/0004-637X/763/1/25

Moses, J. I., Visscher, C., Fortney, J. J., et al. 2011, ApJ, 737, 15, doi: 10.1088/0004-637X/737/1/15

Moses, J. I., Line, M. R., Visscher, C., et al. 2013b, ApJ, 777, 34, doi: 10.1088/0004-637X/777/1/34

Moses, J. I., Marley, M. S., Zahnle, K., et al. 2016, ApJ, 829, 66, doi: 10.3847/0004-637X/829/2/66

Mukherjee, S., Batalha, N. E., Fortney, J. J., & Marley, M. S. 2023, ApJ, 942, 71, doi: 10.3847/1538-4357/ac9f48

38

Mukherjee, S., Fortney, J. J., Batalha, N. E., et al. 2022, ApJ, 938, 107, doi: 10.3847/1538-4357/ac8dfb

Mukherjee, S., Fortney, J. J., Morley, C. V., et al. 2024, arXiv e-prints, arXiv:2402.00756, doi: 10.48550/arXiv.2402.00756

Öberg, K. I., Murray-Clay, R., & Bergin, E. A. 2011, ApJL, 743, L16, doi: 10.1088/2041-8205/743/1/L16

Ohno, K., & Fortney, J. J. 2023a, ApJ, 956, 125, doi: 10.3847/1538-4357/ace531

—. 2023b, ApJ, 946, 18, doi: 10.3847/1538-4357/acafed

Ohno, K., & Kawashima, Y. 2020, ApJL, 895, L47, doi: 10.3847/2041-8213/ab93d7

Parmentier, V., Showman, A. P., & Lian, Y. 2013, A&A, 558, A91, doi: 10.1051/0004-6361/201321132

Pérez, F., & Granger, B. E. 2007, Computing in Science & Engineering, 9

Phillips, M. W., Tremblin, P., Baraffe, I., et al. 2020, A&A, 637, A38, doi: 10.1051/0004-6361/201937381

Polman, J., Waters, L. B. F. M., Min, M., Miguel, Y., & Khorshid, N. 2023, A&A, 670, A161, doi: 10.1051/0004-6361/202244647

Radica, M., Welbanks, L., Espinoza, N., et al. 2023, MNRAS, 524, 835, doi: 10.1093/mnras/stad1762

Ranjan, S., Schwieterman, E. W., Harman, C., et al. 2020, ApJ, 896, 148, doi: 10.3847/1538-4357/ab9363

Roth, A., Parmentier, V., & Hammond, M. 2024, MNRAS, doi: 10.1093/mnras/stae984

Rustamkulov, Z., Sing, D. K., Mukherjee, S., et al. 2022, arXiv e-prints, arXiv:2211.10487, doi: 10.48550/arXiv.2211.10487

Saumon, D., & Marley, M. S. 2008, ApJ, 689, 1327, doi: 10.1086/592734

Schlawin, E., Mukherjee, S., Ohno, K., et al. 2024, AJ, 168, 104, doi: 10.3847/1538-3881/ad58e0

Showman, A. P., Fortney, J. J., Lian, Y., et al. 2009, ApJ, 699, 564, doi: 10.1088/0004-637X/699/1/564

Sing, D. K., Fortney, J. J., Nikolov, N., et al. 2016, Nature, 529, 59, doi: 10.1038/nature16068

Sing, D. K., Rustamkulov, Z., Thorngren, D. P., et al. 2024, arXiv e-prints, arXiv:2405.11027, doi: 10.48550/arXiv.2405.11027

Steinrueck, M. E., Koskinen, T., Lavvas, P., et al. 2023, ApJ, 951, 117, doi: 10.3847/1538-4357/acd4bb

Steinrueck, M. E., Parmentier, V., Showman, A. P., Lothringer, J. D., & Lupu, R. E. 2019, ApJ, 880, 14, doi: 10.3847/1538-4357/ab2598

Tan, X. 2022, Monthly Notices of the Royal Astronomical Society, 511, 4861, doi: 10.1093/mnras/stac344

Thao, P. C., Mann, A. W., Feinstein, A. D., et al. 2024, arXiv e-prints, arXiv:2409.16355, doi: 10.48550/arXiv.2409.16355

Tsai, S.-M., Lyons, J. R., Grosheintz, L., et al. 2017, ApJS, 228, 20, doi: 10.3847/1538-4365/228/2/20

Tsai, S.-M., Malik, M., Kitzmann, D., et al. 2021, ApJ, 923, 264, doi: 10.3847/1538-4357/ac29bc

Tsai, S.-M., Moses, J. I., Powell, D., & Lee, E. K. H. 2023a, ApJL, 959, L30, doi: 10.3847/2041-8213/ad1405

Tsai, S.-M., Steinrueck, M., Parmentier, V., Lewis, N., & Pierrehumbert, R. 2023b, MNRAS, 520, 3867, doi: 10.1093/mnras/stad214

Tsai, S.-M., Lee, E. K. H., Powell, D., et al. 2023c, Nature, 617, 483, doi: 10.1038/s41586-023-05902-2

Venot, O., Hébrard, E., Agúndez, M., et al. 2012, A&A, 546, A43, doi: 10.1051/0004-6361/201219310

Visscher, C., & Fegley, Bruce, J. 2005, ApJ, 623, 1221, doi: 10.1086/428493

Visscher, C., Lodders, K., & Fegley, Bruce, J. 2006, ApJ, 648, 1181, doi: 10.1086/506245

Walt, S. v. d., Colbert, S. C., & Varoquaux, G. 2011, Computing in Science & Engineering, 13, 22

Welbanks, L., Bell, T. J., Beatty, T. G., et al. 2024, arXiv e-prints, arXiv:2405.11018, doi: 10.48550/arXiv.2405.11018

Wogan, N. F., Batalha, N. E., Zahnle, K. J., et al. 2024, ApJL, 963, L7, doi: 10.3847/2041-8213/ad2616

Wogan, N. F., Catling, D. C., Zahnle, K. J., & Lupu, R. 2023, PSJ, 4, 169, doi: 10.3847/PSJ/aced83

Xue, Q., Bean, J. L., Zhang, M., et al. 2024, ApJL, 963, L5, doi: 10.3847/2041-8213/ad2682

Zahnle, K., Marley, M. S., Freedman, R. S., Lodders, K., & Fortney, J. J. 2009, ApJL, 701, L20, doi: 10.1088/0004-637X/701/1/L20

Zahnle, K., Marley, M. S., Morley, C. V., & Moses, J. I. 2016, ApJ, 824, 137, doi: 10.3847/0004-637X/824/2/137

Zahnle, K. J., & Marley, M. S. 2014, ApJ, 797, 41, doi: 10.1088/0004-637X/797/1/41

Zamyatina, M., Hébrard, E., Drummond, B., et al. 2023, MNRAS, 519, 3129, doi: 10.1093/mnras/stac3432

Zhang, X. 2020, Research in Astronomy and Astrophysics, 20, 099, doi: 10.1088/1674-4527/20/7/99